University of Louisville

ThinkIR: The University of Louisville's Institutional Repository

Electronic Theses and Dissertations

12-2022

Design, evaluation, and control of nexus: a multiscale additive manufacturing platform with integrated 3D printing and robotic assembly.

Danming Wei
University of Louisville

Follow this and additional works at: https://ir.library.louisville.edu/etd

Part of the Electrical and Computer Engineering Commons

Recommended Citation

Wei, Danming, "Design, evaluation, and control of nexus: a multiscale additive manufacturing platform with integrated 3D printing and robotic assembly." (2022). *Electronic Theses and Dissertations.* Paper 3997.
https://doi.org/10.18297/etd/3997

This Doctoral Dissertation is brought to you for free and open access by ThinkIR: The University of Louisville's Institutional Repository. It has been accepted for inclusion in Electronic Theses and Dissertations by an authorized administrator of ThinkIR: The University of Louisville's Institutional Repository. This title appears here courtesy of the author, who has retained all other copyrights. For more information, please contact thinkir@louisville.edu.

DESIGN, EVALUATION, AND CONTROL OF NEXUS: A MULTISCALE ADDITIVE MANUFACTURING PLATFORM WITH INTEGRATED 3D PRINTING AND ROBOTIC ASSEMBLY

By

Danming Wei
B.S., Dalian Jiaotong University, 2011
M.S., Western Kentucky University, 2016
M.S., University of Louisville, 2018

A Dissertation
Submitted to the Faculty of the
J. B. Speed School of Engineering of the University of Louisville
in Partial Fulfillment of the Requirements
for the Degree of

Doctor of Philosophy
in Electrical Engineering

Department of Electrical & Computer Engineering
University of Louisville
Louisville, Kentucky

December 2022

Copyright 2022 by Danming Wei

All rights reserved

DESIGN, EVALUATION, AND CONTROL OF NEXUS: A MULTISCALE ADDITIVE MANUFACTURING PLATFORM WITH INTEGRATED 3D PRINTING AND ROBOTIC ASSEMBLY

By

Danming Wei
B.S., Dalian Jiaotong University, 2011
M.S., Western Kentucky University, 2016
M.S., University of Louisville, 2018

A Dissertation Approved on

_____11/16/2022_____

by the following Dissertation Committee:

____

Dan O. Popa

____

Cindy K. Harnett

____

Kevin Walsh

____

Thad Druffel

ACKNOWLEDGMENTS

I would first like to thank my supervising professor Dr. Dan O. Popa for constantly motivating and encouraging me, and for his extensive guidance and continuous support for my Doctoral degree study and related research. In addition, I would also like to thank Dr. Kevin Walsh, Dr. Cindy K. Harnett, and Dr. Thad Druffel for serving on my dissertation committee.

I am thankful to the Department of Electrical and Computer Engineering at the University of Louisville for providing me with the Grosscurth Scholarship and the Dissertation Completion Award to support my study and help me complete my Ph.D. degree. I would like to thank the MRI project team, without their efforts and contributions, the NeXus system will not be accomplished. Special gratitude to Dr. Andriy Sherehiy for his kindly guidance and patience to help me complete many tasks in the MRI project. I must mention the help I received from Douglas Jackson, Dr. Ruoshi Zhang, Dr. Ji-Tzuoh Lin, Dr. Alireza Tofangchi, and Jordan Dowdy, who not only gave me practical suggestions in hardware design but also provided diverse simulation results and excellent figures of experimental results for my dissertation and papers of conference and Journal.

Otherwise, I would like to thank Dr. Moath Alqatamin for his effort in the NeXus state machine user interface development, Dr. Dilan Ratnayake for his help to characterize our Aerosol Jetting printer with a commercial silver ink so that I can achieve excellent printed results with diverse designated structures of skin tactile sensors, and Dr. Chuang Qu for his always friendship to encourage and support my research and life.

I am grateful to all staff and students in the Next Generation Systems (NGS) research group and Louisville Automation and Robotic Research Institute (LARRI) for all the support and friendship that they have given to me. I wish to show my gratitude to all UofL MNTC staff: Julia Aebersold, Evgeniya Moiseeva, Jasmin Beharic, Curt McKenna, and Michael Martin for their help in training instruments in the cleanroom and suggestions in fabrication tasks.

I truly appreciate the support from my dearest father Chang Wei, mother Lizhi Guo, and fiancée Qiuhua Qin who have encouraged me to move forward to ultimate success. This dissertation is dedicated to them with my whole-hearted love and gratitude.

Last but not least, I would like to thank the National Science Foundation, which provided funding to support our research. Without those fundings, I would not conduct my research and complete challenges and tasks research. The grand numbers are MRI#1828355 and EPSCoR#1849213.

ABSTRACT

DESIGN, EVALUATION, AND CONTROL OF NEXUS: A MULTISCALE ADDITIVE MANUFACTURING PLATFORM WITH INTEGRATED 3D PRINTING AND ROBOTIC ASSEMBLY

Danming Wei

November 16, 2022

Additive manufacturing (AM) technology is an emerging approach to creating three-dimensional (3D) objects and has seen numerous applications in medical implants, transportation, aerospace, energy, consumer products, etc. Compared with manufacturing by forming and machining, additive manufacturing techniques provide more rapid, economical, efficient, reliable, and complex manufacturing processes. However, additive manufacturing also has limitations on print strength and dimensional tolerance, while traditional additive manufacturing hardware platforms for 3D printing have limited flexibility. In particular, part geometry and materials are limited to most 3D printing hardware. In addition, for multiscale and complex products, samples must be printed, fabricated, and transferred among different additive manufacturing platforms in different locations, which leads to high cost, long process time, and low yield of products.

This thesis investigates methods to design, evaluate, and control the NeXus, which is a novel custom robotic platform for multiscale additive manufacturing with integrated 3D printing and robotic assembly. NeXus can be used to prototype miniature devices and systems, such as wearable MEMS sensor fabrics, microrobots for wafer-scale microfactories, tactile robot skins, next generation energy storage (solar cells), nanostructure plasmonic devices, and biosensors. The NeXus has the flexibility to fixture, position, transport, and assemble components across a wide spectrum of length scales (Macro-Meso-Micro-Nano, 1m to 100nm) and provides unparalleled additive process capabilities such as 3D printing through both aerosol jetting and ultrasonic bonding and forming, thin-film photonic sintering, fiber loom weaving, and in-situ Micro-Electro-Mechanical System (MEMS) packaging and interconnect formation. The NeXus system has a footprint of around 4m x 3.5m x 2.4m (X-Y-Z) and includes two industrial robotic arms, precision positioners, multiple manipulation tools, and additive manufacturing processes and packaging capabilities.

The design of the NeXus platform adopted the Lean Robotic Micromanufacturing (LRM) design principles and simulation tools to mitigate development risks. The NeXus has more than 50 degrees of freedom (DOF) from different instruments, precise evaluation of the custom robots and positioners is indispensable before employing them in complex and multiscale applications. The integration and control of multi-functional instruments is also a challenge in the NeXus system due to different communication protocols and compatibility. Thus, the NeXus system is controlled by National Instruments (NI) LabVIEW real-time operating system (RTOS) with NI PXI controller and a LabVIEW State Machine User Interface (SMUI) and was programmed considering the

synchronization of various instruments and sequencing of additive manufacturing processes for different tasks. The operation sequences of each robot along with relevant tools must be organized in safe mode to avoid crashes and damage to tools during robots' motions.

This thesis also describes two demonstrators that are realized by the NeXus system in detail: skin tactile sensor arrays and electronic textiles. The fabrication process of the skin tactile sensor uses the automated manufacturing line in the NeXus with pattern design, precise calibration, synchronization of an Aerosol Jet printer, and a custom positioner. The fabrication process for electronic textiles is a combination of MEMS fabrication techniques in the cleanroom and the collaboration of multiple NeXus robots including two industrial robotic arms and a custom high-precision positioner for the deterministic alignment process.

TABLE OF CONTENTS

ACKNOWLEDGMENTS iii
ABSTRACT v
LIST OF TABLES xi
LIST OF FIGURES xii
CHAPTER I INTRODUCTION 1
1.1 Motivation 1
1.2 Contributions 2
1.3 Dissertation Organization 6
CHAPTER II BACKGROUND AND PROPOSED METHODOLOGY 8
2.1 Additive Manufacturing 8
2.2 Lean Robotic Micromanufacturing 9
2.2.1 LRM inner loop 11
2.2.2 LRM outer loop 11
2.2.3 LRM external loop 12
2.3 Robotic Skin Tactile Sensor Arrays 13
2.4 Electronic Textiles 15
CHAPTER III DESIGN AND ANALYSIS OF NEXUS 17
3.1 Demonstrators 17
3.2 Design of NeXus 18
3.3 Simulation of NeXus 20
3.4 NeXus Control System 21
CHAPTER IV IMPLEMENTATION OF NEXUS 24
4.1 Implementation of NeXus 24
4.2 Precision Evaluation of NeXus 26
4.2.1 Evaluation of 6-DOF robotic arm with X-Y gantry 27
4.2.2 Vibration performance of the frame 38

4.2.3 Precision metrics of the robotic arm and gantry system 40
4.2.5 Evaluation of Custom 6-DOF positioner 49
CHAPTER V DEMONSTRATOR OF NEXUS 52
5.1 Tactile Sensor Fabrication 52
5.1.1 Fabrication of Tactile Sensor in the Cleanroom 52
5.1.1.1 Design of Sensor 52
5.1.1.2 Fabrication Process 53
5.1.1.3 Lamination Process 57
5.1.1.4 Experimental Setup 59
5.1.1.5 Experimental Results and Discussion 62
5.1.2 Fabrication of Tactile Sensor in NeXus 64
5.1.2.1 Kinematic Design and Calibration of NeXus 65
5.1.2.2 Tactile Sensor Design 76
5.1.2.3 Fabrication Process of Tactile Sensor 82
5.1.2.4 Experimental Setup 83
5.1.2.5 Experimental Results and Discussion 86
5.2 Electronic Textiles Fabrication 98
5.2.1 Electronic Textiles Design 99
5.2.2 Simulation of the Grasp Tolerance of MEMS Clamp 103
5.2.3 Fabrication Process of Electronic Textiles 105
5.2.3.1 MEMS Clamps Fabrication Process 105
5.2.3.2 Deterministic alignment process 110
5.2.4 Experimental results 115
5.2.4.1 Robotic Tool Change Process 115
5.2.4.3 Auger Valve Printing 118
5.2.4.4 Releasing Results and Measurement 119
CHAPTER VI CONCLUSIONS AND FUTURE WORK 121
6.1 Conclusions 121
6.2 Future work 125
REFERENCES 127
APPENDICES 132

CURRICULUM VITA 136

LIST OF TABLES

Table 3. 1 Networking requirements for the NeXus system components. 22

Table 4. 1 Eigenfrequency and maximum displacement of different versions of frame design 30
Table 4. 2 Natural frequencies (Hz) of the robotic arm in the motor on and off 39
Table 4. 3 Pose accuracy and repeatability of the robotic arm using a microscope camera 43
Table 4. 4 Pose accuracy and repeatability of the robotic arm using two laser displacement sensors... 45
Table 4. 5 Pose accuracy and repeatability of the robotic arm using a Digimatic® indicator 45
Table 4. 6 Accuracy and repeatability of SCARA and RTU 48
Table 4. 7 Specifications of the custom 6-DOF positioner.. 51

Table 5. 1 Resistance measurement of two sensor arrays of a pair before lamination 63
Table 5. 2 IAI linear stage travel for each station. 69
Table 5. 3 Distances between fiducial to the center of pad-3 and pad-4 in CAD model and measured samples 75
Table 5. 4 Offsets of the starting pointing to the center of pad-4 and the endpoint to the center of pad-3 75
Table 5. 5 Calibration precision of the sensor printing 76
Table 5. 6 Mechanical and electrical properties of the materials. (Table acknowledgment: Ji-Tzuoh Lin) 80
Table 5. 7 length of MEMS clamp finger and corresponding percentage of overlap or collision of Mems clamps. 101

LIST OF FIGURES

Figure 2. 1 Design principle of Lean Robotic Micromanufacturing (LRM). 10

Figure 3. 1 The dimension of the entire NeXus system.. 19
Figure 3. 2 The CAD design of the NeXus system and subsystem distribution............... 20
Figure 3. 3 The simulation interface of the NeXus system in the LabVIEW® environment. 21
Figure 3. 4 the NeXus networking diagram.. 22
Figure 3. 5 NI PXI real-time control system.. 23

Figure 4. 1 OPTOMEC Aerosol Inkjet printer; 2. Stationary 3D printer; 3. PicoPulse deposition station; 4. IPL sintering station; 5. Microassembly station; 6 Custom 6-DOF positioner.. 25
Figure 4. 2 Tool change station and PNP station... 25
Figure 4. 3 NeXus controller rack.. 26
Figure 4. 4 The isometric view of the custom frame with mounted X-Y gantry and 6-DOF robotic arm 27
Figure 4. 5 Initial version and final version of the custom frame.................................... 29
Figure 4. 6 Different versions of the frame with the improvement of structures. (Figure acknowledgment: Alireza Tofangchi)... 29
Figure 4. 7 Two laser displacement sensors measure the natural frequency of the robotic arm 31
Figure 4. 8 Hardware setup for evaluation of robotic arm by the microscope camera..... 33
Figure 4. 9 Micron-size feature for visual measurement 34
Figure 4. 10 Point location in the first mode 35
Figure 4. 11 Point location in the second mode... 36
Figure 4. 12 Two laser displacement sensors were used to measure the pose performance 37
Figure 4. 13 A Digimatic® indicator used to measure the pose performance.................. 37
Figure 4. 14 Natural frequencies of the robotic arm at motor on and off 39
Figure 4. 15 The CAD model of the 6-DOF positioner, featuring a coarse X, fine XYZ translation, tilt, and rotation 50
Figure 4. 16 Evaluation of 6-DOF positioner with a crossing template 50

Figure 5. 1 Star-shaped sensor array mask design for 4-inch wafer and dimensions of a sensor array, single sensor, and single beam. 53
Figure 5. 2 Skin sensor fabrication process in the cleanroom. 56

Figure 5. 3 The fabricated sensor array with a Ti protection layer. 57
Figure 5. 4 Lamination process for the double-layer skin sensor array. 59
Figure 5. 5 Tactile sensor load testing station. 60
Figure 5. 6 Top: a pair of sensors representing two potentiometers in series connection; bottom: strain sensing circuit diagram. REEP, REFN pins are the reference voltage, AVDD is the positive supply and the AVSS is the negative supply. 61
Figure 5. 7 Sensors and electrodes arrangement of a sensor array. 62
Figure 5. 8 Strain gauge performance of sensor pair with variable load applied on No. 5 sensor 64
Figure 5. 9 Hardware on a long optical table: 1. OPTOMEC® Aerosol Inkjet printing station; 2. 3D FDM printing station; 3. PicoPulse® inkjet deposition station; 4. Intense Pulse Light (IPL) station; 5. Microassembly station; 6. 6-DOF positioner with the printed sample. 66
Figure 5. 10 Coordinate the frame and distribution of each subsystem for the skin sensor fabrication process in the NeXus. 66
Figure 5. 11 The top view of the alignment of the center of the sample chuck to the printer head. 68
Figure 5. 12 Alignment of sample chuck center and OPTOMEC® printer nozzle. 69
Figure 5. 13 An arbitrary point moves to the center of the sample chuck with the desired orientation. 70
Figure 5. 14 Fiducial mark location before and after visual servoing adjustment. 73
Figure 5. 15 Dimension of fiducial and contact pads on the substrate 74
Figure 5. 16 Dimension of the starting point on pad-4 of sample-3. 74
Figure 5. 17 Design of the tactile sensor with two individual strain gauge structures. 77
Figure 5. 18 Design principle of the combined structure tactile sensor. 79
Figure 5. 19 Simulated results of the tactile sensor via COMSOL®. (Figure acknowledgment: Ji-Tzuoh Lin) 81
Figure 5. 20 Printed tactile sensor on the Kapton® substrate. 83
Figure 5. 21 Linkam Scientific Instruments® Analysa-LTS350 temperature chamber. 84
Figure 5. 22 Single sub-indenter load test. 85
Figure 5. 23 Multiple sub-indenters directional load test. 85
Figure 5. 24 2x2 sensor array load test. 86
Figure 5. 25 A) Sensor's structure resistance dependence on the sintering time at 200°C and 0N load; B) variation of resistance difference between sensor's structures with the sintering duration time. (Figure acknowledgment: Andriy Sherehiy) 87
Figure 5. 26 Temperature performance of the radial and arc structures. 89
Figure 5. 27 The changes of resistance and the sensitivities of the radial structure and arc structure under the single force 1N and 2N. (Figure acknowledgment: Ruoshi Zhang) 92
Figure 5. 28 The changes in the resistance of the radial and arc structures under the ladder force 0-0.5-1-1.5-2N. (Figure acknowledgment: Ruoshi Zhang) 92
Figure 5. 29 The sensitivities of the radial and arc structures under the ladder force 0-5.5N with a step of 0.25N. 93

Figure 5. 30 Characterization of tactile sensor printed on the Kapton® substrate with indicated 5 different sub-indenter locations for 4 directions 0°, 45°, 90°, and 135°. 94
Figure 5. 31 Load responses of directional force test. 95
Figure 5. 32 2x2 sensor array with 7x7 sub-indenters PDMS cover. 96
Figure 5. 33 The single sensor sensitivity's responses of the radial and arc structures when the load comes from different directions. (Figure acknowledgment: Jordan Dowdy) 97
Figure 5. 34 The Gaussian distribution of sensitivity's responses of the radial and arc structure in a 2x2 sensor array. (Figure acknowledgment: Jordan Dowdy) 97
Figure 5. 35 Red crosses mean MEMS clamps overlap or collide; green crosses mean MEMS clamps without overlap or collision; (e) Missed electrical intersections at fiber distorted turnings circled in yellow. (Figure acknowledgment: Sushmita Challa)......... 101
Figure 5. 36 (a) The image of the fabric structure. (b) (c) MEMS gripper and alignment mark distribution for mask design. (d) Single MEMS gripper structure dimension. (e) MEMS grippers align on the intersections of the fabric. (f) Alignment mark dimension. 103
Figure 5. 37 2500µm length MEMS finger bends in half circle and a 600µm diameter fiber. 104
Figure 5. 38 left: the fiber reaches the maximum y-height for grasping; right: the fiber reaches the maximum x-axis for grasping. 105
Figure 5. 39 A simple demonstration for the MEMS fingers fabrication process.(a)Si wafter with SiO_2 layer; (b)Photolithography for MEMS finger pattern; (c) Sputter Au layer; (d) lift-off process; (e) Photolithography for SiO_2 etching pattern; (f) Etch SiO_2 around MEMS fingers;(h)Etch Si isotropically to pop up the MEMS fingers. (Figure acknowledgment: Sushmita Challa) 107
Figure 5. 40 1st generation hardware for deterministic alignment process of textiles with MEMS grippers.. 108
Figure 5. 41 Metal frame clamping fabric material on the standing; (b) 4-inch wafer sample chuck carrying the wafer with MEMS clamps; (c) Metal frame coupling with 4-inch wafer sample chuck.. 110
Figure 5. 42 Design of the NeXus system manipulators for fiber and MEMS clamps handling and alignment.. 113
Figure 5. 43 An image of the NeXus system in our lab.. 114
Figure 5. 44 Flow chart of the deterministic alignment process.................................... 114
Figure 5. 45 The alignment mark aligns with the specific intersection after the visual servoing process.. 116
Figure 5. 46 Alignment results of MEMS grippers with fiber intersections. 116
Figure 5. 47 The alignment errors in translational and rotational directions.................. 117
Figure 5. 48 The Auger valve dispenses the SU-8 photoresist on the fabric.................. 118
Figure 5. 49 Releasing results of MEMS microgrippers. (Figure acknowledgment: Chuang Qu).. 119
Figure 5. 50 Measurement of conductive fibers from a microgripper pad. 120

CHAPTER I INTRODUCTION

1.1 Motivation

Off-the-shelf additive manufacturing processes and equipment have dedicated functionality, limited achievable print geometries, and materials, and require human intervention to fixture, remove, and transport printed parts from one tool to another. Manufacturing processes of complex multiscale devices or systems usually require multiple steps and procedures that cannot be handled by today's 3D printers. In research and development environments, samples are typically transferred by human beings among different platforms in different locations, which likely results in more errors, a long process time, and a low yield of R&D samples. The fabrication instruments used in these R&D environments, for example, in university cleanroom, have well-defined functionalities and little flexibility in fabricating the desired samples. Research staff must often consider the use of multiple instruments and processes in order to complete the fabrication of R&D samples. In a manufacturing environment, however, products are often integrated with advanced automated manufacturing systems, robots, and controllers that integrate functionalities and maintain quality and yield. The automated control system integrates multiple instruments that are with different communication protocols, calibrates the fabrication precision, synchronizes multiple instruments, optimizes the distribution of hardware and fabrication process, and sequences the operation of instruments on the manufacturing line.

The motivation of this work is to create an “All-in-One” R&D platform for additive manufacturing instruments and processes integrated with robotic assembly techniques, which has high flexibility and can manufacture multiscale systems with high precision and high yield in a manufacturing environment. The multiscale nature of the systems targeted by our work includes complex products with Macro-Meso-Micro and even Nano scale components covering the dimensional range between 1m to 100nm.

As a result of our unique effort detailed in this thesis, a novel custom robotic platform -NeXus- has been designed, evaluated, and controlled as a multiscale additive manufacturing platform with integrated 3D printing and robotic assembly. The NeXus was evaluated during the manufacturing of miniature demonstrators, such as tactile robot skin sensors and wearable MEMS sensor fabrics. The NeXus system integrates several high-precision additive manufacturing instruments, such as an Aerosol inkjet printer, a piezoelectric inkjet dispensing system, a microassembly station, an Intense Pulse Light (IPL) sintering system, as well as two custom 3D FDM printers. The NeXus also integrates two industrial robotic arms with 6 degrees of Freedom (DOF) and 4-DOF, and a custom 6-DOF positioner. Operational flexibility for the NeXus is ensured by the use of multiple manipulation tools, such as electrical gripper, auger valve dispensers, pick and place (PNP) nozzles, ultrasonic welding heads, and dual-head 3D FDM printers, all operated within the placed in the tool change station of the NeXus system.

1.2 Contributions

Given the complicated hardware requirements of the NeXus platform, supporting the operation of around 50 degrees of freedom, it is extremely challenging to design and optimize the whole platform in order to accomplish the required precision and throughput.

During the design of the NeXus we had to consider aspects of alignment, calibration, integration, and synchronization among different instruments, processes, and positioners, and optimize the sequencing of operations to achieve needed precision. Thus, the contribution of this research is to propose and demonstrate a new design methodology for heterogeneous multiscale MEMS devices and systems, called the Lean Robotic Micromanufacturing (LRM) approach. Specifically, the thesis contributions are summarized below:

a) The LRM approach starts with the Inner Loop design optimization step, which takes into account the conceptualization of the multiscale robotic platform and visualizes it using Computer-Aided Design (CAD) models, as well as complex animation and process visualization using a "digital twin" that can study the impact of positional and size uncertainties to the assembly yield. The purpose of the inner-loop design step of LRM is to reduce the hardware implementation risk, analyze the impact of robot precision and part tolerances on the assembly yield, and obtain estimates of manufacturing throughput. The inner-loop step can also lead to production yield guarantees given tolerance bounds, optimization and visualize the whole manufacturing process, and selection of hardware requirements.

b) The second step of our LRM approach called the "Outer-Loop" involves instruments and hardware selection according to tolerance budgets established in the inner loop. During this step, I communicated and discussed with numerous hardware vendors and manufacturers the availability, compatibility, and reliability of their products for integration within the NeXus. Custom fixtures have also been designed and fabricated taking into account the required process tooling. At the end

of these discussions, appropriate hardware was selected and purchased by our team and used to complete the assembly of the NeXus system. Once NeXus operation was accomplished, the outer-loop LRM design steps evaluated the precision of the custom and multi-degrees of freedom robots and positioners. Numerous adjustments of hardware configurations, calibration, and implementation of automation and control sequences were undertaken during the outer-loop design step. During this step, I was continuously involved in the integration, synchronization, and automated control of multi-functional instruments of the NeXus system, while I also figured out instrument communication protocols, in-situ sensing, and debugged platform compatibilities issues. The NeXus control system was integrated under National Instruments (NI) LabVIEW real-time operating system (RTOS) and a LabVIEW State Machine User Interface (SMUI). The SMUI accomplishes the synchronization of various instruments and sequencing of additive manufacturing processes for different tasks with the help of human operators. The operation sequences of each robot along with relevant tools were programmed in a safe mode to avoid crashes and damage to hardware during operation, as well as accomplish human operator safety.

The result of the outer-loop LRM design step includes the integration, synchronization, and automated control of additive manufacturing, part transport, and finally functional testing of several demonstrator “prototypes”.

c) The third LRM design step, the External Loop, involved the design of the process, programming of the control, calibration, improvement, and implementation of the manufacturing processes of the demonstrators. During this step, I conducted and

developed the manufacturing processes of several demonstrators including robotic skin tactile sensor arrays and electronic textiles. To fabricate these demonstrators, it was necessary to tune process parameters, the program of the control, calibration, and synchronization of fabrication sequences, and test the dimensional tolerance and the functionality of the resulting prototypes.

d) This thesis details scientific contribution to the design, fabrication, and evaluation of two demonstrators, including 1) "robot skins" comprising of piezo-resistive tactile printed on flexible substrates with the NeXus that can serve as large area touch sensors for future collaborative robots and 2) "electronic textiles" comprising of woven conductive fibers interconnected with the help of MEMS microclamp arrays, that need to be handled and aligned with the required precision using three collaborating NeXus robots.

As a result of the LRM design process, several subsystems including additive manufacturing processes, robots, and metrology tools were integrated into the NeXus and used to manufacture demonstrators, The NeXus subsystems include:

1) An Aerosol Jetting print station for depositing multi-material features (lines) minimum 20-micron width and hundred nanometers thick.
2) An intense pulse light (IPL) photonic sintering station for curing thin and thick films deposited with the Aerosol Jetting print station.
3) An additive 3D printing station including a fixed dual-head fused filament molding (FDM) printer, and a movable 5-DOF dual-head FDM printer mounted on an industrial robot.

4) A custom microassembly station (MAS) for microrobots assembly, that can be used to assemble mobile cm-size microcrawler microrobots.
5) A custom ultrasonic print head configured for metal interconnect formation for wire bonding. This custom end-effector can be used for wire bonding with a Silicon substrate and a soft ferroelectric polymer (PVDF) actuator surface wire embedding.
6) A fiber loom station (FLS) to create electronic textiles (E-textiles) for wearable devices. The demonstrator is to create a functionalized fiber network whose manufacturing process combines microstructures (clamps or grippers) fabrication on the Si wafer in the cleanroom and multi-robot collaboration for precise alignment of microstructures and fiber textile intersections.
7) The NeXus has other end-effector tools, including microgrippers, dispensers, probers, and laser cutting or curing tools that are designed and employed to assist the subsystems to complete the demonstrators.

The research results detailed in this thesis are supported by numerous publications in conferences and journals in APPENDICES.

1.3 Dissertation Organization

This dissertation is organized as follows: Chapter 2 includes a background and literature review on additive manufacturing, Lean Robotic Manufacturing, and the demonstrators of the NeXus: skin tactile sensor and electronic textiles (E-textiles). Chapter 3 introduces the demonstrators manufactured by the NeXus system and presents the design of the NeXus system in CAD model and simulation results in the LabVIEW environment by following the LRM designed principles. Chapter 4 describes the implementation of the NeXus system and the precision evaluation of custom robots and positioners. Chapter 5

presents demonstrators manufacturing processes in the NeXus system and discusses the manufacturing results, Finally, Chapter 6 presents conclusions and future work on the development and completion of demonstrators' manufacturing processes in the NeXus system.

CHAPTER II BACKGROUND AND PROPOSED METHODOLOGY

2.1 Additive Manufacturing

Additive manufacturing technologies are an emerging approach to creating 3D objects and have widely been employed in various fields, such as medical implants [1], transportation [2], aerospace[3], energy, consumer products, etc. Technically, additive manufacturing is the process to build something up by one layer at once, but many times, it refers to 3D printing techniques using a solid filament. In the 1980s, additive manufacturing started to be used for developing prototypes, which is known as rapid prototyping because it allowed people to bring to file CAD models very quickly without the complex processes employed by traditional subtractive manufacturing such as tooling, cutting, and machining. Over the past two decades, AM processes have been investigated and developed including Fused Deposition Modeling (FDM) [4], Stereolithography (SLA) [5], Laser Metal Deposition (LMD) [6], Laminated Objective Manufacturing (LOM) [7], Selective Laser Sintering (SLS) [8], and Three Dimensional Printing (3DP) [9]. Compared with subtractive manufacturing, additive manufacturing techniques provide more rapid, economical, efficient, flexible, reliable, and complex manufacturing processes. Based on various materials, like polymer filament [like Polylactic Acid (PLA), Polycarbonate, and acrylonitrile-butadiene-styrene (ABS)], metal/ceramic/polymer powders, UV curable resins, carbon fiber, graphene, and concrete, 3D objects can be created in multiple scales from micro and nanostructures to large buildings.

However, traditional additive manufacturing platform including 3D printing and rapid prototyping has limited flexibilities of hardware to create restricted products due to the instruments' functionalities. For multiscale and complex products, they have to be printed, fabricated, packaged, and transferred among different additive manufacturing platforms in different locations, which leads to high cost, long process time, and low yield of products.

2.2 Lean Robotic Micromanufacturing

The Lean Manufacturing concept evolved from Japanese manufacturers, especially at Toyota in the 1930s, who aimed to reduce inventory costs and wastage and increase productivity, quality, and profit. In modern industries, the main goal of Lean Manufacturing systems is to manufacture products of higher quality at the lowest cost and in the least time by eliminating waste [10]. Lean Manufacturing is based on measuring output statistics of manufactured products, whether in terms of dimensional tolerance or other performance metrics and ensuring that most process steps produce a yield exceeding 99%, within the six-sigma band. In this research, I propose to employ a novel concept, the Lean Robotic Micromanufacturing (LRM) methodology as a way to design multi-robot manufacturing cells with guaranteed production metrics. LRM is rooted in Lean Manufacturing, but it is uniquely applied to manufacture at small scales such as meso or micro scales. Research at the Next Generation Systems Lab (NGS) has been advocating for the last two decades that design for manufacturing (DfM) along with modular, open, design methodologies must be employed concurrently when designing both products and production tools at the microscale [11-14].

At small scales, stringent precision requirements increased tolerance to dimension ratio of components, low signal vs. noise ratio of sensors, and increased environmental influences combine to increase production system costs and time to manufacture while decreasing the yield and the reliability of miniaturized products [15]. The LRM approach keeps costs down by employing an evolutionary manufacturing cell optimization process from design databases and masters the uncertainties in the manufacturing system by monitoring key yield-related process variables. The design principle has three loops: inner loop, outer loop, and external loop depicted in Figure 2.1.

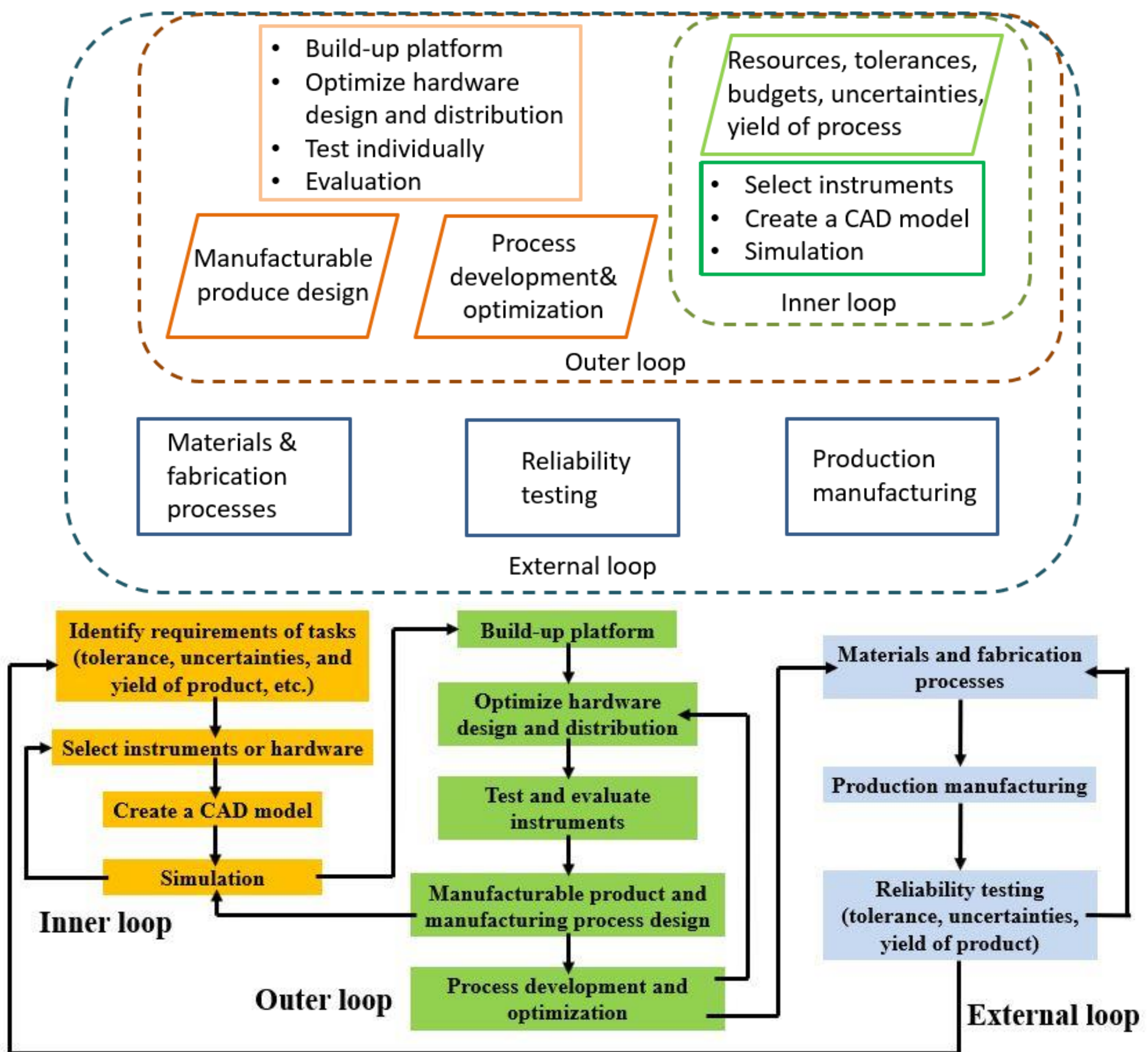

Figure 2. 1 Design principle of Lean Robotic Micromanufacturing (LRM).

2.2.1 LRM inner loop

In the LRM inner loop, at first, it is significant to establish a nonzero assembly yield given product design to expect the yield of products depending on the tolerances and uncertainties of instruments, such as robots, sensors, tools, and manufacturing process (grasping, bonding, and printing). According to the expected tolerances and uncertainties, specific instruments and their accessories are selected to match the required manufacturing yield of products. After selecting the proper instruments, it is necessary to create a CAD model of the integration of all the instruments to visualize the whole system. It is convenient to modify the distribution of instruments and optimize their functions in the CAD model. Furthermore, a more advanced type of model, a "Digital Twin" is usually created to study the impact of uncertainties in the system on the overall tolerance budget. This digital twin can realistically imitate the manufacturing process and can be used to anticipate the production throughput of the system, sequence the production, and evaluate the impact of hardware or configuration changes. In past research at NGS, several studies [16-20] have modeled the propagation of positional uncertainties through robotic chains, and simulated these uncertainties within the digital twin, in order to predict the production yield. Past work included Monte-Carlo simulations with an analytical product of exponential formula and Interval Analysis. Using this method, the designer can check and validate the manufacturing processes, and reduce prototyping costs and integration time through its reconfigurability and hardware cost optimizations.

2.2.2 LRM outer loop

Based on the inner loop digital twin model, the selected positioner and process instruments should be selected, purchased, and assembled. However, real assembled

hardware is usually different from the exact nominal designs of the CAD model. In addition, there are lots of uncertainty sources for the real workspace due to floor vibration, structure stiffness, fixture tolerances, and so on. Optimization of the hardware design and distribution after assembly is necessary in order to optimize the multi-robot cell configuration. During this step, each instrument and positioner has to be tested, including basic functionality and advanced functionality depending on the application must also be developed. Evaluation of the whole system, especially for the custom-designed instruments, can obtain additional parametric data that can be used to reduce uncertainty using calibration. Meanwhile, during this step, we start to design and optimize manufacturing processes combining them with robotic assembly steps. In past work [21-23] from NGS, this process was described for several multi-robot cells, including the M^3 [24], designed to assemble optoelectronic MEMS, and μ^3 [25] designed to assemble micro-optical benches, and N^3, comprising of a microrobotic wafer aiming to put together nanoscale products.

2.2.3 LRM external loop

In the LRM external loop, the multi-robot system is ready to manufacture the product depending on processes evaluated in the LRM outer loop and guaranteed to achieve a non-zero yield. The selection of materials and processes should satisfy product reliability requirements determined in LRM inner loop. However, additional experiments, testing, and reliability studies of the resulting demonstrators must be implemented in order to verify whether the manufacturing results are acceptable. During these steps, designers can adjust both process parameters and also materials employed in the demonstrator manufacturing, and product functional testing is carried out to validate that the resulting products are

reliable. Past examples of external loop studies [26, 27] were carried out with demonstrators of the M^3 and μ^3.

2.3 Robotic Skin Tactile Sensor Arrays

For decades, artificial robotic skin has attracted interest among researchers, especially for applications in physical human-robot interaction and autonomous manipulation [28, 29]. The sense of touch enables robots to physically interact with their environment and people, in applications such as grasping manipulation [30] and full-body haptic sensing [31]. Many researchers have investigated robotic skins design that matches or outperforms humans, incorporating temperature and pressure sensors using different transducer mechanisms including capacitive sensing [32], conductive fabrics [33], infrared sensors [34], or semiconductor strain gauges [35]. However, after over 30 years of research, numerous challenges related to the fabrication and integration of skin sensors with robots remain [36, 37].

In the past several years, the NGS group at UofL has been investigating and developing robotic skin sensor arrays based on semiconductor organic materials and addressing challenges in design, simulation [38], fabrication [39], packaging [40], electronic transducers, interfaces to robot controllers, and human-robot interaction algorithms [41]. The base sensing material used in our research is the organic semiconductor polymer Poly (3, 4-ethylene dioxythiophene)-poly(styrene sulfonate) or PEDOT: PSS, which has been printed over flexible Kapton substrate using several techniques. The active sensor material changes resistance in response to strain and it is consistent with a 20:1 gauge factor [38].

In [42], Electro-Hydro-Dynamic (EHD) ink-jetting was used to print mm-size interdigitated strain gauge structures with 10-micron feature resolution. Under a high-voltage electrical field working environment, the EHD print head has to be a specialized nozzle. However, the inks for EHD printing must have special formulations to satisfy conductivity and viscosity requirements, and the printing process is highly serial, for example, one gauge is printed at a time. In [42], the sensor geometry included interdigitated designs, resulting in directional pressure sensitivity in the vicinity of the sensor.

In [39], we investigated a scalable, cleanroom-compatible fabrication technique using spinning and wet lift-off photolithography. In addition, the sensor geometry employed was a star-shaped strain gauge structure incorporated in a 4x4 skin sensor array. The star-shaped sensor structure had a circular symmetric pressure response and was thoroughly characterized by indentation experiments.

The wet lift-off photolithographic method improved the deposition process when compared to EHD printing but required Acetone to lift off unnecessary sensing film. In addition, the process required spinning PEDOT: PSS solution diluted with Methanol with ratios between 1:1 and 1:4 [39]. During the process, PEDOT: PSS residue cannot be removed perfectly but remains on the sensing areas, therefore affecting the conductivity and sensitivity of the sensors. In particular, if arrays of tactile sensors are produced, they will have wide variations in resistance, which require additional lamination and calibration procedures. Later, in [43], we developed a new dry etching photolithographic process that can repeatably deposit uniform PEDOT: PSS sensing layers. The process does not require Methanol additives. Instead, a new formulation of PEDOT: PSS with Dimethyl sulfoxide (DMSO) and Polyvinylpyrrolidone (PVP) was investigated. The presence of the new

additives increases the tactile sensors resistance and results in better sensitivity. In addition, to protect the sensing area, a physical cap was created to deposit a protective Titanium layer. As a result, the lift-off process which contributed to residue on the sensing elements was replaced with dry etching and results in more repeatable sensor characteristics.

2.4 Electronic Textiles

Textile sensors and actuators are applied to wearables such as joint angle measurement sleeves, sensor gloves, and other accessories to track body movement and shape. Various electronic fabric manufacturing techniques have been devised which employ traditional methods such as knitting [44], weaving [45], embroidery [46], or braiding; finished textiles can also be altered with various techniques like dip coating [47], laminating [48], electroplating [49], physical vapor deposition (PVD) [50], chemical polymerization [51], and screen printing [52] methods to coat the surface of the textile. Mechanical characteristics of E-Textiles such as light weight, flexibility, conformability, breathability, permeability, porosity, compressibility, and texture will depend on the manufacturing technique weave/knit/non-woven/composite, type of smart/conductive fibers and yarns used, fiber/thread count, yarn twist, fiber spacing, embedded devices, printing/coating/deposition of conductive material, and loading [53]. For instance, knitted fabric is characterized by low linear density, higher elongation, and small bending resistance while woven structures exhibit higher strength [47]. Such research is driven by the goal of adding electronic functionality while maintaining the desired mechanical characteristics of textiles.

Fiber substrates present unique properties such as permeability, flexibility, conformability, and breathability compared to conventional thin-film substrates on which

electronics are generally built. Various methods from building functional fiber systems [54, 55] to embedding electronics into 2-D fabric structures [56], electronic textile manufacturing techniques are very much populated in literature. Micro Electromechanical systems structures integrated functional fiber assembly systems find applications in textile circuitry [57], wearable sensors [58], switchgear systems [59], and MEMS packaging on mesh substrates [60]. Functional fiber systems can offer desirable electrical fiber traces, and ohmic fiber crossovers, that can enable textile circuit routing which can implement fabric-based logic circuits, multiplexers, memory devices, wire electrochemical transistors (WECT) [61], and pressure sensors [53].

CHAPTER III DESIGN AND ANALYSIS OF NEXUS

3.1 Demonstrators

According to the LRM design inner loop, demonstrators need to be determined and all requirements of demonstrators should be addressed, such as product scales, design tolerances, uncertainties, and expected yield. Based on the requirements, needed specific instruments were selected to satisfy the requirements of demonstrators manufacturing processes. To design the NeXus system, we proposed two initial demonstrators: skin tactile sensors and electrical textiles.

For the skin tactile sensor, recently, we used MEMS fabrication techniques to fabricate a 4x4 skin sensor array in the UofL cleanroom. The fabrication process has many steps with specific instruments, which results in high costs and a long process time. While the repeatability of fabricated results of skin sensors could not be guaranteed due to the multi-steps and manual operations involved. The recent skin sensor fabrication process leads to sensors patterned over 300 nm thick with 20μm width gold traces on a 100μm thick Kapton® sheet. PEDOT: PSS as an organic piezoresistive polymer is deposited and patterned on the sensing areas of sensors. The density of patterned structures enhances the ability to measure the piezoresistive behavior of the PEDOT: PSS using shorter distances among measurement points. Consequently, higher densities of electrical contacts, thinner PEDOT: PSS films, and additional ink additives result in higher sensor sensitivities [41]

A lamination process is needed to create a double-sided sensor for temperature compensation and enhancing sensitivity. In the NeXus system, we proposed a new skin sensor fabrication process by using an Aerosol Inkjet printing instrument to print conductive traces on the flexible polymer substrates, like Kapton® sheet, and then sintering with an intense pulse light photonic sintering tools with an intense pulse (1-3kW) of white light (250nm – 1000nm) that can be distributed over a very large area. The PEDOT: PSS solution will be deposited with a PicoPulse dispensing tool to the desired location with automated control. The new skin sensor fabrication process with the NeXus system will lead to short manufacturing process time and all operations are under automated mode without any human errors.

For electronic textiles, a loom station will be employed to make multi-scale fiber textiles with conductive and non-conductive material. To manufacture wearable textile sensors, functional structures need to be added or embedded into the fabric structures. MEMS microgrippers with electrical properties are fabricated in the cleanroom. The NeXus system will be utilized to align the MEMS microgrippers with intersections on the fiber textile with multi-robot collaboration to make the microgrippers grasp the intersections of the textile with a releasing process in the cleanroom after the alignment process. In this manufacturing process, multi-functional textile sensors can be fabricated for wearable sensors or soft robots.

3.2 Design of NeXus

Based on the lean robotic manufacturing framework design principle, at first, a NeXus CAD model was prototyped and created using Solidworks®. Before purchasing the NeXus hardware, it is significantly helpful and necessary to define the dimension of each

piece of hardware, such as the entire frame, RTU (robotic transport unit) standing, overhead gantry, and the heights of two optical tables (shown in Figure 3.1), as well as the distributions of two industrial robotic arms and subsystem stations in the NeXus system (shown in Figure 3.2) according to the measured available room for the NeXus system. The 6-DOF robotic arm was ceiling mounted on a 2.8m x 2.55m overhead large X-Y gantry which can assist the 6-DOF robotic arm to reach everywhere inside the frame and make it achieve the maximum workspace. The 4-DOF robotic arm was floor mounted on a 2.3m single-axis RTU standing which can assist the 4-DOF robotic arm to transform between two optical tables to complete multiple tasks.

Also, the NeXus has several subsystems, such as an aerosol jetting print station, a 3D printing station, a PicoPulse dispensing station, an intense pulsed light photonic sintering station, a microassembly station, a fiber weaving station, and a tool change station. They are distributed and very arranged in the NeXus system.

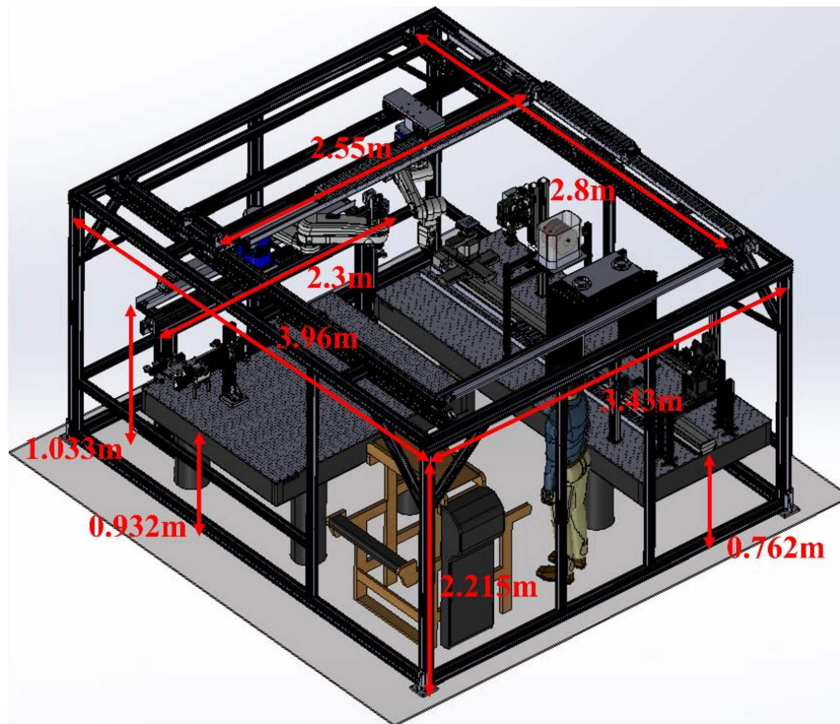

Figure 3. 1 The dimension of the entire NeXus system.

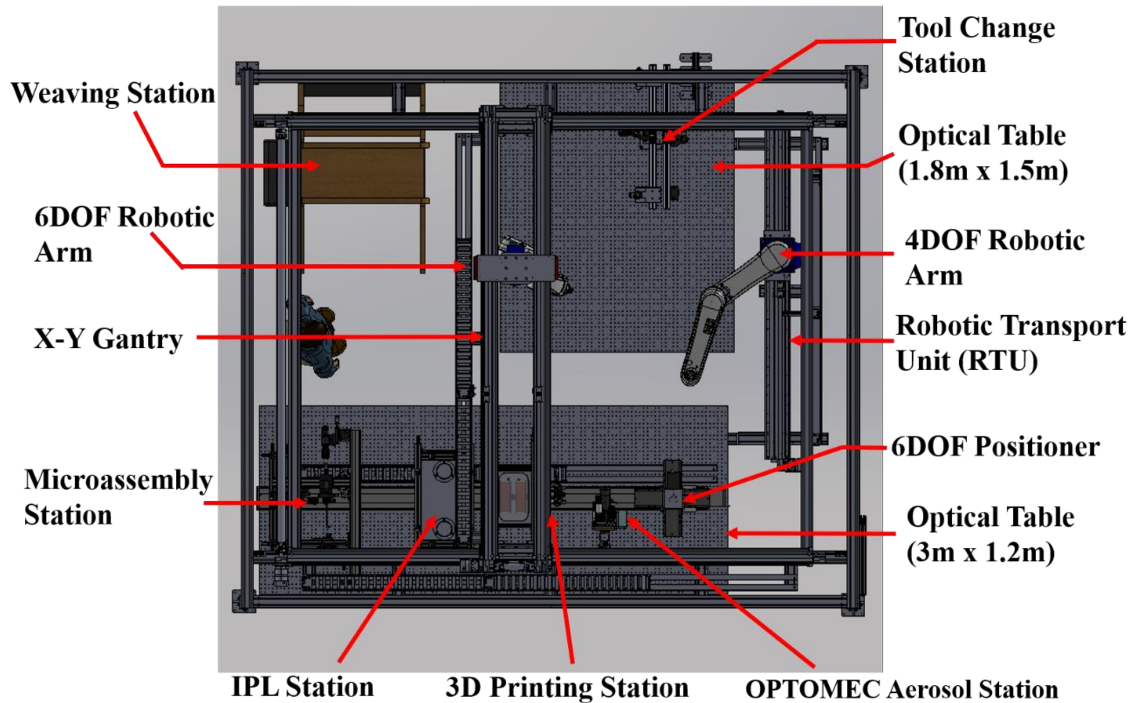

Figure 3. 2 The CAD design of the NeXus system and subsystem distribution.

3.3 Simulation of NeXus

After completion of the NeXus design in the CAD model, a simulation system of the NeXus system was programmed by LabVIEW®. In the simulation program, all the hardware was simplified and imitated with the same dimension and build up together to match the NeXus design in the CAD model. Figure 3.3 depicts the LabVIEW interface for manually controlling each degree of freedom of motorized stages and industrial robotic arms as well as tool change functions. The stages or industrial robotic arms can be driven by adjusting the corresponding slides and knobs' locations. The auto mode of certain demonstrators is being developed and modified. This simulation system can be used to evaluate, simulate, and test the availability, and flexibility of operations of multiple robots collaboration for the demonstrators.

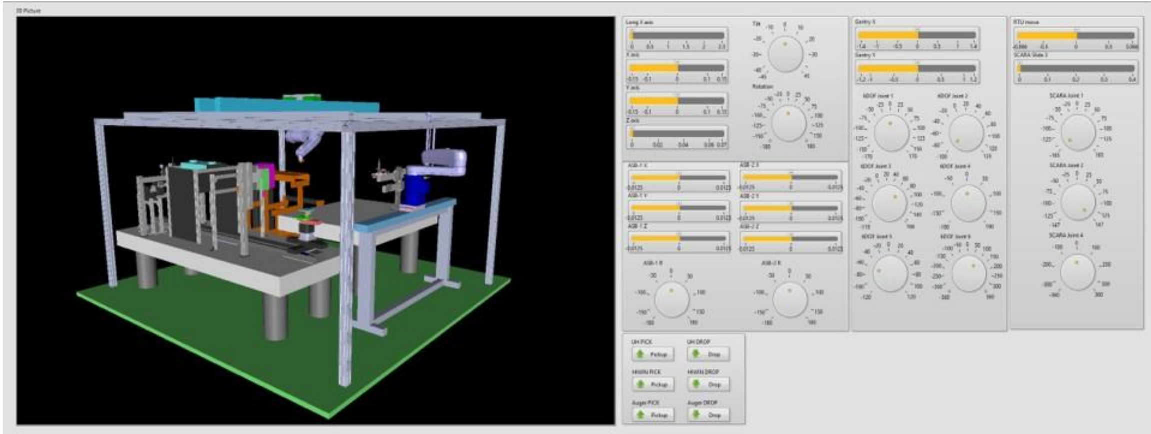

Figure 3. 3 The simulation interface of the NeXus system in the LabVIEW® environment.

3.4 NeXus Control System

Figure 3.4 depicts the networking of NeXus system components, including subsystems stations, positioners, robots, and process tools that must be networked together to an operator workstation. A NeXus system controller will include at least 13 RJ45 Ethernet/EtherCAT, 3 RS232, 1 RS485 connector, and 8 USB connectors.

Using these specifications, we selected National Instruments (NI) PXI series (in Figure 3.5) as a controller for the NeXus running LabVIEW Real-Time OS and used it in tandem with a Windows PC. The PXIe-1085 chassis was selected, along with multiple function modules, such as PXIe-8861 controllers, PXIe-8234 Ethernet interface module, PXIe-4300 analog input module, PXI-8432/4 RS232 serial interface module, PXIe-6602 counter module, PXIe-6509 digital module, and PXI-8433/2 RS485 interface module. Table 3.1 describes the networking protocol available to each tool or positioner system of the NeXus.

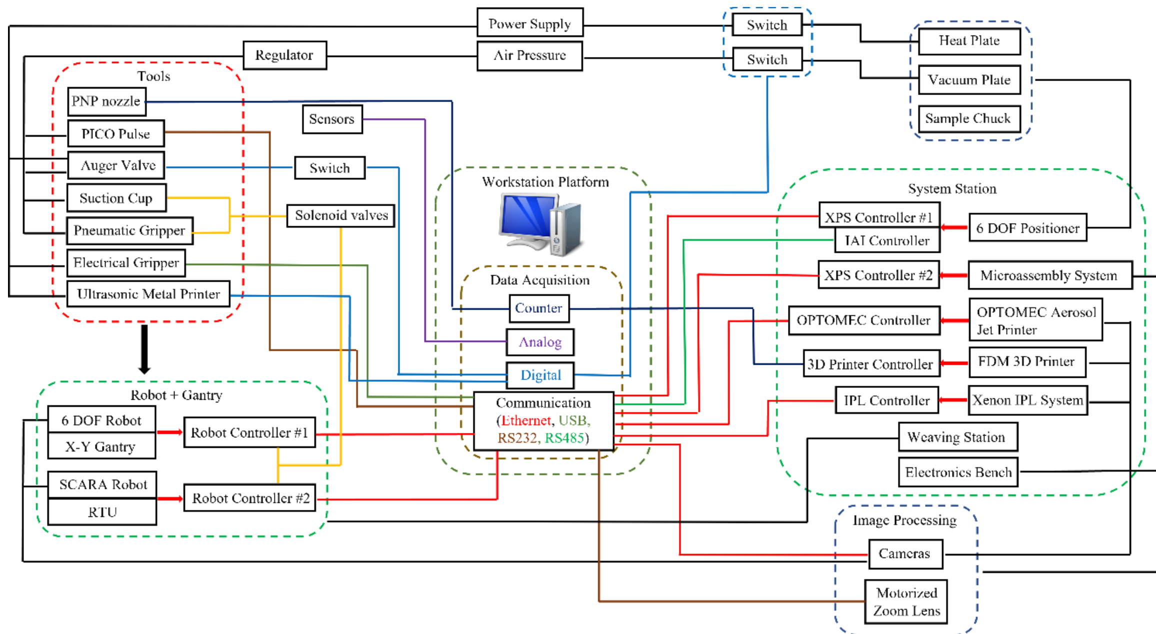

Figure 3. 4 the NeXus networking diagram.

Table 3. 1 Networking requirements for the NeXus system components.

Equipment	Controller	Connect to PC
DENSO-VS6577	DENSO RC8A (1)	RJ45
DENSO-HM40A02	DENSO RC8A (2)	RJ45
Microassembly System	Newport XPS-D8 (1)	RJ45
6 DOF positioner	Newport XPS-D8 (2)	RJ45
Microassembly System & Electronics Bench	Gigabit Ethernet Camera (4)	RJ45 x 4
Compressed Air System	Electro-Pneumatic Regulator	RJ45
	Solenoid Valves System	RJ45
IAI-ISPB Linear Stage	IAI SCON-CA(B)	RS485
OPTOMEC Aerosol Inkjet	OPTOMEC	RJ45, RS232, USB
XENON IPL Sintering Station	IPL Controller	RS232, USB
Nordson PICO Pulse	PICO Pulse Controller	USB
HIWIN Electrical Gripper	HIWIN Controller	USB
3D printer & metalize printer	Microcontroller for Extruders	USB x 2
Two Robotic Arms	Gigabit Ethernet Camera (2)	RJ45 x 2
Motorized Lens	Controller	RS232

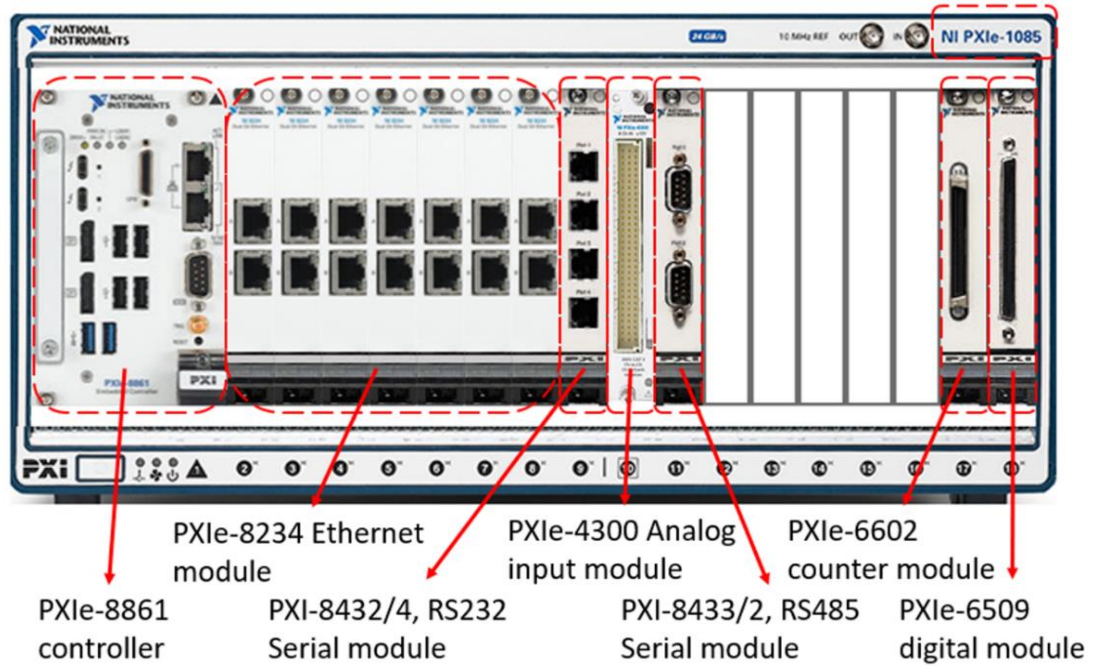

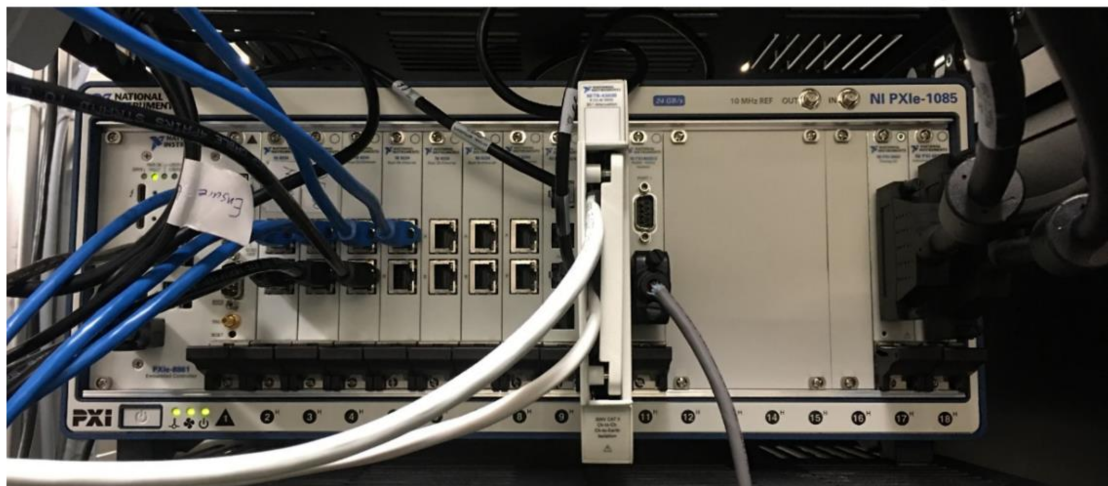

Figure 3. 5 NI PXI real-time control system.

CHAPTER IV IMPLEMENTATION OF NEXUS

4.1 Implementation of NeXus

The NeXus system was prototyped and designed as a novel multiscale additive manufacturing platform integrated with 3D printing and robotic assembly techniques. Thus, all instruments in the NeXus system are served for additive manufacturing and robotic assembly techniques, such as an aerosol inkjet printing station, 3D printing station, PicoPulse deposition station, IPL station, microassembly station, tool change station, PNP station, 6-DOF positioner, and two industrial robotic arms. In addition, various end-effector tools, including microgrippers, an electrical gripper, an ultrasonic tool, dispensers, probers, and laser cutting/curing tools are designed and employed to assist the subsystems to complete the demonstrators. Also, there are two optical tables, 3m x 1.2m and 1.8m x 1.5m, as stable and precise platforms to place and fix most stations on themself. On the longer optical table, a long linear motorized stage was fixed on the middle of the surface as one degree of freedom of the 6-DOF positioner. The positioner can be transferred on the long linear stage. Referring to the middle line of the long linear stage, the aerosol inkjet printing station, 3D printing station, PicoPulse deposition station, IPL station, and microassembly station are aligned and placed on the optical table in sequence as shown in Figure 4.1. Otherwise, Figure 4.2 shows the tool change station, PNP station, and other necessary components or devices were located on the other optical table.

Figure 4.3 depicts the controller rack that was installed with all the controllers for the hardware, such as two DENSO industrial robotic arm controllers RC8A, two high-precise Newport stages controllers XPS-Q8, an IAI long linear stage controller, a NI PXI-1086e chassis, several digital multimeters, and a UPS for power storage and backup.

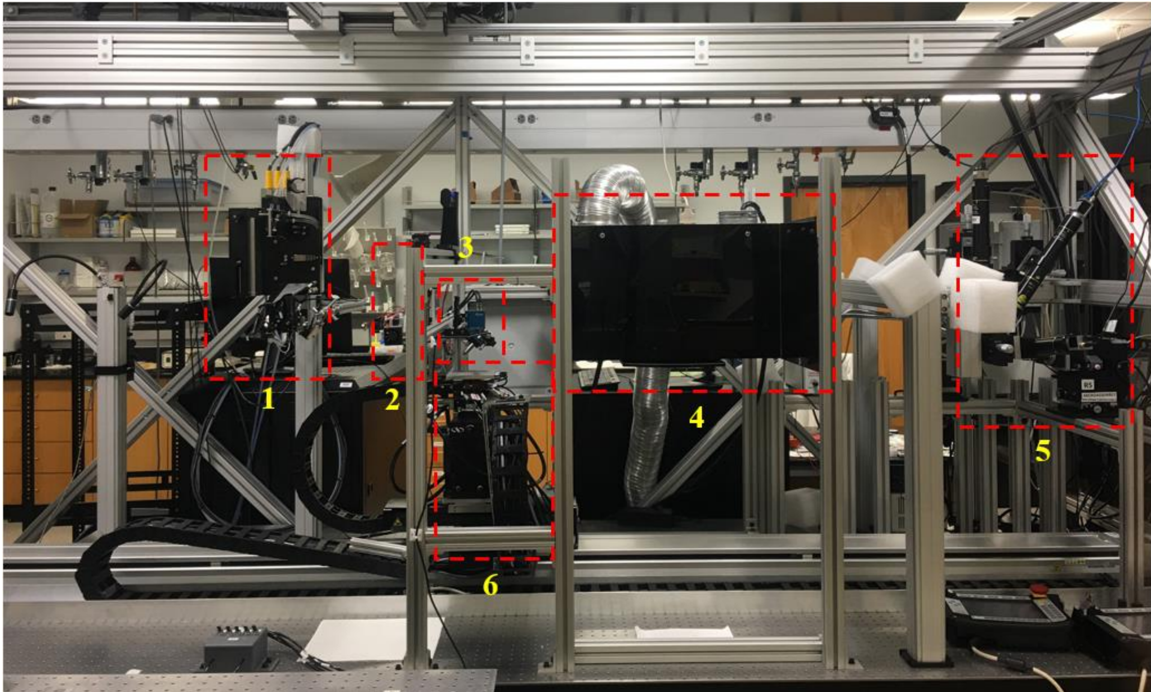

Figure 4. 1 OPTOMEC Aerosol Inkjet printer; 2. Stationary 3D printer; 3. PicoPulse deposition station; 4. IPL sintering station; 5. Microassembly station; 6 Custom 6-DOF positioner

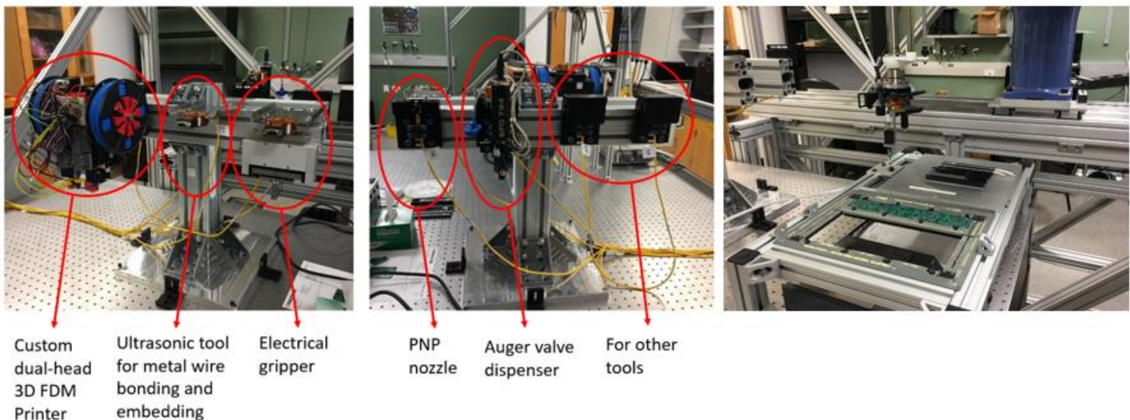

Figure 4. 2 Tool change station and PNP station

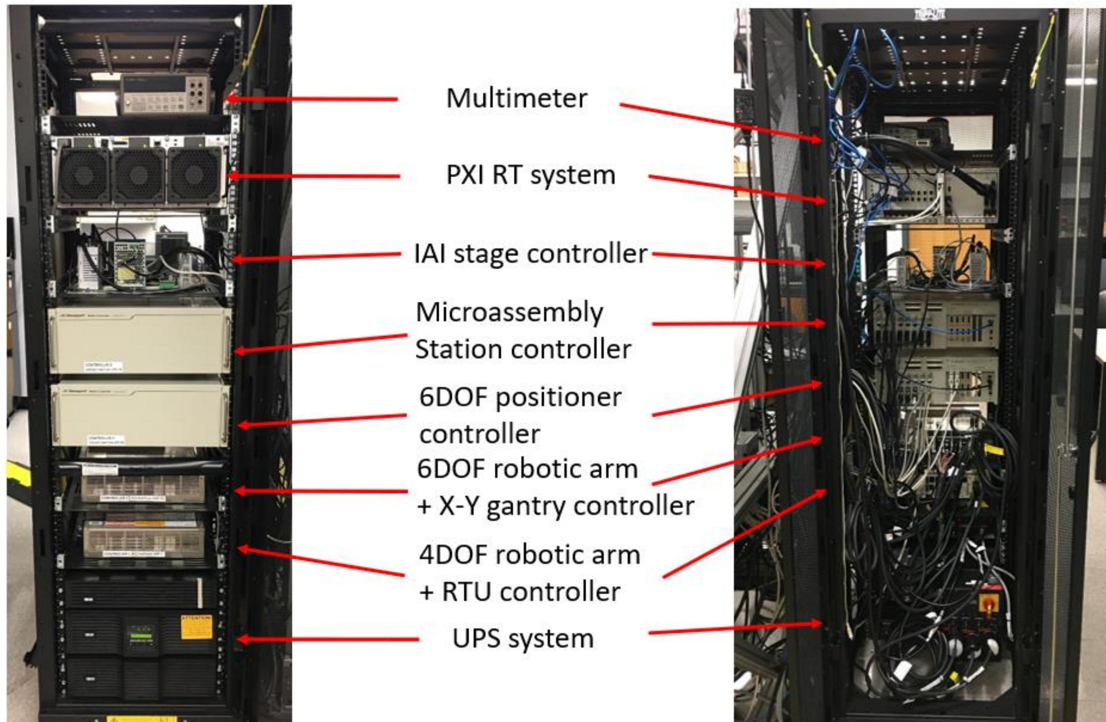

Figure 4. 3 NeXus controller rack

4.2 Precision Evaluation of NeXus

Normally, it is necessary to evaluate the custom robotic manipulators, especially, after the hardware setup. Even though the robotic arms or stages have their manufactural specifications which list all required parameters, such as repeatability, accuracy, payload, minimum increment, and so on, they are highly possible varied and affected by external modifications, like adding external joints to robotic arms or assembly multiple stages together to build multi-degree of freedom positioner. Therefore, it is significant to evaluate custom robotic manipulators to obtain new repeatability and accuracy values for further applications to manufacturing high-precision and yield products. In the NeXus, there are three custom designs for two industrial robotic arms and one custom positioner.

4.2.1 Evaluation of 6-DOF robotic arm with X-Y gantry

According to the NeXus hardware design, the DENSO VS6577B 6-DOF robotic arm was ceiling mounted on a large X-Y gantry and the gantry was fixed on a custom frame in Fig. 4.5. The custom frame was designed to support the X-Y gantry with a ceiling-mounted 6-DOF robotic arm. The stiffness and stability of the frame will consequently influence the motion performance of the robotic arm, which is especially critical for high-precision assembly applications.

The entire frame assembly, which can be viewed as a multi-member mechanical structure, exhibits various natural frequencies with corresponding modal shapes (eigenvalues). Due to the complexity of the structure, we used a Finite Element Analysis (FEA) simulation software COMSOL® to estimate the modal frequencies and mode shapes as well as deformation under a static load. The amplitude of each vibrational mode depends on the external moving objects attached to the frame, such as the gantry's body and the robotic arm.

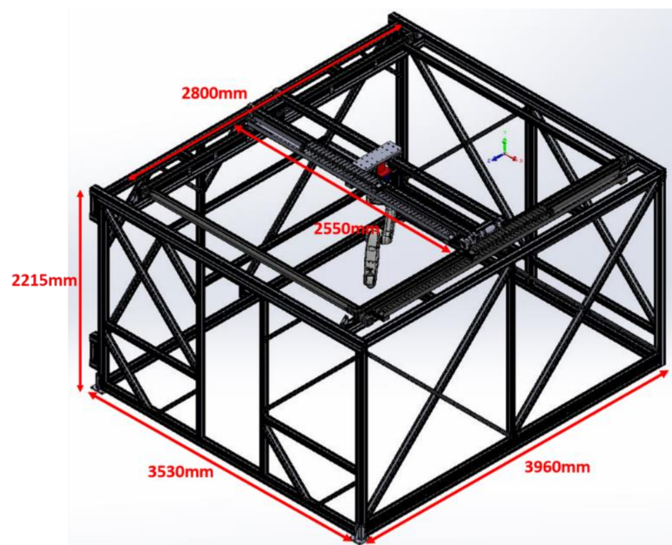

Figure 4. 4 The isometric view of the custom frame with mounted X-Y gantry and 6-DOF robotic arm

In Fig 4.6, due to the extremely large vibration of the initial design of the frame during the gantry motion, the custom frame must be improved the structures to strengthen the stiffness and stability. Several versions of frame modification have been proposed and simulated in Fig. 4.7.

For this analysis, the accelerated motions of the robot and the gantry were incorporated to calculate the effective forces acting on the frame, which were also used as inputs to the simulation software. The load sign can vary as the robot and gantry move in various directions. In terms of structural optimization, starting with the initial design, we applied several progressive modifications to the frame to improve its stability and mitigate vibrational amplitude during robot translation. The process of the initial and succeeding modified designs can be briefly described as follows, shown in Figures 4.6 and 4.7: in "initial design", the frame was fixed on the ground on its four corners with no additional buttress and interior beams, which suffered from shaking and observable deformation. The "2nd version" with lower beams anchored to the ground at 8 points, showed diminished vibrations on the base beams but not on the entire frame. The "3rd version" with small diagonal beams attached at each corner, showed a significant reduction in frame vibrations in all directions. The "4th version" with reinforced pillar did not serve to be a practical solution spatially, although showed an admissible response. Lastly, in the "final version" longer diagonal beams were used which led to further vibrational mitigations and structural deformation. Thus, in all cases, the revised designs resulted in improvement both in static and dynamic responses (increase eigenfrequencies and reduced maximum deformation), as depicted in Figure 4.7 and summarized in Table 4.2. Note that only the 1st mode shape and the maximum deformation for the worst-case scenario have been shown and listed in

progressive design versions. Compared with the initial design, the final version of the frame features a significant reduction in the maximum deformation (from 3.5mm to 0.8mm).

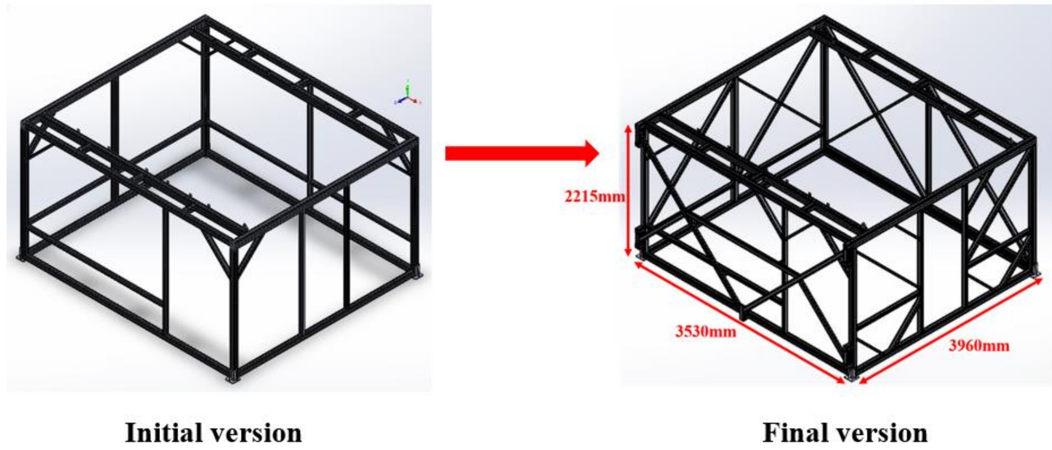

Figure 4. 5 Initial version and final version of the custom frame

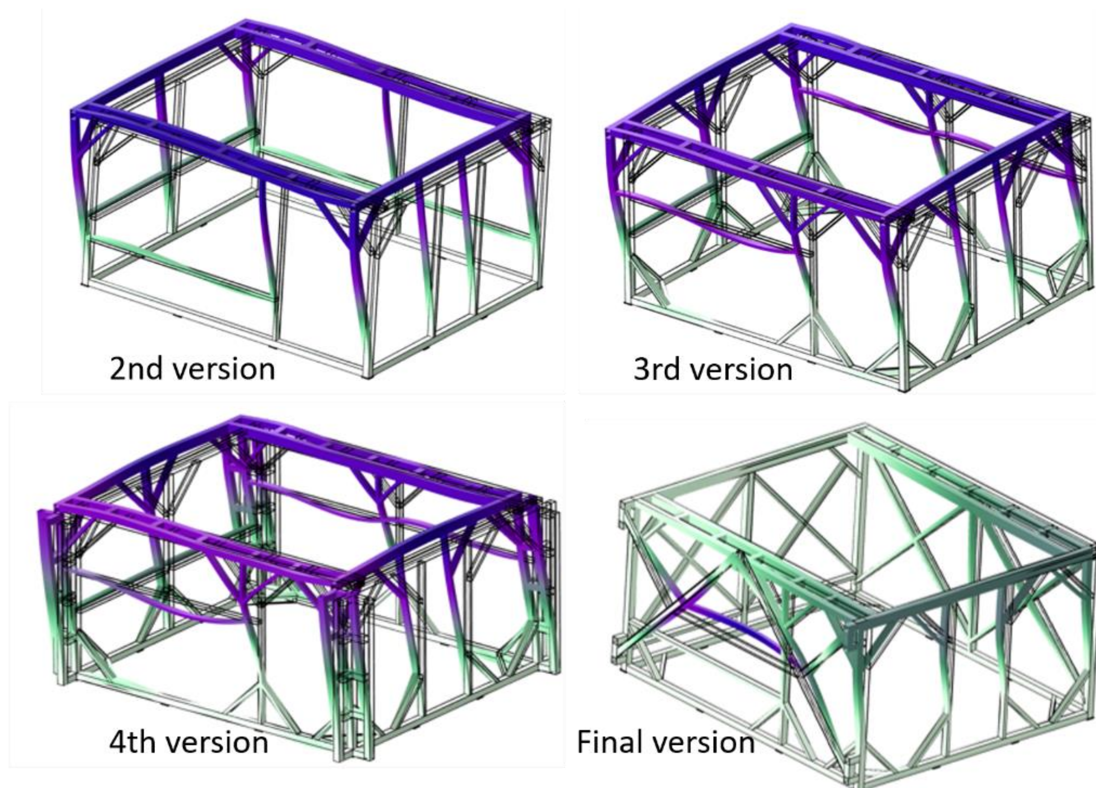

Figure 4. 6 Different versions of the frame with the improvement of structures. (Figure acknowledgment: Alireza Tofangchi)

Table 4. 1 Eigenfrequency and maximum displacement of different versions of frame design

Version of frame design	EF_1 (Hz)	EF_2 (Hz)	EF_3 (Hz)	Max δ (mm)
Initial version	11.1	12.6	14.8	3.5
2nd version	12.7	13.6	15.8	3.0
3rd version	18.3	20.6	22.2	1.2
4th version	23.4	25.4	27.4	0.9
Final version	19.9	23.8	32.6	0.8

δ: displacement in mm

The values of EF1, EF2, and EF3 are the first three eigenfrequencies estimated by FEA corresponding to the natural modes for the "same" loading cases on the frame. Practically, for design purposes, the lowest value of EF for each frame configuration is a matter of interest to avoid severe vibration in the structure. As is evident from Table 4.2, through each step of progressive modifications of the frame by adding and rearranging the beams, the eigenfrequency also varies. Of particular interest, the lowest eigenfrequency in each design increases from the initial version through the final version by a factor of 2 (1st column in Table 4.2), which is desirable.

After completing the assembly of the final version of the frame and mounting the gantry and robotic arm onto the frame, prior to the study of the precision metrics, it is necessary to evaluate the stability of the (frame + gantry + robot) system in a static mode when the gantry and the robotic arm are at rest. The evaluation included measurements of the robotic arm vibrations (noise level) and determination of the natural frequency of the gantry and robotic arm in a static mode. These measurements were conducted with the help of two Keyence® LK-G5000 (Keyence Corporation, IL, USA) laser displacement sensors as shown in Figure 4.8. Two sensors were set up to measure the variations of the amplitudes

of the natural vibrations along the X-axis and Y-axis. The sampling frequency of the sensor was configurated at 50KHz to collect 219 = 524288 points to determine the natural frequencies of the robotic arm system. Otherwise, the measurements were given in two modes: the robotic arm motor on (brake off) and the motor off (brake on). In these ways, it can indicate the influence of the motor status on the natural frequency of the robotic arm.

Figure 4. 7 Two laser displacement sensors measure the natural frequency of the robotic arm

After measuring the natural frequency of the robotic arm in the static mode, we evaluated the robotic arm positioning performance. The 6-DOF industrial robotic arm used in the NeXus has the following specifications based on its manual: maximum payload capacity of 7kg, maximum reach of 850mm, and repeatability of +/- 30µm. However, our custom robotic system containing the X-Y gantry and robot arm has a combined 8 degrees of freedom, and its precision needed to be evaluated with 8-DOF movements. To evaluate the robotic arm, an end-effector, including an ATI Gamma force/torque sensor (ATI Industrial Automation, Inc., NC, USA), an ATI QC-11 tool changer couple, and a HIWIN

XEG-32 electrical gripper (HIWIN Corporation, IL, USA) mounted at the end of the robotic arm as shown in Figure 4.9. The gripper held a 3D cube, onto which we mounted a 1cm x 1cm Silicon die with micron-scale features to serve as the target for visual measurements. To evaluate the pose accuracy and repeatability of the robotic arm, three different measurement sensors are employed: An integrated microscope camera (a combination of Edmund® EO-3112C camera, 7X zoom module motorized lens, and 2.0X lower lens) was calibrated at 70% magnification of the maximum zoom, which results in a resolution of 0.556μm/pixel to monitoring the target in a proper view; two Keyence® LK-G5000 laser displacement sensors with 0.0001mm resolution; and a Mitutoyo 534-390 Digimatic® indicator with 0.001mm resolution.

The first method to evaluate the pose accuracy and repeatability is using the microscope camera. Because the camera only has one degree of freedom, it only acquires 2D information from the image. To measure spatial variables, the microscope camera was set up in horizontal and vertical orientations (shown in Figure 4.9) to collect X-Y-Z axes data for every single point.

Three modes were proposed to measure pose accuracy (Ap) and pose repeatability (Rp). The first mode was that the gantry was stationary and only the robotic arm took the motions. The second mode was that the robotic arm was keeping a constant pose, but the gantry moved in X and Y directions. The last mode was a combined motion with the gantry and robotic arm.

Figure 4. 8 Hardware setup for evaluation of robotic arm by the microscope camera

In each mode, the robotic arm moved to the same point with the same pose. The commanded point should be in the field of view (FOV) of the camera, and the camera

would recognize the same micro-size feature as the target (shown in Figure 4.10) when the robotic arm moved to the point. Meanwhile, the center of the target pixel coordinate value was acquired and recorded by the LabVIEW® program with the vision assistant function. With the calibrated resolution of the microscope camera, the actual values of points the robotic arm reaches can be measured and calculated for Ap and Rp.

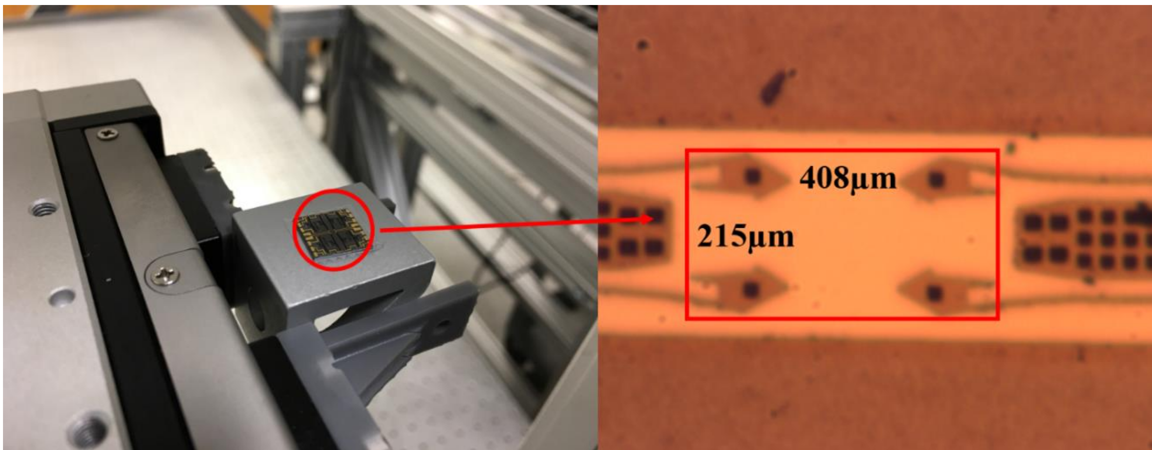

Figure 4. 9 Micron-size feature for visual measurement

For the first mode, there were 3 paths to evaluate the robotic arm performance – refer to Figure 4.11. The P0 was the target point, which was in the FOV of the camera, P1, P2, P3, and P4 were outside the FOV. The robotic arm performed repeatable motion between respective points.

1) 1st path: repeat linear motion between P0 and P1---X direction.
2) 2nd path: repeat linear motion between P0 and P3---Y direction
3) 3rd path: repeat motion along the diagonal section between P0 and P4

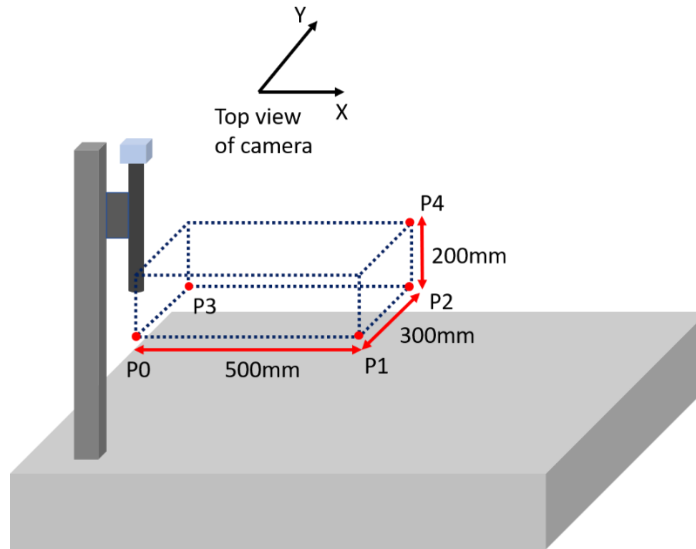

Figure 4. 10 Point location in the first mode

In the second mode, we considered motion only of the gantry along X and Y directions where the robotic arm was kept at rest in the same pose. Figure 4.12 shows the points that the target reached. P0' still represents the point in the FOV of the camera P1', P2', and P3' pointed outside the FOV of the camera during the gantry motion. The repeatable motion of the robotic arms was realized along the three paths.

1) 1st path: repeat the motion from P0' to P1'---X' direction.
2) 2nd path: repeat the motion from P0' to P3'---Y' direction.

In the third mode, we have considered the combined motion of the gantry and robotic arm together. The sequence of the repeatable motion is described below (Figures 4.11 and 4.12):

1) The robotic arm moved from P0 to P4 along a diagonal path.
2) Then, the gantry (with the robot) moved along X-axis from P0' to P1'.
3) Next, the gantry moved along Y-axis for the same distance between P1' and P2'.

4) After the gantry moved back following section |P1'P2'| and |P0'P1'| to the gantry's initial point at P0'.

5) Finally, the target is moved from the P4 position to the initial point P0.

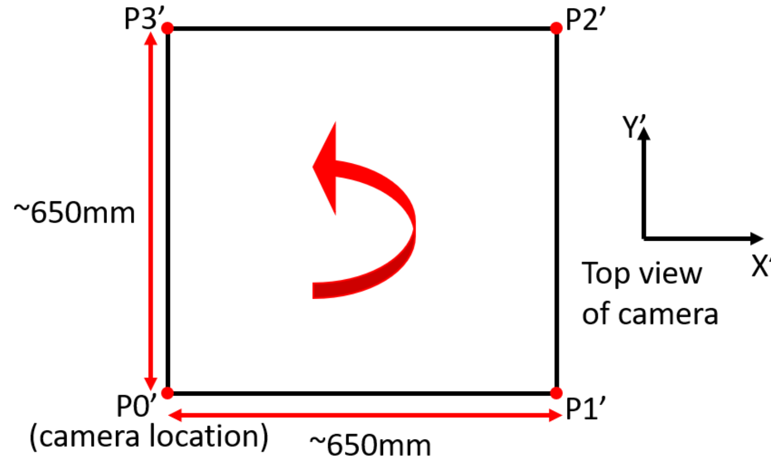

Figure 4. 11 Point location in the second mode

Besides the microscope camera method, we have employed another measurement method by using two high-resolution laser displacement sensors. Figure 4.13 shows different arrangements of two Keyence® laser displacement sensors for measurement in X, Y, and Z directions. Keyence® instruments were used to evaluate robotic arm performance for three different modes as the same modes described in the case of the camera. The experimental results of this evaluation will be discussed in Section 4.

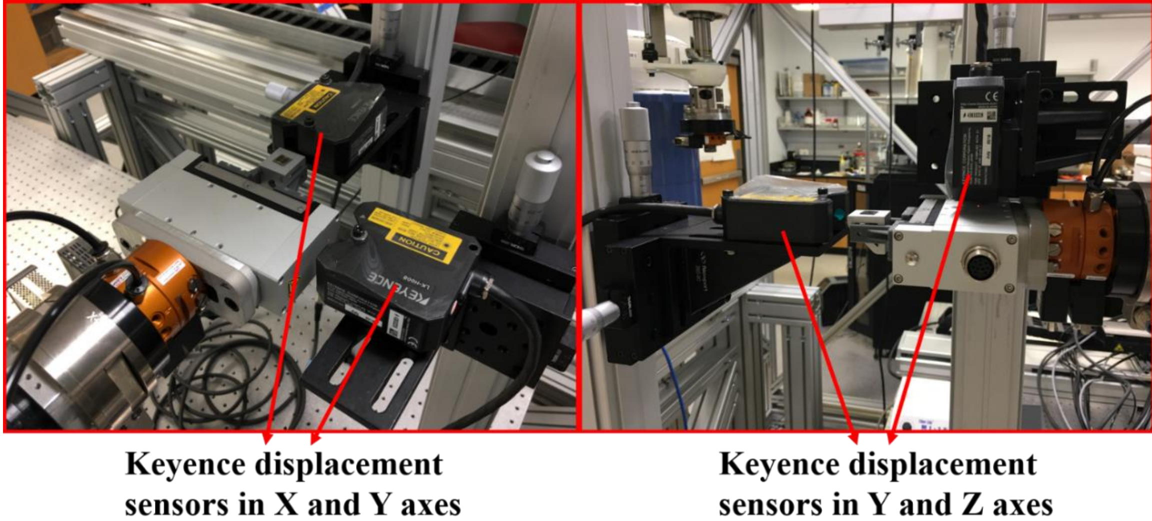

Figure 4. 12 Two laser displacement sensors were used to measure the pose performance

In the third evaluation method, we utilized a Digimatic® indicator to evaluate the robotic arm pose performance. Due to the measurement limit of the Digimatic® indicator, it only indicated the data by touching the object, which resulted in the Digimatic® indicator only could measure one direction of data of the robotic arm motion at once. Therefore, only one pose of the robotic arm was evaluated in the X, Y, and Z directions (shown in Figure 4.14).

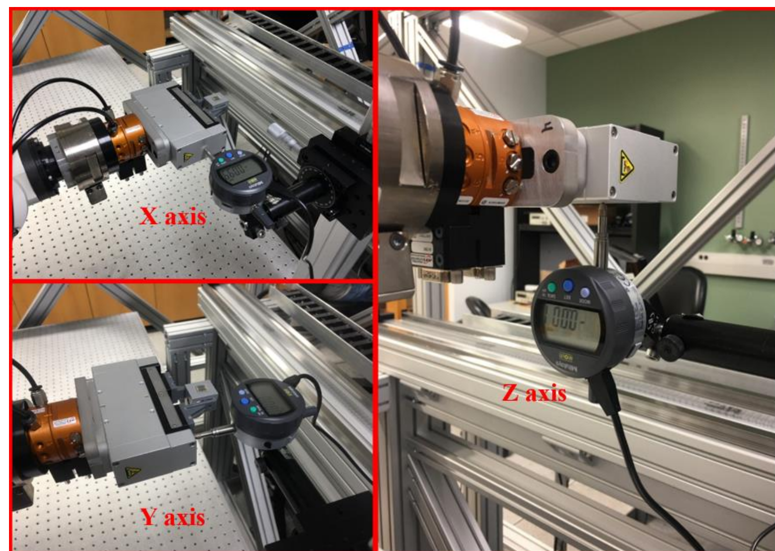

Figure 4. 13 A Digimatic® indicator used to measure the pose performance

First, our progressive design approach for the custom frame has significantly improved both static and dynamic responses of the structure, starting from the initial design towards the final version. In Table 2, it is evident to see three eigenfrequencies begin to ramp up as a result of increased structural stiffness particularly after adding more beams at specific positions. Otherwise, the maximum deformation of the frame in each version has been successively decreased, especially in the final version, where the maximum deformation dropped from 3.5mm (in the initial version) to 0.8mm. Besides, in some modal shapes, the deformation region is shifted from the upper beams (in other version designs) into the lateral beams in the final version design which can be viewed as an additional geometrical advantage.

4.2.2 Vibration performance of the frame

Prior to evaluating the pose performance of the robot, we investigated the spectral response of the positioning data collected in a static mode. The natural frequencies of vibration were estimated using the Fast Fourier Transform (FFT) algorithm dealing with the data collected by two Keyence laser displacement sensors. High peaks of frequency are shown in Figure 4.15 and the values are listed in Table 4.3. In both cases, no matter whether the robot's motor was on or off (brake off or on), the measured natural frequencies were very close for the X-axis and Y-axis, which means that the status of the motor is not a significant factor to the natural frequency of the robotic arm in the static mode. Due to direct current offset influence, the frequency of 0.09537 Hz can be neglected in Figure 4.13. Moreover, the estimated simulation of three eigenfrequencies of the final version of the frame's design (Table 4.2) is not matching any robot's structure's natural frequencies determined experimentally (Figure 4.13). It may speculate that this frequency mismatch

suggests that only the robot's motion would not induce the resonance. However, further study is needed to investigate whether the gantry motion can generate resonance in the whole frame + gantry + robotic arm structure.

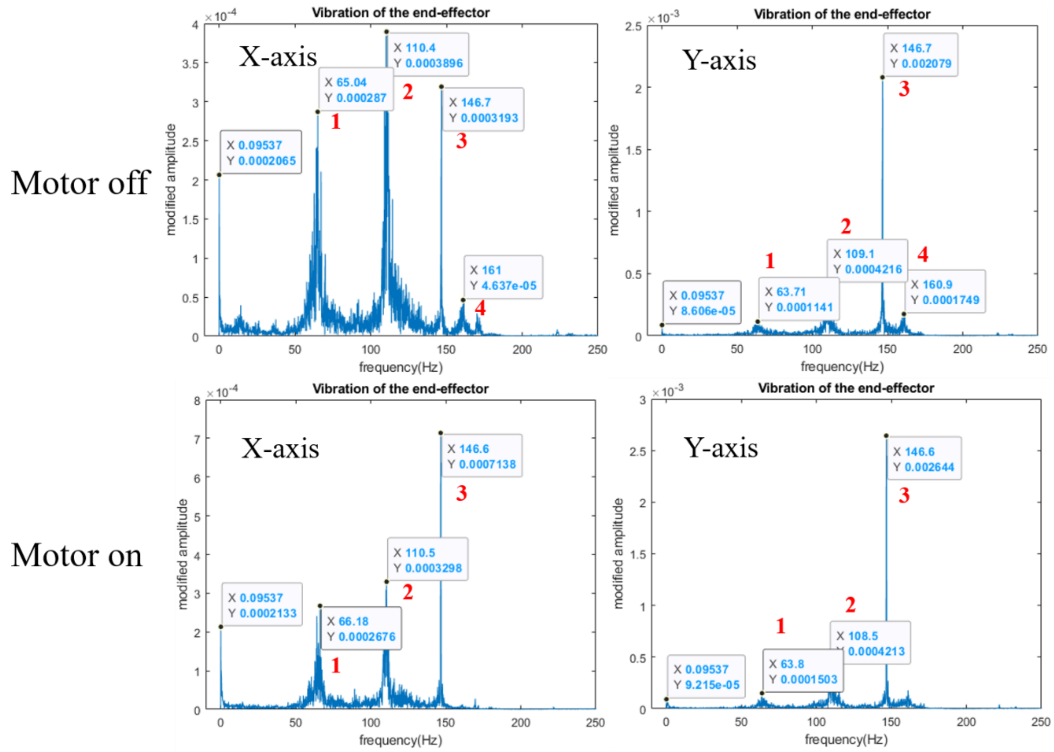

Figure 4. 14 Natural frequencies of the robotic arm at motor on and off

Table 4. 2 Natural frequencies (Hz) of the robotic arm in the motor on and off

Number	Motor off		Motor on	
	X-axis	Y-axis	X-axis	Y-axis
1	65.04	63.71	66.18	63.8
2	110.4	109.1	110.5	108.5
3	146.7	146.7	146.6	146.6
4	161	160.9	-	-

4.2.3 Precision metrics of the robotic arm and gantry system

After the stiffness and vibration of the frame were improved, the robotic arm was evaluated following the ISO9283:1998 standard. Two main robot performance criteria needed to be evaluated, including the robot's pose accuracy and pose repeatability. Pose accuracy represents how close the robot reaches the desired position in its workspace, and pose repeatability represents how close to the same location the robot returns repeatedly after N repeat cycles. Pose accuracy and pose repeatability were used in the same test conditions.

In the experiments, each path in the three different modes was repeated N=30 times, and we collected 30 data points along with the cartesian X-axis and Y-axis, and Z-axis respectively. To estimate the accuracy and the repeatability of the robot, we used the following definitions:

$$Ap = \sqrt{(\overline{X} - X_c)^2 + (\overline{Y} - Y_c)^2 + (\overline{Z} - Z_c)^2} \tag{4.1}$$

$$\overline{X} = \frac{1}{N}\sum_{i=1}^{N} X_{ai} \tag{4.2}$$

$$\overline{Y} = \frac{1}{N}\sum_{i=1}^{N} Y_{ai} \tag{4.3}$$

$$\overline{Z} = \frac{1}{N}\sum_{i=1}^{N} Z_{ai} \tag{4.4}$$

where X_c, Y_c, and Z_c are the commanded cartesian robot positions, X_{ai}, Y_{ai}, and Z_{ai} are the attained positions, and N is the number of motion cycles performed. $\overline{X}$, $\overline{Y}$, and $\overline{Z}$ are the mean of attained positions. Furthermore, the pose repeatability can be calculated as:

$$Rp = \bar{l} + 3S_l \tag{4.5}$$

$$l_i = \sqrt{\left(X_{ai} - \overline{X}\right)^2 + (Y_{ai} - \overline{Y})^2 + (Z_{ai} - \overline{Z})^2} \tag{4.6}$$

$$\overline{l} = \frac{1}{N} \sum_{i=1}^{N} l_i \tag{4.7}$$

$$S_l = \sqrt{\sum_{i=1}^{N} (l_i - \overline{l})^2 \Big/ N - 1} \tag{4.8}$$

where l_i is the deviation between i_{th} attained positions and the mean of attained positions. S_l is the standard deviation of l_i.

There are three different modes proposed to measure the pose accuracy and repeatability of the robotic arm: the motion of the robot only, the motion of the gantry only, and the motion combination of the gantry and robot. Due to the limitation of pose measurement of the gantry, only X and Y axes' motion can be measured. While the 6-DOF robotic arm can present motion in spatial space. Otherwise, there are three different types of sensors employed to measure the position values of the end-effector on the robotic arm: a microscope camera, two Keyence laser displacement sensors, and a Digimatic® indicator.

Firstly, a microscope camera was employed. Because the camera only has one DOF measurement, the microscope camera was set up in horizontal and vertical orientations to estimate the robot precision in the X, Y, and Z axes. The pose accuracy and repeatability calculated results were listed in Table 4.4.

In the first mode, the calculated pose accuracy and repeatability of the robot along with the 1st, 2nd, and 3rd paths are very similar. The probable reason for those results is that for the 1st, 2nd, and 3rd path robotic arm moves along a single and shorter section without changing

the direction of the motion (only orientation in case of the repeatable motion). Nevertheless, the calculated experimental repeatability is within the range of the factory value from the manufacturer +/- 30μm.

In the second mode, we analyzed only the gantry motion along with the X and Y directions. The main factors affecting precision metrics, in this case, are servo motor load, motor gearbox, gantry structure features, and payload. Different precision metrics results for the paths in the second mode are most likely caused by the structural features of the X-Y gantry and how it affects its motion. We can consider several reasons for different values of accuracy and repeatability. In Figure 4.11, in Y's direction (2nd path), the gantry base components were mounted on the top of the frame and rigidly supported by the structure of the frame. Whereas in X's direction (1st path), there is not much support for motion components, just relying on the stiffness of component material. That may result in different metrics between the 1st and 2nd paths. Another factor could be the payload. Analyzing the gantry structure in Y's direction (2nd path) servo motor with gearbox will have a smaller load since it has to move only the robotic arm with gantry adapter/fixture along a 2.5m section. Whereas in the X' direction (1st path), the same servo motor with the gearbox has to move a much larger (heavier) payload. The whole 2.5m section with several long aluminum beams and the robotic arm. A larger payload usually results in lower accuracy and worse repeatability. Another possible contributing factor related to the gantry's structure is the difference in motion realization for both paths. In the case of the 2nd path (Y' direction) motion is simpler where the robotic arm with adapter is transported along one linear track. For the 1st path (along X' direction) we consider displacement of a

2.5m long structure with a more complex servo motor-transmission system which might cause non-synchronous motion of both ends at the microscale.

For the 3rd path, the robot moved in a cycle path stopping at four corners which resulted in the worst result for repeatability. Here, the scenario is similar to the case of the second mode's 1st path. As expected, repeatability is higher due to combined motion along different sections in different directions and larger travel distances. Although interestingly accuracy for the 3rd path is improved compared with the 1st and 2nd paths, it could be caused by error compensation when the robot returns to the starting point after being displaced along the square-shaped trajectory (Figure 4.12).

In the third mode, the combined motion of the gantry and robotic arm should be considered with various factors. 37.4µm is sort of a reasonable measurement even if it is higher than 30µm due to the gantry motion factors probably as domain factors.

Table 4. 3 Pose accuracy and repeatability of the robotic arm using a microscope camera

	Accuracy (µm)	**Repeatability (µm)**
The first mode (robot only)		
1st path	5.3	8.7
2nd path	5.7	6.2
3rd path	5.7	6.2
The second mode (gantry only)		
1st path	40.8	39.3
2nd path	24.7	26.5
3rd path	19.7	39.5
The third mode (gantry + robot)		
Combination	9.6	37.4

Also, we used two Keyence laser displacement sensors to evaluate the pose performance of the robotic arm. The motion modes are like the ones we discussed for

microscope camera measurement. The pose accuracy and repeatability experimental results are listed in Table 4.5. The laser displacement sensor is much more precise than the microscope camera to measure objects because of the different measuring functions they have. By using the camera to measure the target position, it must utilize an image processing function to recognize the template of the target. Due to the natural vibration of the whole system, the images captured by the camera were not static but fuzzy, which results in the target position losing precision. Compared with camera measurement, the laser displacement sensor is more reliable and stable based on high sampling frequency (set 50kHz), but the LabVIEW® program to collect data after image processing of the camera just has around 7.5Hz sampling frequency. Therefore, the data collected by the laser displacement sensors are reasonable resulting in the high precision of measurement.

From Table 4.5, the accuracy and repeatability values are almost the same in the first mode. The reason has been discussed above. But in the second mode, there is a big difference in repeatability between the 1st path and 2nd path. The reasons are probably the same as the ones discussed above for the camera measurement. The accuracy and repeatability of motion in the Y direction are much better than in the X' direction. While the repeatability of combination motion is more than 30μm, 34.7μm also is a reasonable result after considering the repeatability of gantry and robot motion individually.

Table 4. 4 Pose accuracy and repeatability of the robotic arm using two laser displacement sensors

	Accuracy (µm)	**Repeatability (µm)**
The first mode (robot only)		
1st path	15.6	11.0
2nd path	15.0	11.0
3rd path	10.8	11.8
The second mode (gantry only)		
1st path	10.8	22.7
2nd path	8.3	9.8
Third mode (gantry + robot)		
Combination	15.6	34.7

Besides the above two methods, a Digimatic® indicator was used as another sensor to evaluate the pose accuracy and repeatability of the robotic arm. Due to its sensing principle, the Digimatic® indicator collected the data by being touched by the object. That limits the sensor to only measure one direction displacement. We only evaluated the pose accuracy and repeatability of the robot with gantry motion in the X and Y axes, and the robotic arm motion in the X, Y, and Z axes. The travel length of gantry motion on the X or Y axis is around 650mm while the travel length of robot motion is 500mm for X-axis, 300mm for Y-axis, and 200mm for Z-axis. There is only one direction parameter instead of three-direction parameters in the equations to calculate the pose accuracy and repeatability of single-axis motion. The calculated results are listed in Table 4.6.

Table 4. 5 Pose accuracy and repeatability of the robotic arm using a Digimatic® indicator

	Accuracy (µm)	**Repeatability (µm)**
The first mode (robot only)		
X-axis	**5.2**	**4.6**
Y-axis	**2.8**	**3.3**
Z-axis	**3.2**	**6.2**
The second mode (gantry only)		
X-axis	**22.3**	**36.2**
Y-axis	**4.0**	**9.1**

From Table 4.6, the repeatability in X-axis and Y-axis is almost close, but in Z-axis, the repeatability increases a little bit. That might be caused by the payload factor in Z-axis. When the robotic arm moved down to touch the indicator, Due to the inertial movement in Z-axis, it could result in the offset of displacement. Otherwise, for the gantry motion, the repeatability in the X-direction motion is much more than one in the Y-direction motion. Those results are similar to the other two sensors' experimental results. The reasons for this case should be the same.

According to the ISO standard, accuracy is a deviation between the commanded position and the measured (attained) position. Whereas repeatability is a measure of fluctuation between the measured actual positions after repeat visits to the same commanded position. Therefore, these two measures provide information about two distinct properties of the evaluated robotic system in the context of the planned tasks. There is a possible scenario where calculated accuracy can be better than repeatability.

In this case, attained positions are widely distributed due to the given experimental conditions resulting in the large value of repeatability – "bad" repeatability – in agreement with the definition. However, attained positions are evenly distributed (normal distribution) where the mean attained position is relatively close to the commanded position resulting in a low value of accuracy – "good" accuracy.

In our study we faced an interesting situation where the pose accuracy is fluctuating relative to the pose repeatability (Tables 4.4 – 4.6) – some values are less than repeatability, but some are more than that. This is due to several factors, such as different instruments used for the position measurements, different modes, and paths during the motion of the

robot/gantry system. Nevertheless, the behavior of our system reflects possible scenarios regarding the relation between accuracy and repeatability.

We would like also to pay attention to the arbitrary character of the ISO standard definition of accuracy which was discussed by other researchers. Specifically, the challenge is to clearly define the commanded position, which is usually associated with the robot's system of coordinates, compared to the attained position determined by the sensor, and defined in the sensor's system of coordinates.

Comparing all three types of sensors used in the experiments, we have determined that the Keyence® laser displacement sensor is more reliable and precise than the two other tools. One of the factors is the sampling rate of data acquisition. The acquisition frequency of the microscope camera drops to on 7.5Hz due to the image processing steps. For example, the LabVIEW vision assistant function was used to acquire the target coordinate information, such as pixel values at a specific location. By comparison, the Keyence® sensor sample rate can be set as high as 50KHz. Such low acquisition frequency of the camera might result in low precision measurement of pose accuracy and repeatability. On the other hand, the Digimatic® indicator allows measurement only in one direction at once, thus providing less information compared to the microscope camera and the Keyence® sensors. In summary, the Keyence® laser displacement sensors allow the most reliable evaluation of the robotic arm performance in a custom robotic system.

4.2.4 Evaluation of SCARA robot with RTU

From the experience of evaluation of the 6-DOF robotic arm with X-Y gantry and custom frame, only two Keyence laser displacement sensors were employed to evaluate

the SCARA robot with RTU because of the high precision of sensors. Also, there are some factors, such as speed, payload, and pose of the robotic arm, to influent the pose performance of the robotic arm. Thus, when evaluating the SCARA robot and RTU accuracy and repeatability, different speeds of motion were applied. For example, in auto mode, the output speeds of the robotic arm and RTU are determined by two different speeds, external and internal speeds. External speed can be modified in the teach pendant from 1% to 100% and the internal speed is set up in the program, such as LabVIEW. For the experiments, the external speed in the teach pendant was kept at 100%, and the only internal speed varied by 10% and 50%, which are acceptable and reasonable speeds for the NeXus system. It is not necessary to set up too fast the speed of robotic arm motion in the real manufacturing process. SCARA robot and RTU as well as their combination motions were evaluated using similar methods mentioned above. The accuracy and repeatability of SCARA and RTU are listed in Table 4.7. The repeatability of the SCARA robot is extremely different in various speed motions, but RTU seems to keep constant repeatability. The combination of SCARA and RTU has a closed value of repeatability in the different internal speeds of motion, which is around 6μm.

Table 4. 6 Accuracy and repeatability of SCARA and RTU

	Accuracy(μm)			Repeatability (μm)		
Internal speed	SCARA	RTU	Combination	SCARA	RTU	Combination
10%	2.6	13.1	3.9	5.5	22.4	5.4
50%	4.0	16.7	18.6	8.2	22.7	28.6

Note 1. External speed from teaching pendant is 100%; 2. In combination, keep the SCARA robot speed at 10%, only varying RTU's speed.

4.2.5 Evaluation of Custom 6-DOF positioner

The custom 6-DOF positioner (shown in Fig 4.16) contains a long linear stage X_L (IAI® ISPB-LXMX-200) and 5 high-precision motorized stages, including two linear stages X and Y (Newport® M-ILS300LM-S), a Z stage (Newport® GTS70VCC), a tilt stage (Newport® BGS80PP), and a rotation stage (Newport® URS50CPP). They were arranged and assembled from bottom to top in order of X_L-Y-X-Z-T-R. On the top of the rotation stage, an ATI QC-11 tool change coupler was used to mount the sample chuck. Some useful specifications are listed in Table 4.8. After assembling all the stages with relevant adapters and arranging all the cables, the 6-DOF positioner was evaluated using the vertical microscope camera in the microassembly system of the NeXus as shown in Figure 4.17. Using OPTOMEC Aerosol Inkjet printer to print a small cross as the template for the imaging process to record and calculate the repeatability of the 6-DOF positioner. Currently, only the repeatability of the IAI stage with the above stages has been evaluated and measured repeatability is 17.76μm refer to ISO9283. Other stages' repeatability will be evaluated in the future.

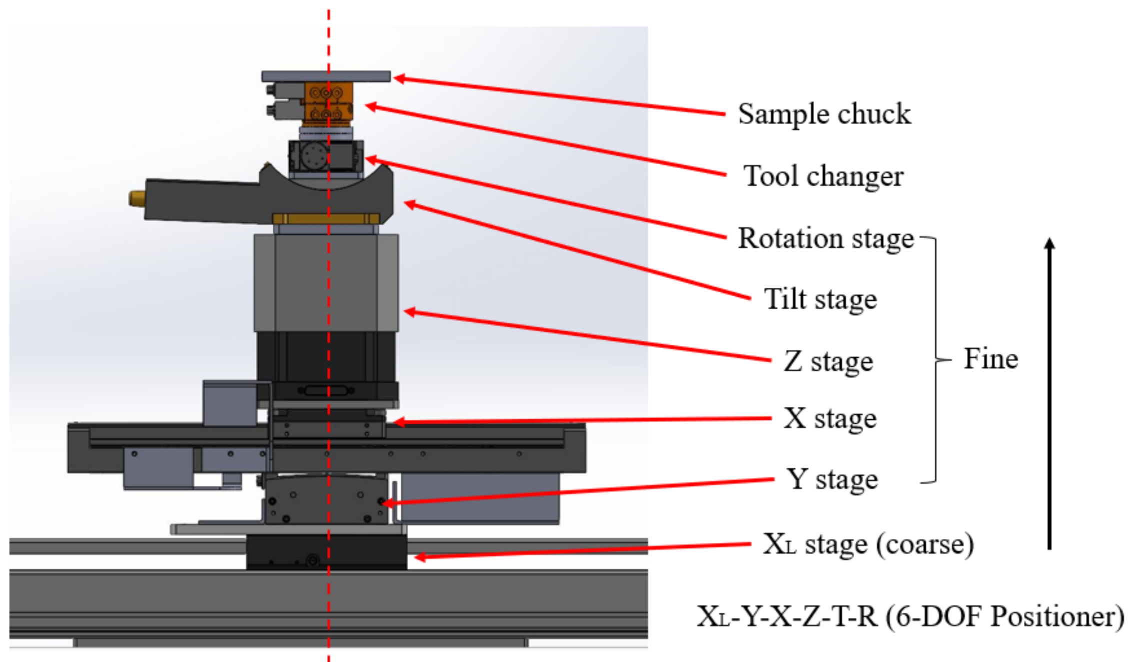

Figure 4. 15 The CAD model of the 6-DOF positioner, featuring a coarse X, fine XYZ translation, tilt, and rotation

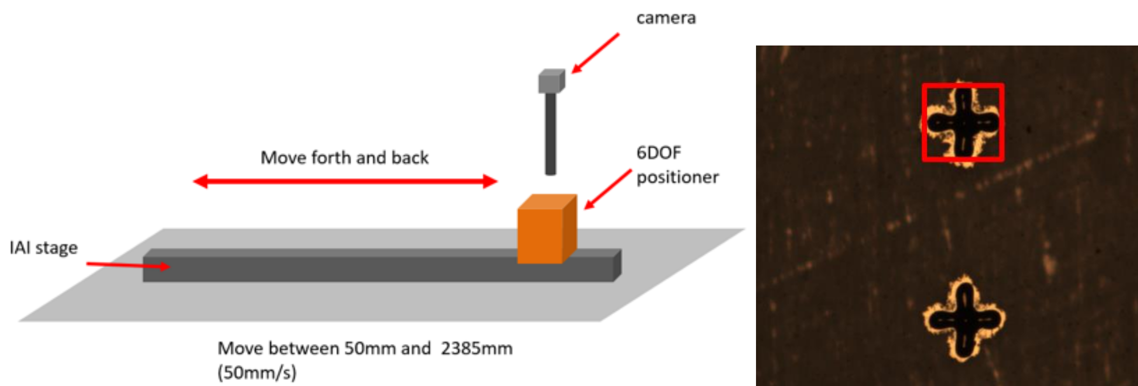

Figure 4. 16 Evaluation of 6-DOF positioner with a crossing template

Table 4. 7 Specifications of the custom 6-DOF positioner

	6-DOF Positioner					
	X_L	**Y**	**X**	**Z**	**Tilt**	**Rotation**
Travel (mm)	2500	300	300	70	90 deg	360 deg
Accuracy(µm)	-	2.5	2.5	1.75	30mdeg	25mdeg
Repeatability (µm)	18	5	5	0.5	2.5mdeg	1mdeg
Resolution (µm)	10	0.01	0.01	0.25	0.2mdeg	0.5mdeg
Weight (kg)	53.6	4.5	4.5	4.35	2.1	0.7
Payload (kg)	45	25	25	7	6	10

CHAPTER V DEMONSTRATOR OF NEXUS

5.1 Tactile Sensor Fabrication

5.1.1 Fabrication of Tactile Sensor in the Cleanroom

Figure 5.1 depicts the recent skin sensor fabrication process in the cleanroom, there are numbers of steps in the recipe and multiple specific instruments need to be trained to guarantee low repeatability using lift-off or metal etching techniques to remove unnecessary metal traces.

5.1.1.1 Design of Sensor

The star-shaped tactile sensors in our design have been simulated using COMSOL® Finite Element Analysis (FEA), as described in [62]. Here, we summarized the dimensional parameters of our sensor array used to refine the fabrication process. A photolithographic mask was generated as depicted in Figure 5.1. The mask has three sensor arrays, and each array has 16 individual tactile sensors in a 4x4 arrangement. The diameter of each sensor is 3.65mm and the 16 sensors are arrayed in a grid with each sensor separated by 7mm spacing. Figure 5.1 also depicts the dimensions of a single beam in a star-shaped structure. Electrical traces are 0.5mm apart and they are 1mm thick. Nine electrodes are interconnected from tactile sensors to both sides of the array. Eight electrodes are for signal lines, and one is for ground. The side electrodes will later be used for interconnection to the electronic circuit.

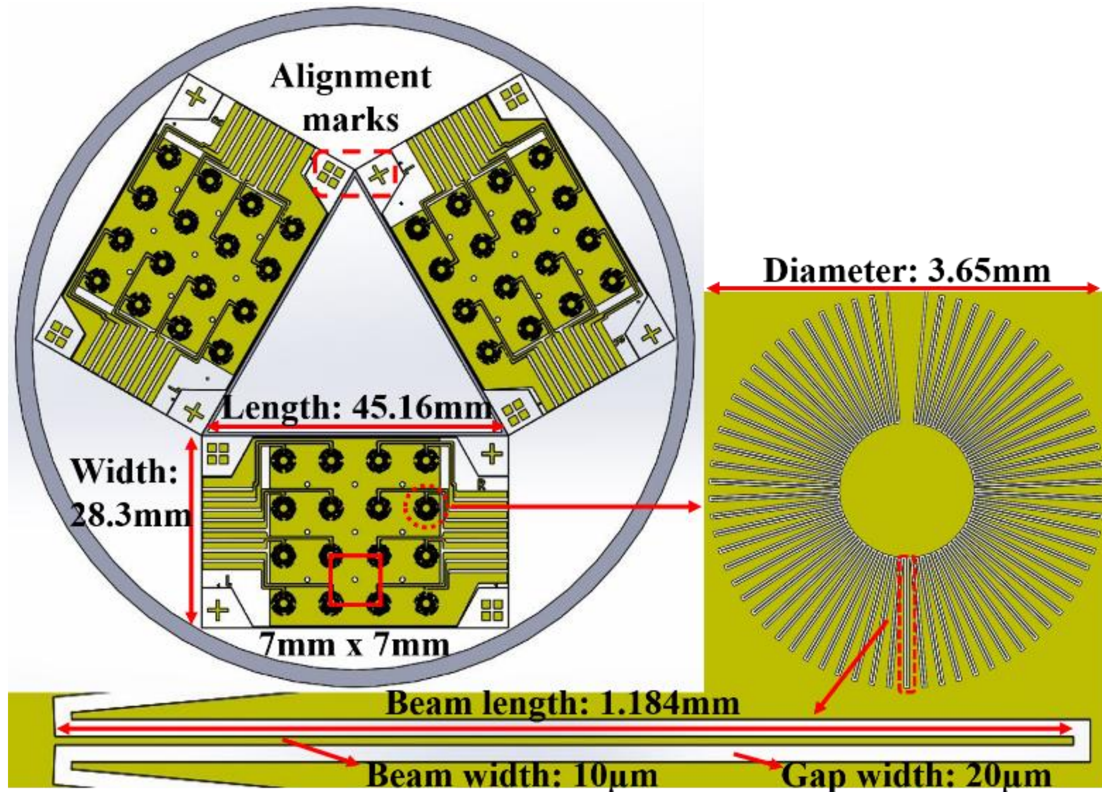

Figure 5. 1 Star-shaped sensor array mask design for 4-inch wafer and dimensions of a sensor array, single sensor, and single beam.

5.1.1.2 Fabrication Process

We adapt well-known cleanroom techniques to fabricate the pressure-sensitive robotic skin sensor with PEDOT: PSS organic piezoresistive material on Kapton® substrates. Figure 5.2 depicts the fabrication process leading to the patterning of sensor features on 50 µm thick Kapton® sheets. To improve the repeatability of PEDOT: PSS deposition and the performance of sensor arrays sensitivity, we developed a dry etching photolithographic method to create a uniform PEDOT: PSS layer on the star-shaped sensing structures.

To make a PEDOT: PSS-based solution with high viscosity and more stability, we used two chemical additives: Dimethyl sulfoxide (DMSO) and Polyvinylpyrrolidone

(PVP). They are mixed with 5wt% PEDOT: PSS in a ratio of 2g (PEDOT): 2g (DMSO): 0.77g (PVP), which is the quantity needed to fabricate one substrate. Before spinning the PEDOT: PSS mixture solution on the substrate, it should be sonicated for at least 60 seconds in order to evenly generate a uniform sensor layer.

The overall fabrication process is described in detail below:

Step 1: First, a clean 4” silicon wafer is prepared as a carrier and spun with MicroChem® SPR 220-3.0 photoresist.

Step 2: A Kapton® polyimide film is cut to an appropriate size, which is a little smaller than the 4” wafer size and cleaned by Acetone and Isopropyl alcohol (IPA), in that order. The film is aligned and loaded on a carrier 4-inch silicon wafer and placed on a hotplate at 115ºC for 60 seconds, where the Kapton® film is covered with a 6” by 6” square thicker Kapton® film and laminated by a brayer. The wafer along with the Kapton film is removed after heating for a short time. Take away the thicker Kapton® film and then the skin sensor Kapton® substrate adheres to the wafer.

Step 3: Two-layer photoresists composed of MicroChem LOR3A and SPR220-3.0 are spun onto the wafer respectively for patterning the electrodes. The wafer is soft baked at 115ºC for 120 seconds and cooled down before the next step.

Step 4: Select the desired electrode mask to do the first photolithography using a Karl SUSS® mask aligner with 16 seconds of UV light exposure.

Step 5: The wafer is then placed on the hotplate at 115ºC for 60 seconds’ post-bake. The photoresist is developed using MF319 developer. Then the sample is dried with an N_2 gun and cleaned using MARCH® Reactive Ion Etching (RIE) set at 50 watts power with a 20 SCCM flow rate of Oxygen for 45 seconds under 300 mTorr pressure.

Step 6: A sputtering deposition system, Kurt J. Lesker® PVD75, is used to sputter 300 nm of Gold on the patterned Kapton film. The coated Kapton® film and wafer are placed in a beaker with Acetone, then placed in a sonicated bath for approximately 20 minutes for liftoff. The Kapton® film detaches from the wafer and is rinsed several times with Acetone and IPA and dried with an N_2 gun.

Step 7: Each sensor's resistance is measured before continuing the fabrication process. Ideally, the measured conductance values of each sensor should be zero because they are open circuits. If any sensor has a non-zero conductance value, the Kapton® film will be liftoff again or cleaned by RIE. The reworked film with interdigitated structures should adhere to a new carrier wafer following step 2.

Step 8: A PEDOT: PSS-based solution is spun onto the Kapton® film, and the patterning windows over the interdigitated structures are covered with a semi-conductive material. Then the wafer is moved into a conventional oven to dry at 80ºC under a vacuum for 10 minutes.

Step 9: The wafer is cooled, then an SCS Labcoter® 2 (PDS 2010) Parylene deposition system is used to coat a thin layer on the Kapton® film with 2g type C Parylene particle. When the coating is done, the sensor surface is sprayed with N_2 to remove any dust.

Step 10: Repeat step 3 to spin two layers of MicroChem LOR3A and SPR220-3.0 photoresists on the Parylene film.

Step 11: Using a second mask, the sensor area is exposed to do a second photolithography step in the mask aligner for 16 seconds under UV light, and then repeat step 5.

Step 12: Using the PVD75, a 300nm thickness Titanium is sputtered on the top surface of each tactile sensor. Then repeat the liftoff process in step 6.

Step 13: Finally, the RIE machine is set at 200 watts power with a 20 SCCM flow rate of Oxygen to etch the surface of Kapton® film for several cycles (each cycle is 5 minutes etching and 1-minute cooling) until reaches the Kapton® substrate.

Because the etching rate of Titanium is considerably slower than that of Parylene and PEDOT: PSS mixture, the Titanium looks like a cap that can protect PEDOT: PSS remaining in the sensing areas, as shown in Figure 5.3. At this point, each sensor should have non-zero resistance values and these values are recorded for the pairing process prior to lamination, as described in the next section.

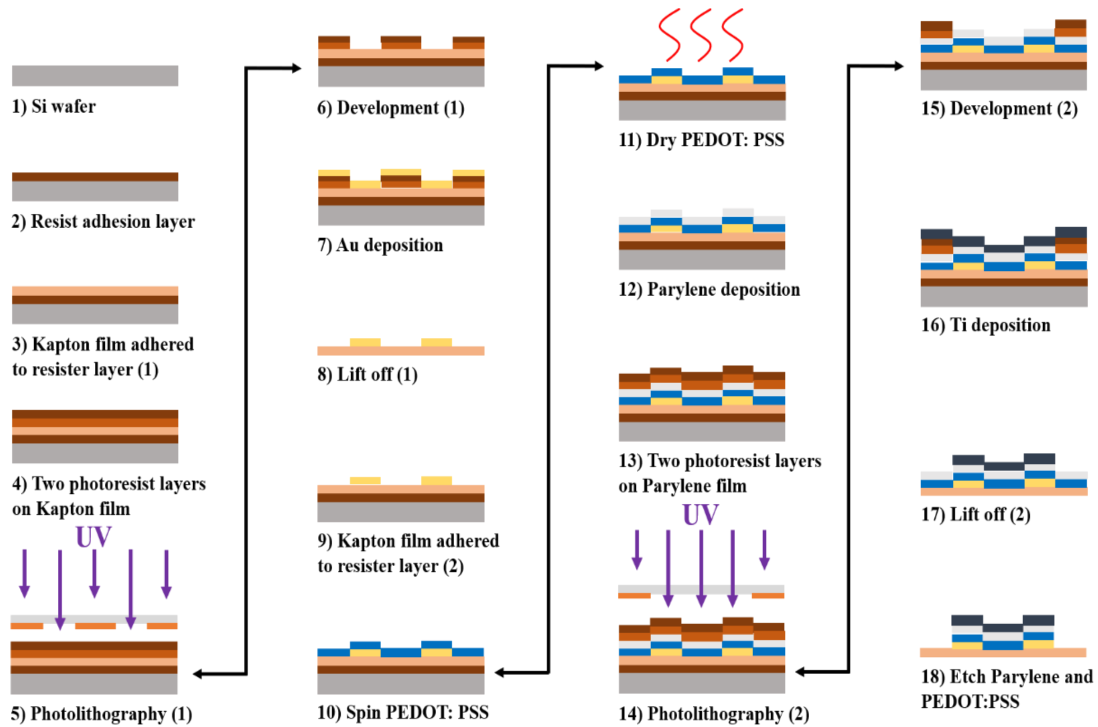

Figure 5. 2 Skin sensor fabrication process in the cleanroom.

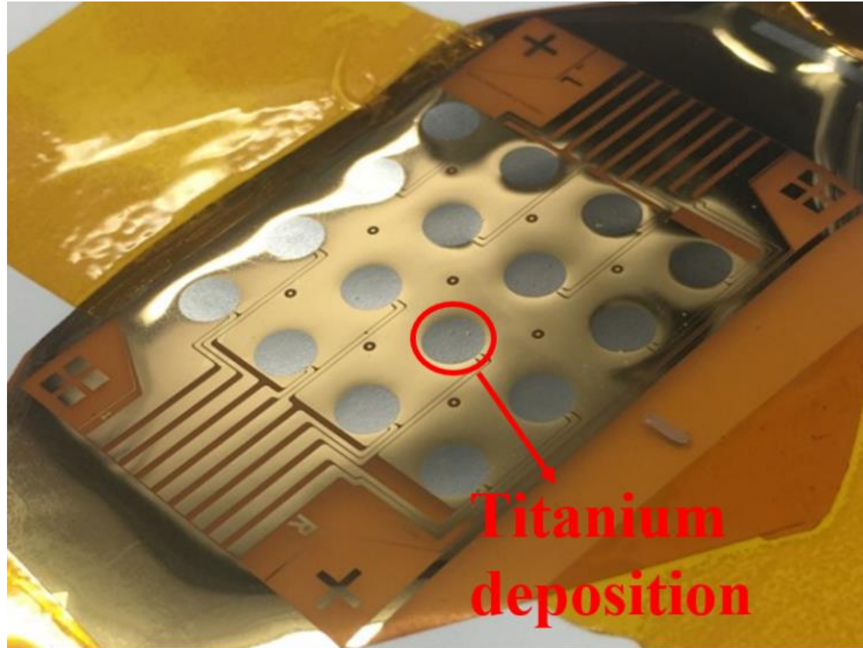

Figure 5. 3 The fabricated sensor array with a Ti protection layer.

5.1.1.3 Lamination Process

After the skin sensor array fabrication is completed, the arrays are prepared for lamination as a double-sided skin structure prior to testing. The purpose of double-sided sensors is to compensate for temperature drifts and double the sensitivity of the skin, as discussed in detail in our prior work.

The overall lamination process is described below:

Step 1: The Kapton® substrate, which was fabricated with star-shaped sensor array structures, is cut into three pieces, as shown in Figure 5.4. Then, the sensor films are placed in a suitable uncovered container and moved to a conventional oven at 85ºC under vacuum for 15 minutes.

Step 2: The samples are handled with care and placed on a flat surface with adhesive tape. Then the samples are evenly protected with a wider Kapton® tape. Both tapes are cut to size while the electrode areas are protected.

Step 3: Based on the measured resistance of tactile sensors, two sensor arrays, whose resistances' values are most closely matched, are selected to form a lamination pair. Then, pick up one of a pair of sensors whose back faces up and place it on the flat substrate. An additional thin Kapton® tape is used to create double layers on both sides of the electrode connectors. Finally, we use a razor blade to remove the extra tape from the sensor array outline. Because the connection space of a zero-insertion-force (ZIF) connector is wider than two sensor array substrates laminated together, the double layers of thin Kapton® tape are employed to increase the electrodes thickness of the double-side sensor array to match the ZIF connector space.

Step 4: Two sensor arrays of a pair were cleaned with Acetone and IPA, then aligned back-to-back following the alignment marks placed at the corners of the sensor array. We used a clip to clamp one side of the pair.

Step 5: The double-layer sensor array is placed on the flat substrate, put wiping paper in the middle of the pair, and separating them. Then we sprayed 3M® contact adhesive evenly in between the pairs.

Step 6: The wiping paper was removed, and the pair were closed together, then the clip was removed, another wiping paper was placed on the top of the laminated sensor arrays and the brayer was used to create a double-sided structure.

Step 7: Laminated double-layer sensor array is put between two flat substrates, placed a heavy metal block on the top, and moved them into the conventional oven at 75ºC under vacuum for 10 minutes to cure the adhesive.

Step 8: Finally, the laminated sensor array is moved out and trimmed the outline to make its edge flush with the bottom for inserting two ZIF connectors, which are now ready to interconnect with our conditioning electronic circuit.

Figure 5.4 depicts the lamination process, including pictures of the 8 steps outlined in this section.

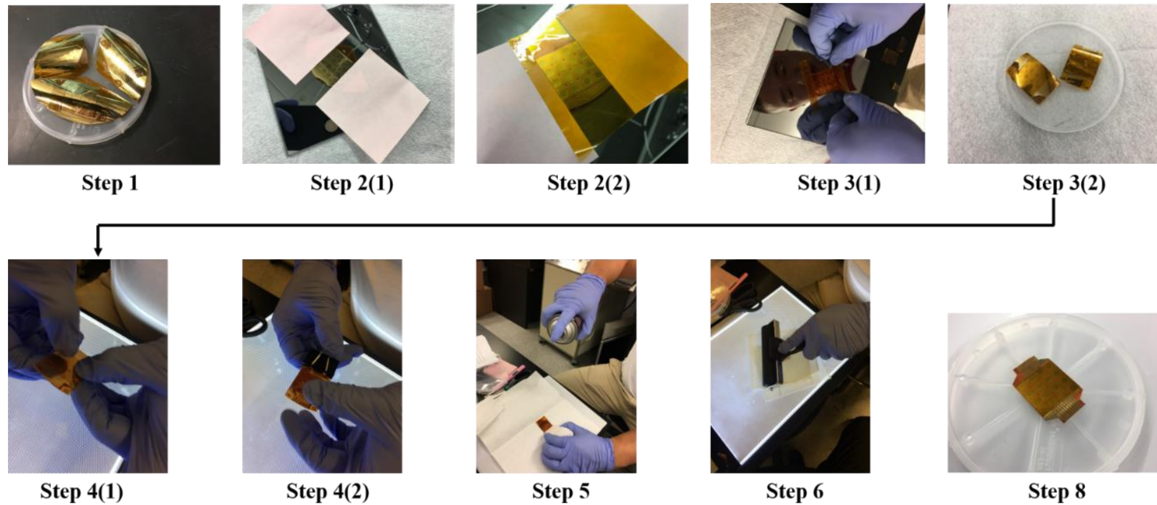

Figure 5. 4 Lamination process for the double-layer skin sensor array.

5.1.1.4 Experimental Setup

To measure the performance of the skin sensor array under various loading conditions, a custom-made indenter system was set up as shown in Figure 5.5. The testing system consists of three Newport® UTM150CC1HL motorized linear stages, which are assembled into an X-Y-Z platform. A load cell with a changeable indenter was mounted on the Z-axis to provide the load on the skin sensors, and a conditioning circuit was designed for receiving real-time strain data during load application. A MATLAB® graphical user interface was developed to collect data and visualize the strain gauge tactile response maps.

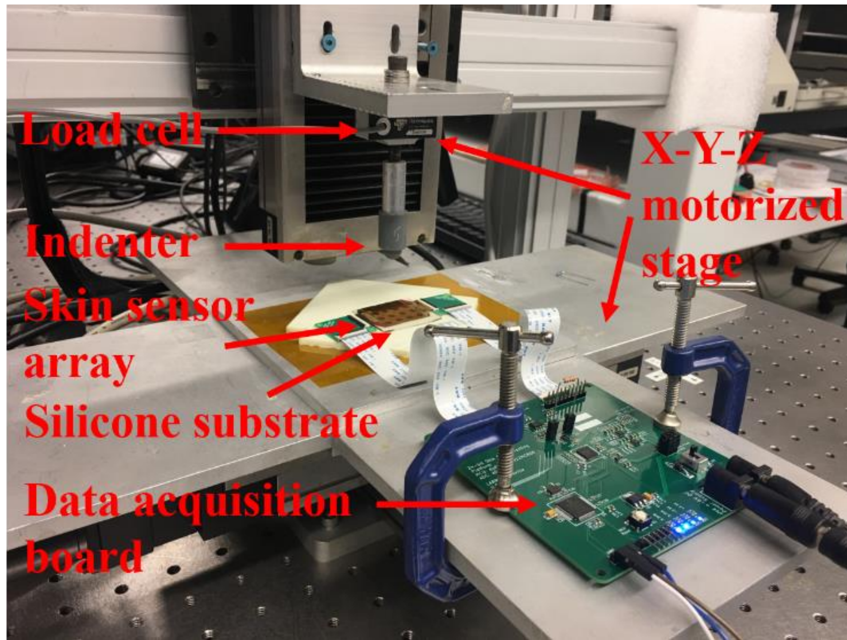

Figure 5. 5 Tactile sensor load testing station.

In the skin sensor patch, each sensing unit consists of two individual sensors that are physically stacked on each other, and electronically connected in series. Then, this unit is powered through a low-noise standard reference voltage source. The middle point of the two sensors is tapped by a 24-bit high-resolution ADC module (Texas Instruments™, ADS1258) (shown in Figure 5.6) to detect any voltage fluctuation, which reflects the strain the unit experiences. The converted voltage signal is collected by a Microchip® microcontroller unit (MCU, model dsPIC33EP512MC806) and transferred to a PC through a UART to USB dongle.

The sensor patch is "trampolined" between the two Molex™ connectors (model 503480-3200). Within each sensing unit, the two sensor cells stack together "back-to-back". This configuration implies that when strain presents on one sensing unit, the two sensor cells deform or strain in opposite directions, hence resistance changes in "differential mode" rather than "common mode" (one increases and the other decreases). This effect essentially enhances the sensitivity of each sensing unit.

A buffered 26mV reference voltage is applied to the two resistors in series (the sensing unit). Ideally, the mid-point of the two resistors should output 13mV if the two sensor cells are identical. A 24-bit high-resolution analog-to-digital converter (ADC) of ADS1258 from Texas Instrument™ was used to detect the mid-point voltage change, which all 16 input channels are multiplexed so that the input signals can be routed out of the IC, externally conditioned, and routed back to digitalize.

In our case, the ADC was operated under single-ended input and bipolar power mode. Each input channel (AINx) of the ADC taps into a mid-point of the sensing unit, and a buffered 13mV DC signal is fed into the input common terminal (AINCOM) of the ADC. The 13mV is the expected resting voltage of the sensing unit, in an ideal world. We refer to this voltage as a baseline. Before a conversion happens, the internal multiplexer (MUX) routes the input voltage present at the AINx pin along with the 13mV baseline voltage present at the AINCOM pin out of the IC by MUXOUTP and MUXOUTN pins to an external instrumentation amplifier INA333, also from TI™, to amplify the voltage difference.

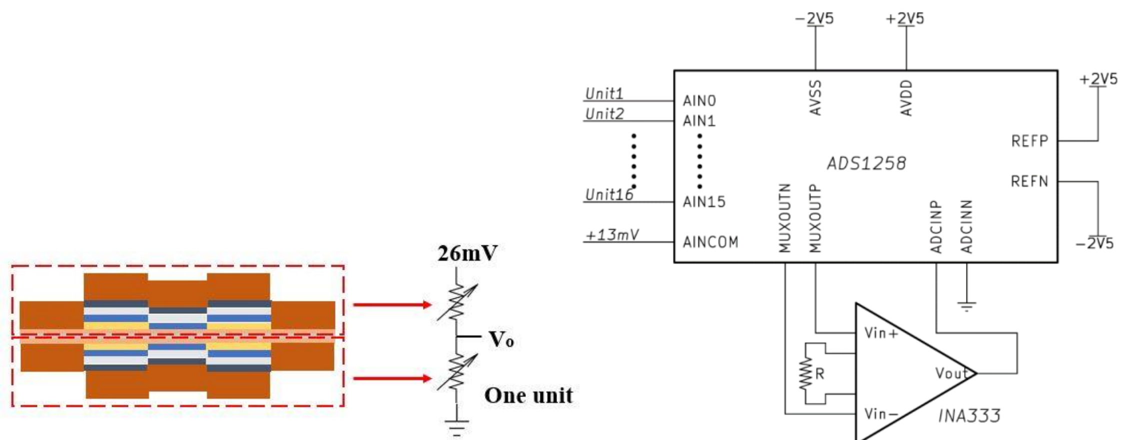

Figure 5. 6 Top: a pair of sensors representing two potentiometers in series connection; bottom: strain sensing circuit diagram. REEP, REFN pins are the reference voltage, AVDD is the positive supply and the AVSS is the negative supply.

5.1.1.5 Experimental Results and Discussion

Before doing the lamination of the sensor arrays, every single sensor's resistance is measured and recorded. This step is to prepare for two sensor arrays selection to laminate a double-side (back-to-back) sensor array. The selection is based on the corresponding resistance of sensors that are closed. As a double-side sensor array, two single sensors which are back-to-back laminated together become a pair. For this situation, those pairs are 2-10, 1-9, …, 7-15, and 8-16 after back-to-back lamination. Figure 5.7 shows the arrangement of the sensors and electrodes of the sensor array, and the resistance of each sensor is listed in Table 5.1. Two single sensors' resistances of each pair are close, which is significant for temperature compensation.

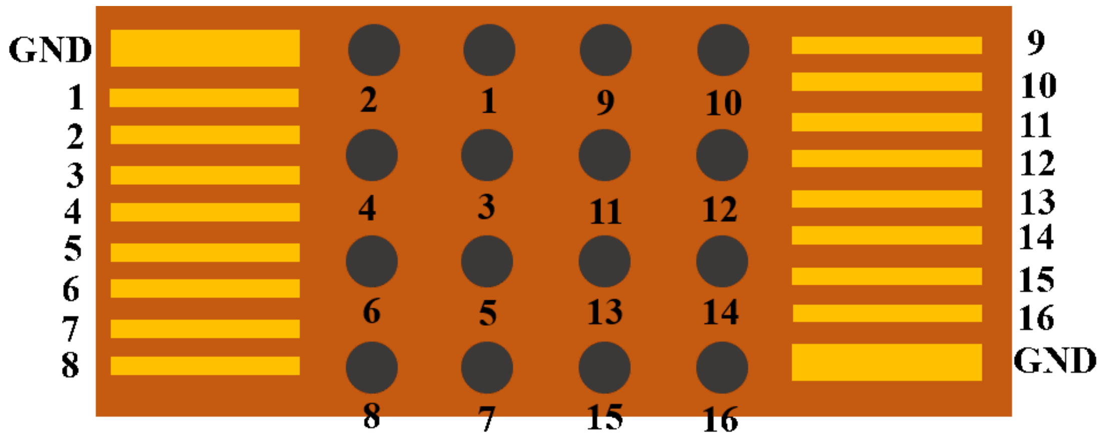

Figure 5. 7 Sensors and electrodes arrangement of a sensor array.

The sensor pair was placed on a soft Silicone substrate that deforms when subjected to pressure. When a load is applied on the sensor pair, the pair is squeezed by the pressure, the up-side sensor is compressed inwards, but the bottom-side sensor is extended outwards. Strain is developed due to the bottom Silicone layer compliance, in addition to the double-side laminate of the sensor.

Table 5. 1 Resistance measurement of two sensor arrays of a pair before lamination

Number of sensors	Resistance (Ω)	Number of sensors	Resistance (Ω)
1	40.8	9	62.3
2	56.5	10	43.6
3	39.3	11	43.2
4	35.7	12	60.3
5	43.6	13	60.1
6	37.4	14	60.5
7	34.1	15	41.1
8	34.2	16	35.1
Number of sensors	**Resistance (Ω)**	**Number of sensors**	**Resistance (Ω)**
1	54.4	9	47.1
2	50.8	10	51.4
3	42.3	11	34.9
4	46.8	12	43.7
5	70.8	13	41.9
6	53.3	14	47.4
7	78.9	15	44.6
8	54.6	16	53.5

Because of the piezoresistive material PEDOT: PSS between the star-shaped structures of the sensor, the resistance of the two sensors of the pair corresponds to increasing (up-side) and decreasing (bottom-side) when the load is applied. The ratio of the resistance of the sensor pair is changed to make V_o variable so that the ADC signals from the data acquisition board are varied and visualized the performance of the sensor strain gauge. With the variable load (0N-17.5N-0N) applied on the No. 5 sensor pair, the strain gauge performance of the No. 5 sensor pair and surrounding sensor pairs are shown in Figure 5.8. When the load reaches around 10N, other sensor pairs start to react with the load variation. Meanwhile, three sensor pairs, 7, 11, and 16 are less sensitive to the pressure of the load. This reduction of sensitivity may be due to the fact that lamination is still a manual process, thus prone to errors from the brayer and adhesive applicator.

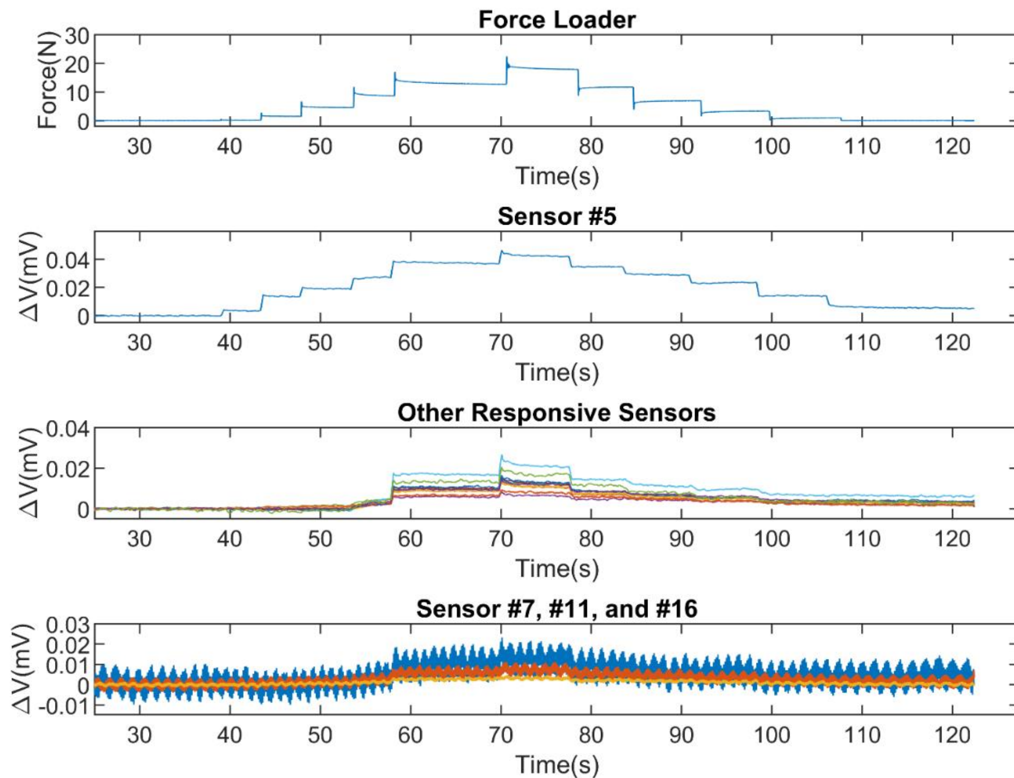

Figure 5. 8 Strain gauge performance of sensor pair with variable load applied on No. 5 sensor

5.1.2 Fabrication of Tactile Sensor in NeXus

In the NeXus system, instead of the fabrication process of the skin sensor in the cleanroom, we came up with a new skin sensor fabrication process by using an Aerosol Inkjet printing instrument to print sensor structures on the flexible polymer substrates, like Kapton® sheet, and an intense pulse light photonic instrument is employed to sinter the structures, an inspection function integrated with the microassembly station to check the printing and sintering results of the sensor structures. A PicoPulse instrument will be used to deposit PEDOT: PSS ink on the sensing area then using IPL to sinter the PEDOT: PSS ink. Two probes are mounted on the manipulators of the microassembly station to measure the resistance of each sensor and check the fabrication results. All the fabrication steps are

completed by transferring the 6-DOF positioner to different stations on the long optical table in the NeXus system, the so-called tactile sensor manufacturing line. All the steps are teleoperated from the LabVIEW user interface. Based on the repeatability and accuracy of instruments and positioner, the fabrication results of skin sensors can be guaranteed with high precision and yield of product.

5.1.2.1 Kinematic Design and Calibration of NeXus

Due to the complexity of the cleanroom fabrication process of the tactile sensors and the low repeatability and the yield of the product during the fabrication and lamination process, a new strain gauge sensor fabrication process was developed via the NeXus system using OPTOMEC® Aerosol Inkjet printer to print the strain gauge structure of tactile sensor on the flexible Kapton® substrate. This method can reduce fabrication procedures and increase the repeatability and yield of products. In the NeXus, several subsystems were employed to fabricate strain gauge sensors in Figure 5.9, such as the OPTOMEC® Aerosol Inkjet printing station, microassembly station, and the 6-DOF positioner. Here, an oven was used to cure or sinter the strain gauge structures printed by the Aerosol Inkjet printer. The IPL station will be employed to complete the sintering or curing process in the future.

Figure. 5.10 depicts the coordinate system of each NeXus process station, including additive manufacturing, curing, and metrology tools. For the strain gauge structure printing, it is first necessary to kinematically calibrate the coordinate systems of substrate [S], the 6-DOF positioner [O], OPTOMEC® Aerosol Inkjet printer head [H], and microscope camera [C], and measure the resulting gauge dimension in order to estimate calibration errors. The remaining part of this section discusses three calibration procedures employed to align the printing tool with the sample by means of optical metrology.

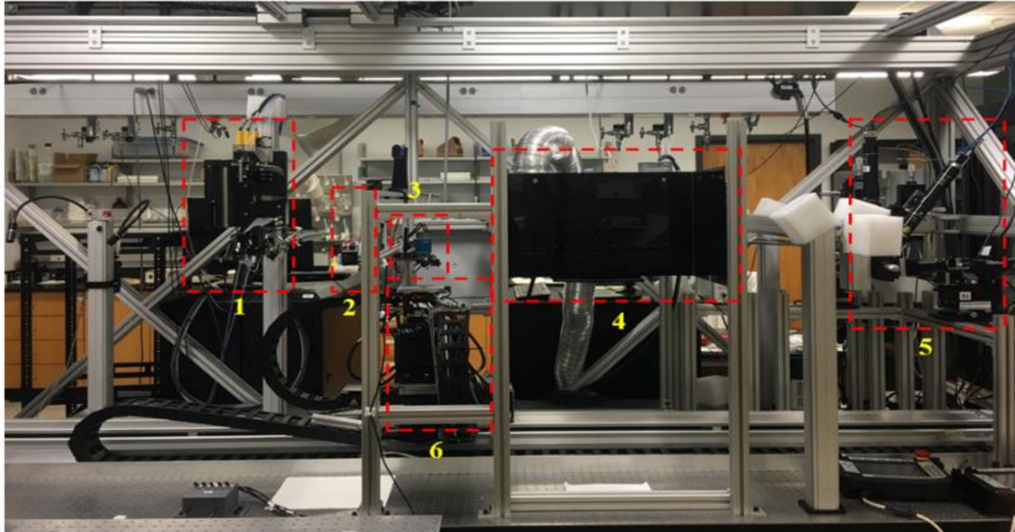

1. OPTOMEC Aerosol Inkjet printing station
2. Custom stationary 3D FDM printing station
3. PicoPulse Ink dispensing station
4. IPL sintering station
5. Microassembly station
6. Custom 6-DOF positioner

Figure 5. 9 Hardware on a long optical table: 1. OPTOMEC® Aerosol Inkjet printing station; 2. 3D FDM printing station; 3. PicoPulse® inkjet deposition station; 4. Intense Pulse Light (IPL) station; 5. Microassembly station; 6. 6-DOF positioner with the printed sample.

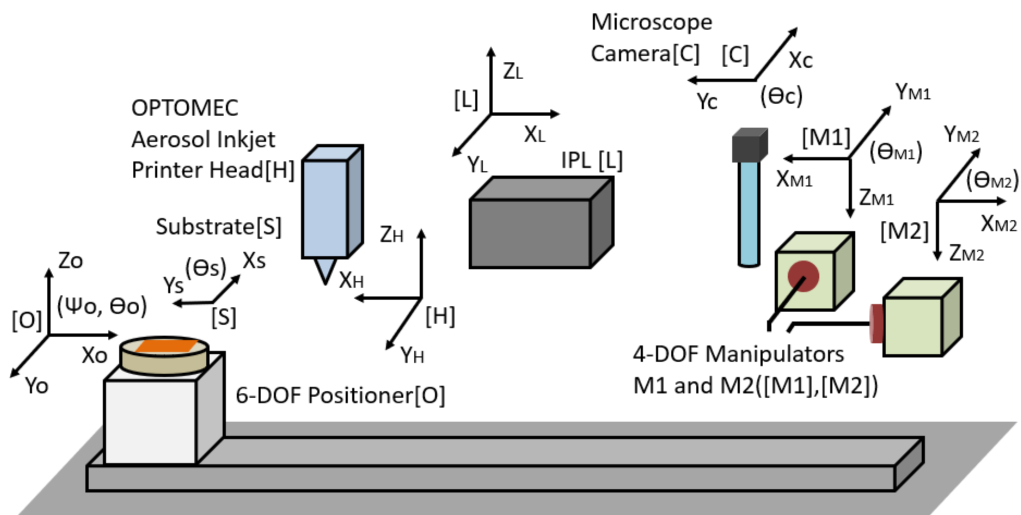

Figure 5. 10 Coordinate the frame and distribution of each subsystem for the skin sensor fabrication process in the NeXus.

5.1.2.1.1 Alignment of the center of sample chuck and printer head

The OPTOMEC® Aerosol Inkjet printer was mounted on the NeXus frame attached to an optical table. The width of the printed line was determined by adjusting several process parameters in its controller, such as sheath flow rate, atomizer flow rate, and atomizer current, as well as the stage motion speed of the 6-DOF positioner. The printing parameters have been characterized in [63, 64]. using a Design of Experiments approach for printing lines with 60-100µm width. After mounting the OPTOMEC printer nozzle, the X-Y-Z coordinates of the printer head are assumed to be constant with respect to the global origin. Before loading the substrate on the sample chuck, a reference point (the center of the sample chuck) was defined on the sample chuck to approximately identify the fiducial coordinates on the substrate when the origin of the substrate matches the center of the sample chuck closely after loading the substrate. In the kinematic calibration process, the center of the field of view (FOV) of the vertical camera in the microassembly station is defined to be the global origin [C] as this camera is fixed on the NeXus frame and the origins of other stations' coordinate systems are considered unknown and will be referred to it.

To align the center of the sample chuck with the OPTOMEC® printer head, we first locate the coordinate of the center of the sample chuck by moving the 6-DOF positioner along with the long linear stage while adjusting other stages to make the center of the sample chuck reach the center of the FOV of the vertical camera in the microassembly station. The current [X_{SC}, Y_{SC}] values of the 6-DOF positioner are the coordinate of the center of the sample chuck with respect to the global origin [C]. For

simplicity, the Z height and X_L movements are considered to be fixed during printing and metrology and are not considered in the identification process.

Second, in order to locate the printer head's coordinate, the 6-DOF positioner was moved under the OPTOMEC® station, the Y-X-T-R stages of the 6-DOF positioner were kept at their initial position and only the Z stage was moved up to keep the 4mm distance between the substrate surface and the tip of the Aerosol Inkjet printer head. A cross pattern was printed on a glass slide loaded on the sample chuck, then the 6-DOF positioner moved under the camera and adjusted its position to align the center of the cross to match the center of the FOV of the camera. The current [X_H, Y_H] values of the 6-DOF positioner are the coordinate of the Aerosol Inkjet printer head with respect to the global origin. The offsets [ΔX, ΔY] between the center of the sample chuck and the Aerosol Inkjet printer head were calculated as in Fig. 5.11:

$$\begin{bmatrix}\Delta X\\ \Delta Y\end{bmatrix} = \begin{bmatrix}X_H\\ Y_H\end{bmatrix} - \begin{bmatrix}X_{SC}\\ Y_{SC}\end{bmatrix} \tag{5.1}$$

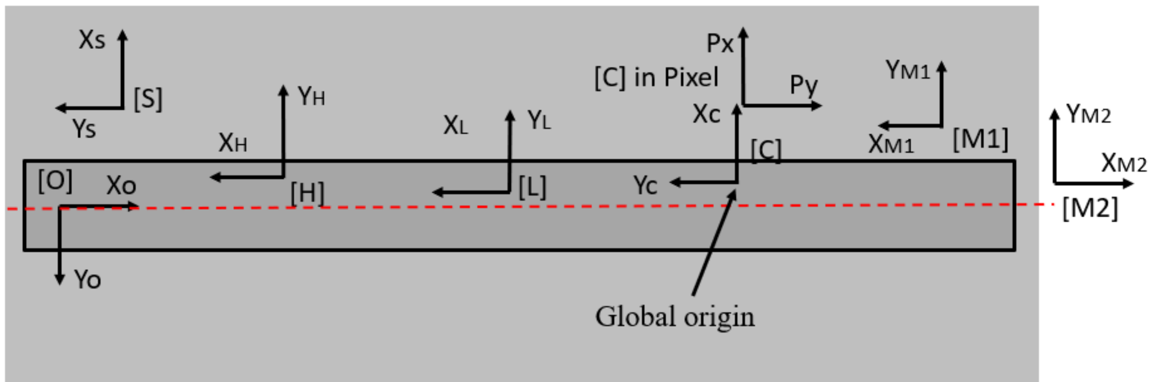

Figure 5. 11 The top view of the alignment of the center of the sample chuck to the printer head.

Third, based on the measured offsets between the center of the sample chuck and the Aerosol Inkjet printer head, they can be aligned as shown in Fig. 5.12. Table 5.2

displays the traveling distance of the long linear stage for each station during this process. When the 6-DOF positioner arrives at each station with the long linear stage, the long linear stage will not move anymore, and only the Y-X-Z-T-R stages above it are fine-adjusted to reach the target positions on the sample chuck.

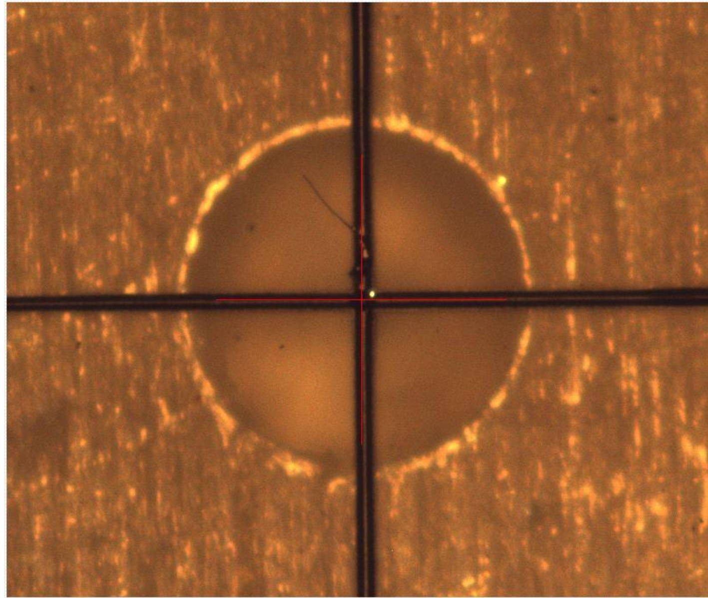

Figure 5. 12 Alignment of sample chuck center and OPTOMEC® printer nozzle.

Table 5. 2 IAI linear stage travel for each station.

Location of Station	Linear Stage Travel
Initial Position	0 mm
OPTOMEC® station	588 mm
3D FDM printer station	844.65 mm
PicoPulse® station	1080.65 mm
IPL station	1565.3 mm
Vertical Camera	2368.95 mm

5.1.2.1.2 Inverse Kinematic Calibration

After the alignment of the center of the sample chuck and the printer head, the center of the sample chuck is defined as the reference point for aligning and loading the substrate on

the sample chuck. For example, an arbitrary point (X_0, Y_0, θ_0) on the sample chuck with a certain angle θ rotation is desired to be moved to the center of the sample chuck. The mathematical relationship for the inverse kinematic function can be expressed in the following equations (Fig. 5.13):

$$\theta_0 = \tan^{-1} {}^{Y_0}\!/_{X_0}, \theta_1 = \theta_0 + \theta \quad (5.2)$$

$$D = \sqrt{X_0^2 + Y_0^2} \quad (5.3)$$

$$X_1 = D\cos\theta_1, Y_1 = D\sin\theta_1 \quad (5.4)$$

where $X_0, Y_0,$ and θ_0 are the initial coordinate of the arbitrary point on the substrate with respect to the center of the sample chuck, θ is the desired orientation, $X_1, Y_1,$ and θ_1 are the calculated coordinate of the new position of the arbitrary point after θ degrees rotation.

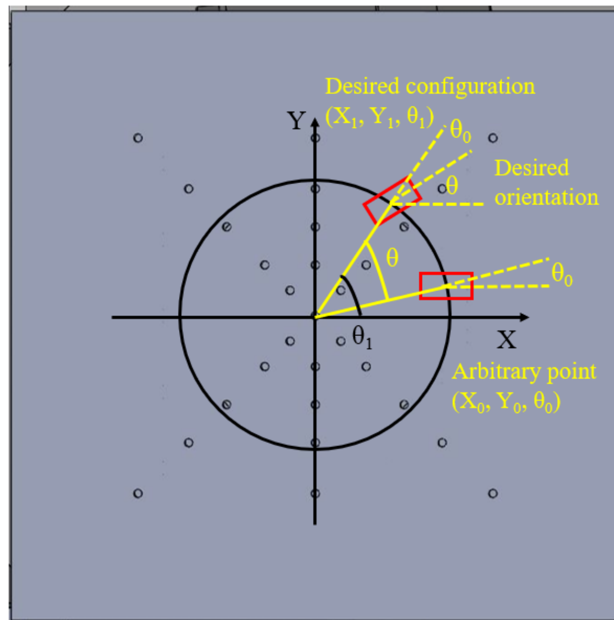

Figure 5. 13 An arbitrary point moves to the center of the sample chuck with the desired orientation.

Here, $X_0, Y_0,$ and θ are inputs, the values of X_0 and Y_0 can be measured from the CAD layout referred to the origin of the substrate. When loading the substrate on the sample chuck, the origin of the substrate needs to be aligned with the center of the sample

chuck approximately so that the value of X_0 and Y_0 will be estimated with respect to the center of the sample chuck, while θ_0 and D can be calculated through the values of X_0 and Y_0. X_1 and Y_1 are the calculated outputs, which will determine the relative motions of the X and Y stages to move the arbitrary point to the center of the sample chuck with θ orientation. Last, this arbitrary point can be the starting point for printing structure by the OPTOMEC® Aerosol Inkjet printer. Finally, the calibrated distance [ΔX', ΔY'] between the arbitrary point and the printer head can be calculated by:

$$\begin{bmatrix} X_1 \\ Y_1 \\ \theta \end{bmatrix} = \begin{bmatrix} \cos\theta_1 & 0 & 0 \\ 0 & \sin\theta_1 & 0 \\ 0 & 0 & 1 \end{bmatrix} \begin{bmatrix} D \\ D \\ \theta \end{bmatrix} \tag{5.5}$$

$$\begin{bmatrix} \Delta X' \\ \Delta Y' \end{bmatrix} = \begin{bmatrix} X_H \\ Y_H \end{bmatrix} - \begin{bmatrix} X_1 \\ Y_1 \end{bmatrix} \tag{5.6}$$

5.1.2.1.3 Visual Servoing Calibration

When the substrate is loaded on the sample chuck, the origin of the substrate is aligned with the center of the sample chuck. Thus, the coordinates of all features on the substrate can be known with respect to the center of the sample chuck based on the design layout of the substrate. Even though the alignment is as good as possible, there still exist offsets in translation and rotation when a pre-fabricated substrate fiducial mark is brought into the camera's FOV with the inverse kinematic calibration mentioned above. The center of the fiducial mark can be further fine-adjusted to move to the desired orientation and position in the camera's FOV with a visual servoing function. The equations below express the relationship between the difference in the configuration of the center of the template in image pixels and the difference in the stages' movements with the image Jacobian involved. ΔP_X, ΔP_Y, and ΔP_θ are the differences in the configuration of the template center

in pixels, $\Delta X, \Delta Y,$ and $\Delta\theta$ are the difference in the stages' motion, while the image Jacobian J_{image} is expressed as:

$$\begin{bmatrix} \Delta P_X \\ \Delta P_Y \\ \Delta P_\theta \end{bmatrix} = J_{image} \times \begin{bmatrix} \Delta X \\ \Delta Y \\ \Delta\theta \end{bmatrix} \tag{5.7}$$

$$J_{image} = \begin{bmatrix} J_{11} & J_{12} & J_{13} \\ J_{21} & J_{22} & J_{23} \\ J_{31} & J_{32} & J_{33} \end{bmatrix} \tag{5.8}$$

Since the image Jacobian is a 3 x 3 matrix that has 9 entries, a linear least squares estimation method was applied to find the entries' values of the image Jacobian. After the image Jacobian was defined, the center of the template was moved to the desired position and orientation achieved by the following equation:

$$\begin{bmatrix} X_{new} - X_c \\ Y_{new} - Y_c \\ \theta_{new} - \theta_c \end{bmatrix} = \Delta s \times J_{image}^{-1} \begin{bmatrix} P_{X_d} - P_{X_c} \\ P_{Y_d} - P_{Y_c} \\ P_{\theta_d} - P_{\theta_c} \end{bmatrix} \tag{5.9}$$

where X_c, Y_c, θ_c, X_{new}, Y_{new}, and θ_{new} are the current and new configurations of the 6-DOF positioner; P_{X_d}, P_{Y_d}, P_{θ_d}, P_{X_c}, P_{Y_c}, and P_{θ_c} are values in pixel of the desired and current position and orientation of the center of the fiducial mark in the camera's FOV, Δs represents a step size of the stages' movements. Based on the vision feedback values, the fiducial mark can be moved to the desired position and orientation in a fast and precise method by using the visual servoing technique. After the visual servoing adjustment, the starting point for printing can be located more precisely and matched the tolerance of the printing.

5.1.2.1.4 Calibration results

After kinematic calibration of the NeXus for skin tactile sensor fabrication, the designated substrate is loaded on the sample chuck and aligned. By using the inverse

kinematic calibration, the fiducial mark was moved into the FOV of the camera, and then using visual servoing calibration, the fiducial mark was adjusted to the desired position and orientation with the image Jacobian assistance. The value of the image Jacobian was calculated by the least-squares method by collecting 50 random X, Y, and θ values of the center of the fiducial mark. Fig. 5.14 depicts the fiducial mark location before and after the visual servoing calibration. The desired position is the center of the camera's FOV, the desired orientation is 0 degrees. In the visual servoing calibration, there has a +/- 1 pixel (around 1.33μm) tolerance in translational adjustment and a +/- 0.5-degree tolerance in rotational adjustment.

$$J_{image} = \begin{bmatrix} -0.0003315 & 0.00125767 & 0.281908 \\ -0.0017776 & 0 & 0.302763 \\ 0 & 0 & -1 \end{bmatrix} \tag{5.10}$$

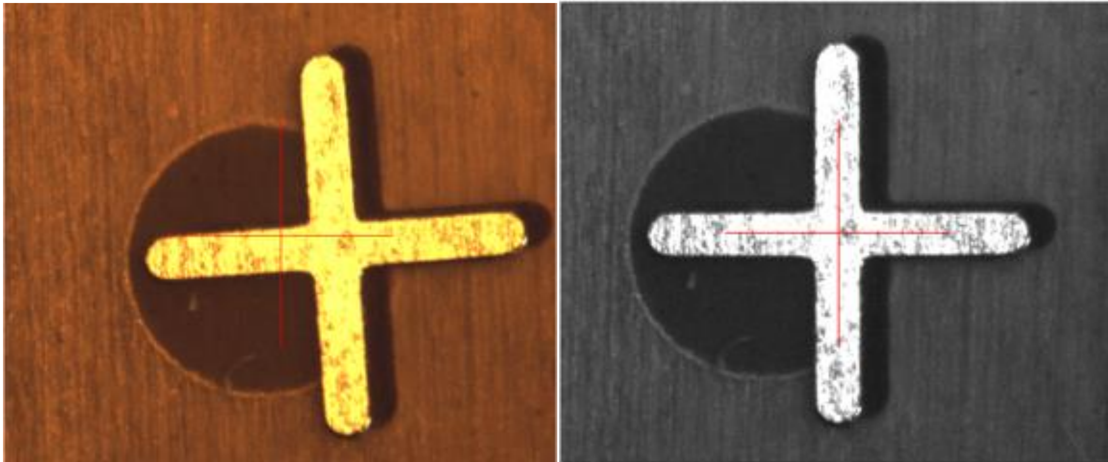

Figure 5. 14 Fiducial mark location before and after visual servoing adjustment.

After the fiducial mark was aligned to the center of the camera's FOV, the starting point for printing need to be determined on the contact pad. Here, the center of the pad-4 was selected for the starting point for printing and moved to the center of the FOV of the camera by the layout dimension 11.27mm x 31.47mm in Fig. 5.15. Due to the uncertainties

of the calibration process, the printing precision was investigated with 5 samples. The starting point for the printing strain gauge structure was measured on the contact pad-4 compared with the design in the CAD model as shown in Fig. 5.16, while the endpoint was measured on the contact pad-3. Based on the CAD model, the tolerance for printing a functional gauge is 650μm (half of the 1.3mm pad size), but the actual measured tolerance for printing on the manufactured contact pad is around 620μm. The distances between the center of the fiducial mark to the center of the pad-3 and pad-4 were measured and listed in Table 5.3 and the offsets of starting point at the center of the pad-4 and the endpoint at the center of the pad-3 were measured and listed in Table 5.4.

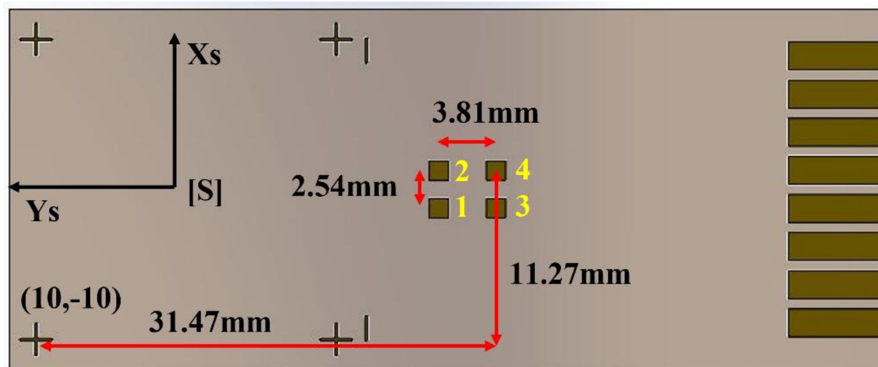

Figure 5. 15 Dimension of fiducial and contact pads on the substrate

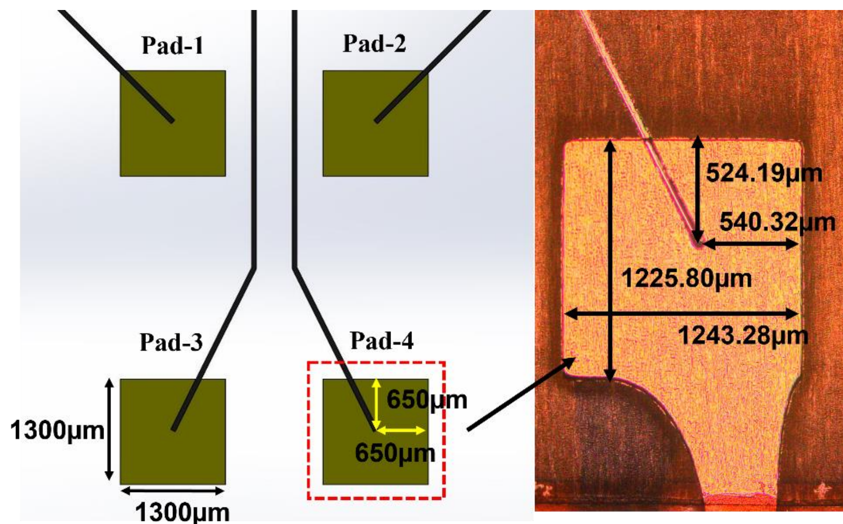

Figure 5. 16 Dimension of the starting point on pad-4 of sample-3.

Table 5. 3 Distances between fiducial to the center of pad-3 and pad-4 in CAD model and measured samples

Sample	**Distance between fiducial to the center of the pad-3 and pad-4 (Unit: mm)**			
	Pad-3		***Pad-4***	
	X	***Y***	***X***	***Y***
CAD	8.73	31.47	11.27	31.47
Sample-1	8.535	31.516	11.063	31.532
Sample-2	8.532	31.57	11.082	31.6
Sample-3	8.59	31.507	11.132	31.512
Sample-4	8.536	31.525	11.076	31.537
Sample-5	8.53	31.508	11.07	31.53
	ΔX	***ΔY***	***ΔX***	***ΔY***
Sample-1	-0.195	0.0459	-0.207	0.062
Sample-2	-0.198	0.0999	-0.188	0.13
Sample-3	-0.14	0.0369	-0.138	0.0419
Sample-4	-0.1941	0.0549	-0.194	0.0669
Sample-5	-0.2	0.038	-0.2	0.06

Table 5. 4 Offsets of the starting pointing to the center of pad-4 and the endpoint to the center of pad-3

Sample	**Offsets of the starting point to the center of the pad-4 and the endpoint to the center of the pad-3 (Unit: µm)**			
	Pad-3		***Pad-4***	
	ΔX'	***ΔY'***	***ΔX'***	***ΔY'***
Sample-1	-68.5	-35.6	-85.4	-16.1
Sample-2	-56.6	-46.4	-74.6	-63.8
Sample-3	-87.4	-72.6	-81.3	-88.7
Sample-4	-89.4	-82.0	-93.4	-90.1
Sample-5	-109.9	-83.3	-101.2	-102.2

A calibration precision metric, Cal_P, was defined to express the standard deviation of the difference of the distances between the center of the fiducial mark to the center of the contact pads in layout design and the actual manufactured substrate shown in Table III, as well as the offsets of the starting point to pad-4's center and endpoint to pad-3's center compared with the actual locations of the starting point and endpoint printed on pad-4 and pad-3 shown in Table 5.5. The equation is expressed below:

$$Cal_P = \sqrt{\sum_{i=1}^{N}[(\Delta X_i + \Delta X_i')^2 + (\Delta Y_i + \Delta Y_i')^2] / N} \quad (5.11)$$

where ΔX_i and ΔY_i are the difference in the distance between the center of the fiducial to the center of pad *i* and in the measured samples and the CAD model layout. $\Delta X_i'$and $\Delta Y_i'$are the offsets between the starting point on pad *i* and the center of the pad, while *N* is the number of the contact pads considered. The resulting calibration precision using N=2 (pad-3 and pad-4) is listed in Table V. distances between the fiducial to centers of pad-3 and pad-4 in the CAD model and measured samples.

The average calibration precision Cal_P=169.1µm ±28.2µm is large, but it is mostly due to manufacturing tolerances of the pre-fabricated substrates, and much less to the robotic precision of the NeXus. Even so, the calibration precision is considerably less than the printing tolerance on the contact pads, which is around 620µm (Fig. 5.16).

Table 5. 5 Calibration precision of the sensor printing

Sample	Calibration precision (µm)
Sample-1	147.5
Sample-2	214.3
Sample-3	132.3
Sample-4	179.5
Sample-5	171.6
Average	169.1
Standard Deviation	28.2

5.1.2.2 Tactile Sensor Design

In our previous double-layer tactile sensor design, when the load is applied on the single sensor, one side of the sensor has a compressive strain, and the other side has a tensile strain. For our new tactile sensor, we came up with a combined-structure design and only fabricate the sensor on one side of the substrate as shown in Fig. 5.17. The combined-structure tactile sensor has two individual strain gauge structures: arc structure and radial

structure. Those two strain gauge structures have extremely opposite performances when the load is applied to the center of the tactile sensor. The radial structure is a kind of circular serpentine structure as the normal strain gauge performance, when the load is applied, the resistance of the radial structure is increasing. Whereas, the arc structure has the opposite strain gauge performance, in another word, when the load is applied, the resistance of the arc structure is decreasing. Therefore, the combined-structure tactile sensor has the opposite strain gauge performance within the load is applied, which has an outstanding advantage to fabricate the tactile sensor on one side of the substrate. The outer diameter of the tactile sensor is 6mm and inner diameter is 3.2 mm, and the width of the structures is around 100 microns. They are fabricated on the designated Kapton® substrate.

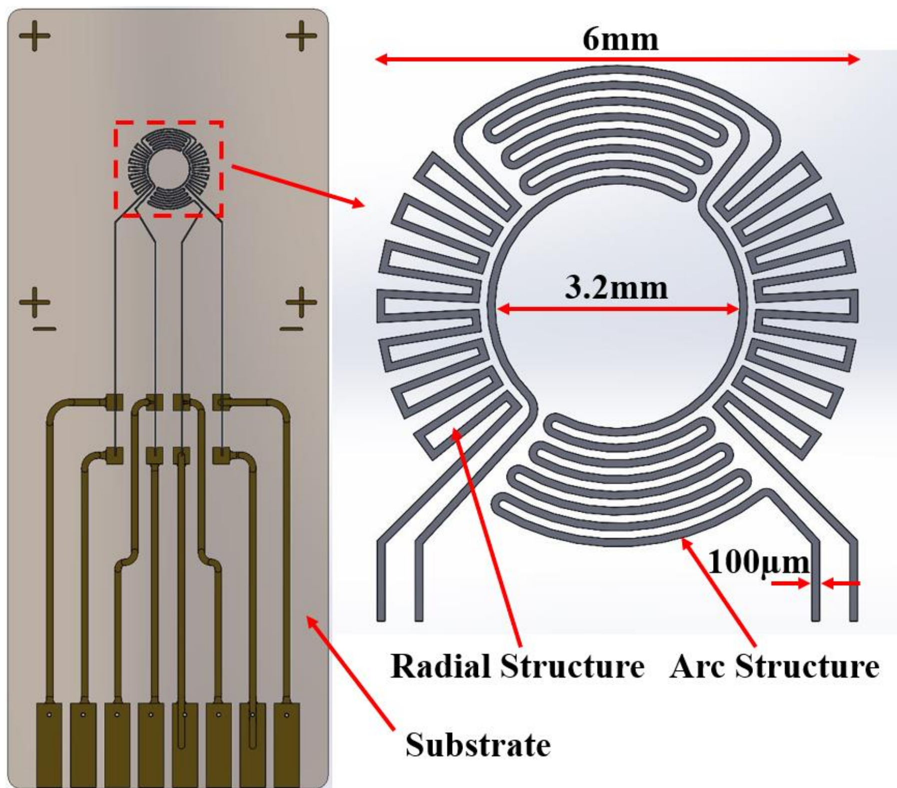

Figure 5. 17 Design of the tactile sensor with two individual strain gauge structures.

5.1.2.2.1 Principle of Tactile Sensor Design

No matter the previous double-layer tactile sensor or this combined-structure tactile sensor, they are both treated as two variable resistors that are in series connected in the circuit. For the combined-structure tactile sensor, each variable resistor represents the individual structure, R_1, and R_2 as shown in Fig. 5.18(a). When there is no load applied to the sensor, the V_{out} can be represented by $R_1, R_2, and\ V_{in}$ as equation (5.12).

$$V_{out} = \frac{R_2}{R_1+R_2} V_{in} \quad (5.12)$$

If,

$$R_1 = R_2\ or\ R_1 \approx R_2 \quad (5.13)$$

Then,

$$V_{out} = \frac{1}{2} V_{in} \quad (5.13)$$

When the load is applied to the center of the combined-structure tactile sensor, the resistances of two individual structures will be changed. For example, the R_1 increases ΔR_1, and the R_2 decreases ΔR_2 as shown in Fig. 5.18 (b).

$$V_{out} = \frac{R_2-\Delta R_2}{(R_1+\Delta R_1)+(R_2-\Delta R_2)} V_{in} \quad (5.14)$$

If,

$$\Delta R_1 \cong \Delta R_2\ and\ R_1 \cong R_2 \quad (5.15)$$

Then,

$$V_{out} = \left(\frac{1}{2} - \frac{1}{2}\frac{\Delta R_2}{R_2}\right) V_{in} \quad (5.16)$$

$$V_{out} = \frac{1}{2} V_{in} - K_2 \frac{1}{2} V_{in}, \ \ K_2 = \frac{\Delta R_2}{R_2} \quad (5.17)$$

where K_2 is the sensitivity of R_2 varied by a different applied force. In order to make that R_1 approximately equal to R_2, the total length of two individual structures must be almost equal to each other. In the CAD design, the length of the arc structure is 90.65mm, while the length of the radial structure is 90.6mm.

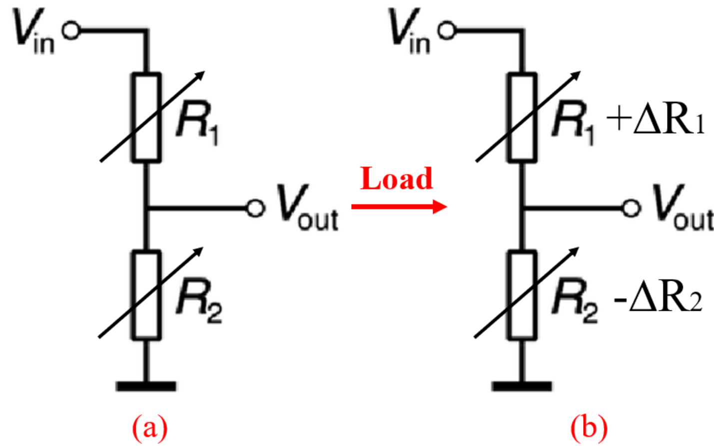

Figure 5. 18 Design principle of the combined structure tactile sensor.

5.1.2.2.2 Simulation of Tactile Sensor

According to the CAD design of the combined structure tactile sensor, the finite element analysis (FEA) is employed concentrated on the sensing area via the COMSOL® software. The simulated results of the sensitivities of the radial structure and arc structure are performed in the opposite directions when the load is applied in the center of the sensor as shown in Fig. 5.19.

The simulation results are obtained using COMSOL Multiphysics® for the finite element analysis. Force applications and resistance derivations are set up with Solid Mechanics and Electric Currents models in the Stationary Study of the COMSOL computation. Default Physics-controlled mesh and "normal" size of element size are selected for the building blocks. Note that the geometric nonlinearity option needs to be checked in the study setting of the stationary method in the mechanic package for the

electric current derivation. Other build-ins including materials such as the Polydimethylsiloxane (PDMS) bedding and indenter, the Polyimide (Kapton) backing of silver ink, and the silver ink itself are continently used. The mechanical properties of the material can be seen in Table 5.6. The sensitivities of the radial and arc structures perform in Fig 5.19 when the force increases from 0N to 4N.

The sensitivities are not expected to be a perfectly linear, since the bedding is not linearly expanded in either X or Y directions due to the different stiffnesses of the material involved (silver ink, Kapton, and PDMS) while the load is applied. It is further complicated with the multiple interweaved radial and arc structures. The simulation tolerance is 0.001 while the simulation time for each point is about 15 minutes using a Penguin 7 CPU. Depending on the size of material, a 4mm-thick the silicone substrate does not play an active role of a resistor, the meshing is coarse and finer near the Kapton layer (50μm thick), which is thinner and meshed with a finer element itself. Similarly, the silver layer (5μm thick) on the top is the thinnest and therefore meshed finest. The indenter of a few mm thick on the top then is meshed coarsely. The meshes are generated automatically and the default element size setting is “normal” which can handle most of the cases.

Table 5. 6 Mechanical and electrical properties of the materials. (Table acknowledgment: Ji-Tzuoh Lin)

Material	**Property**		
	Young’s Modulus (Pa)	***Poisson ratio***	***Electric conductivity (S/m)***
PDMS	750×10^{3}	0.49	0
Polyimide	3.1×10^{9}	0.34	0
Silver	83×10^{9}	0.37	61.6×10^{6}

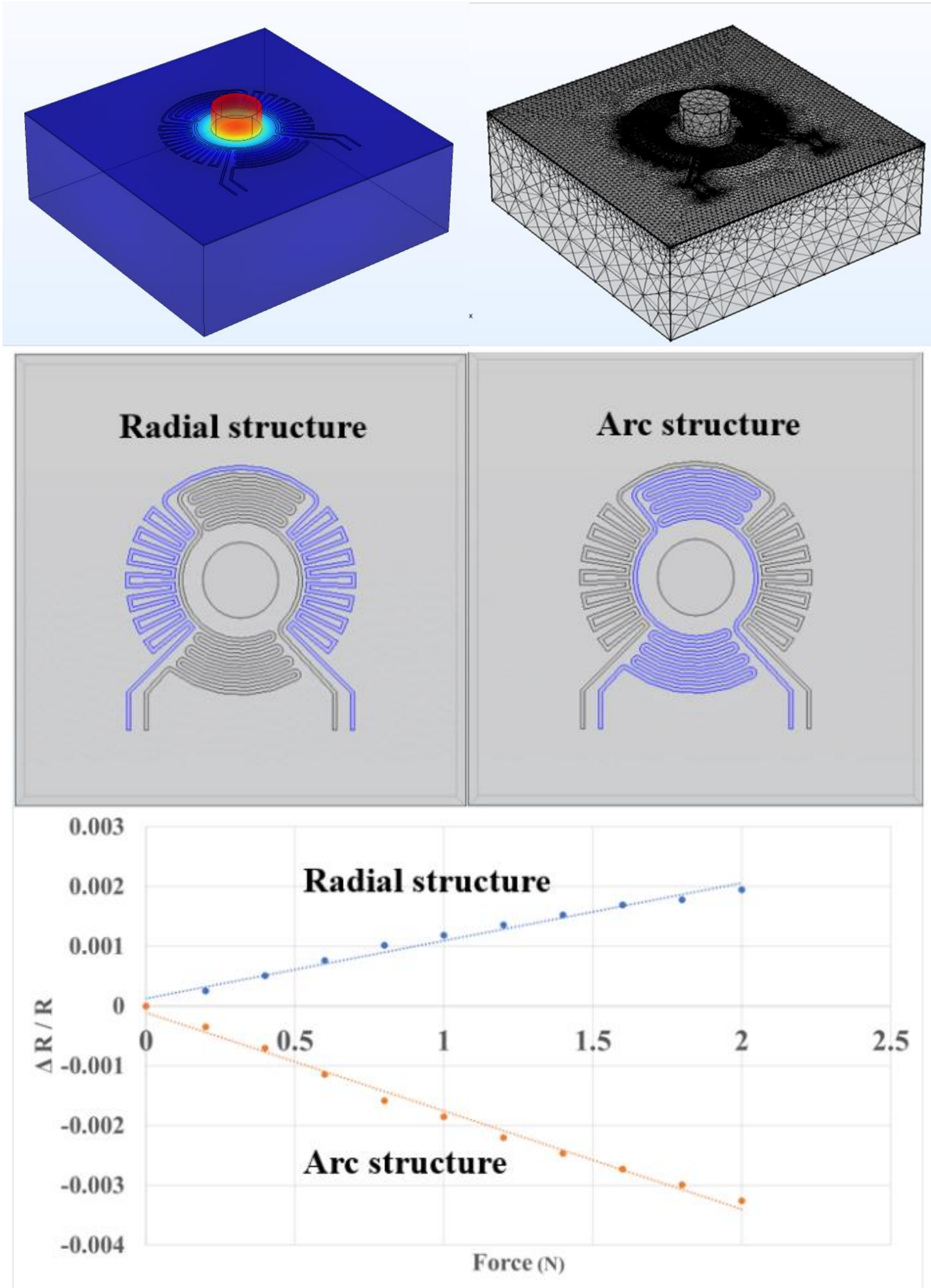

Figure 5. 19 Simulated results of the tactile sensor via COMSOL®. (Figure acknowledgment: Ji-Tzuoh Lin)

5.1.2.3 Fabrication Process of Tactile Sensor

Previously fabrication process of the tactile sensor was realized in Cleanroom, which was determined to be complicated, low efficiency, and characterized by the low yield of the product. As an alternative, we have proposed a novel fabrication method for the combined-structure tactile sensor, which involves the NeXus system: a custom multi-scale additive manufacturing platform designed and developed by our group [65]. In the NeXus, it was incorporated a precision sensor manufacturing line, including a high precision 6 degrees of freedom (DOF) positioner, an OPTOMEC® Aerosol Jet printer, an Intense Pulse Light (IPL) sintering station, and a microassembly station with high magnification optical microscopes for inspection on a 3m long optical table. The 6-DOF positioner is a sample carrier to transfer the sample among different stations for the manufacturing process. In [66], we investigated the kinematic design of the 6-DOF positioner and In [67], we discussed the calibration of the tactile sensor fabrication process in the NeXus. The tactile sensor was directly printed on the designated Kapton® substrate via the OPTOMEC® Aerosol Jet printer with around 100 microns width in silver ink (NovaCentrix® JS-A426). The tactile sensors were sintered via Oven at 200°C in current experiments, whereas the IPL sintering station will be employed to sinter the printed tactile sensors in the future. The printed tactile sensor is shown in Fig. 5.20.

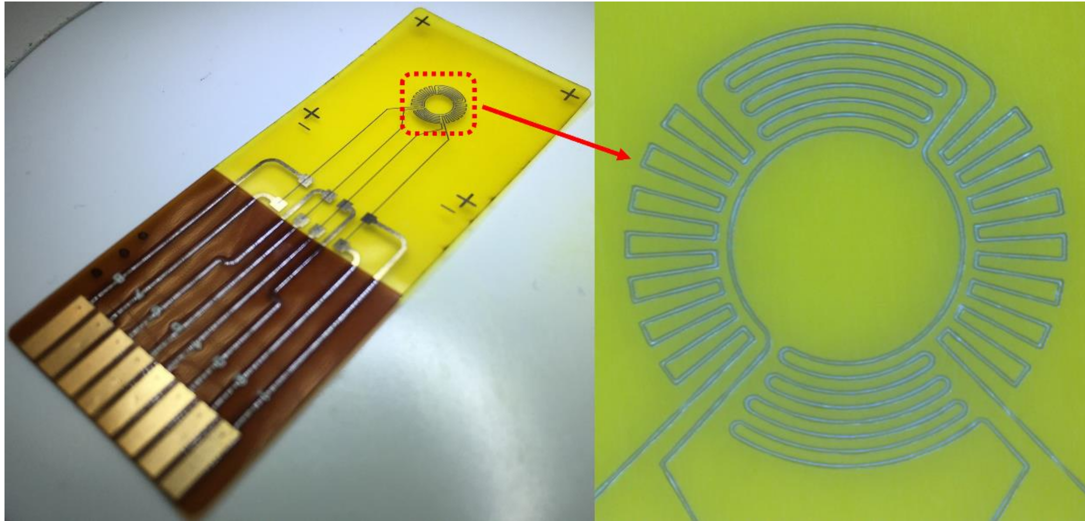

Figure 5. 20 Printed tactile sensor on the Kapton® substrate.

5.1.2.4 Experimental Setup

To characterize the combined-structure tactile sensor, we designed several specific experiments with load tests, temperature performance, and system identification evaluation. For the load test, there are two methods to detect the tactile sensor performance when the load is applied. One method is using a single sub-indenter on the cover made of soft PDMS material, which can reduce deformation coupling, and propagation of wrinkles, and enhance the single-to-noise ratio of tactile measurement, to transfer the load forces from the main indenter to the center of the tactile sensor. The other method is using a PDMS cover with multiple sub-indenters to measure the sensor's performance of the load from different directions.

5.1.2.4.1 Temperature Drift Test

Considering the temperature compensation of the tactile sensor in the actual application, the combine-structure tactile sensor was characterized under different temperatures using a Linkam Scientific Instruments® Analysa-LTS350 Temperature Chamber as shown in Fig. 5.21. The sensor sample was loaded in the chamber and the

variable resistances were measured under the temperature steps of 20-40-60-80-100°C.

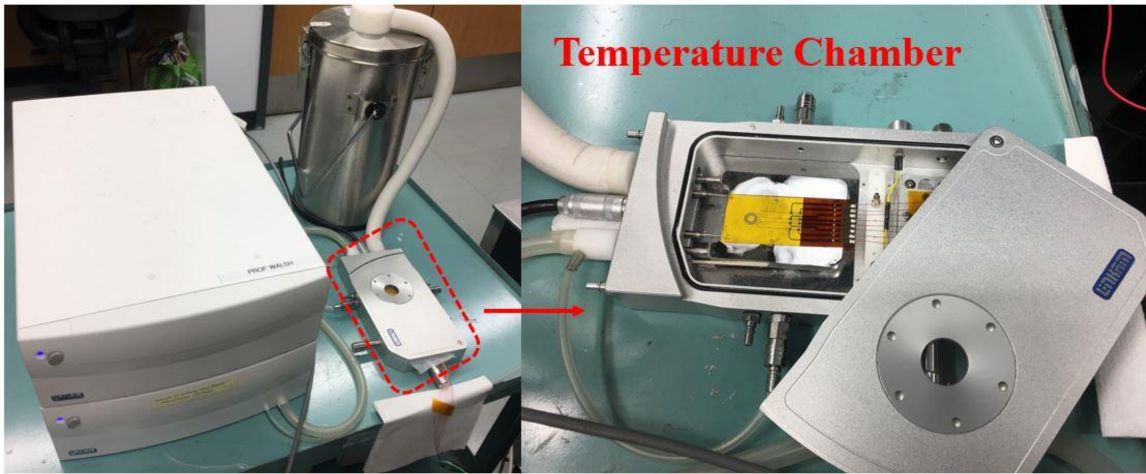

Figure 5. 21 Linkam Scientific Instruments® Analysa-LTS350 temperature chamber.

5.1.2.4.2 Single Sub-indenter Test

Figure. 5.22 depicts the load test bench for the tactile sensor, it consists of three Newport® UTM150CC1HL motorized linear stages, a load cell with a 6mm diameter round indenter at the end to press the PDMS cover, which has a 2mm diameter half-sphere sub-indenter, to apply the force to the tactile sensor. The variable resistances of the radial structure and arc structure of the tactile sensor are measured via an Agilent® 34970A with an Agilent® 34901A 20-channel multiplexer to collect resistances with a 4-wire resistance measurement method. Under the sensor sample, there is a circular PDMS bed to create a soft and elastic substrate. Therefore, during applying and releasing the load, the Kapton® substrate can deform gently. In this method, a single force (1N and 2N), is applied to the sensor, and a ladder force, 0-0.5-1-1.5-2N, is also applied to the sensor. The sensitivities of the sensor under different loads are measured and calculated.

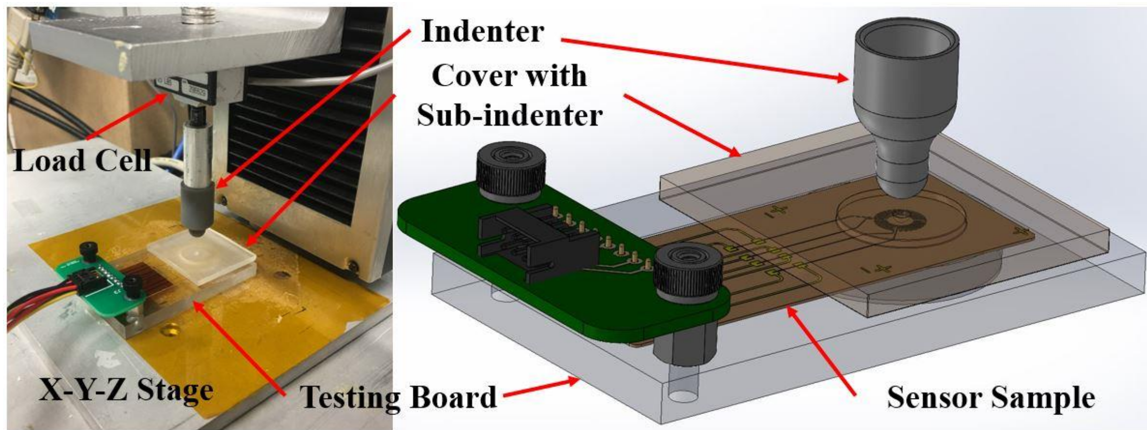

Figure 5. 22 Single sub-indenter load test.

5.1.2.4.3 Multiple Sub-indenters Test

To characterize the performance of the tactile sensor along with different directional loads and different distance from the center of the sensor, a PDMS cover with multiple 3mm diameter half spherical sub-indenters were fabricated as shown in Fig. 5.23. The sub-indenters are distributed from the center of the sensor to the outer on a 12mm diameter circle and a 24mm diameter circle. The 2N load was applied on each sub-indenter and the resistances of the sensor were measured.

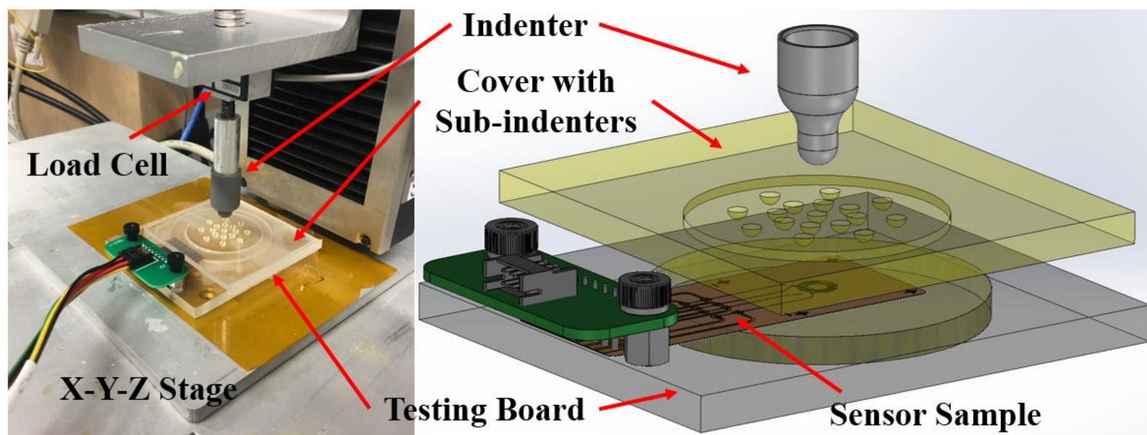

Figure 5. 23 Multiple sub-indenters directional load test.

5.1.2.4.4 2x2 Sensor Array Test

After characterizing a single tactile sensor, for a larger scale, a 2x2 sensor array

was fabricated on the specific Kapton® substrate. A 7x7 sub-indenter PDMS cover was made for the sensor array test with the 4N force in Fig. 5.24. A total of 8 individual resistances of 4 sensors are measured separately via the Agilent® 34901A 20-channel multiplexer. The indenter will apply the force on each sub-indenter location. The distance between each sub-indenter is 6mm. 4 sub-indenters are exactly in the center of the sensors.

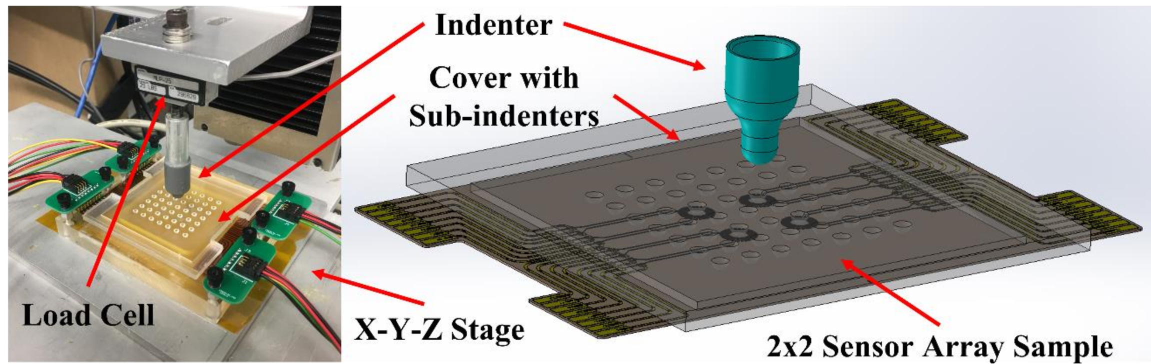

Figure 5. 24 2x2 sensor array load test.

5.1.2.5 Experimental Results and Discussion

5.1.2.5.1 Oven Sintering

A Series of experimental trials were conducted in order to evaluate fabricated tactile sensors and validate the proposed design combined radial and arc strain gauge structures. For that purpose, we have studied a number of tactile sensors which were thermally treated at different conditions: constant temperature of 200°C and varied sintering duration times from 2 to 20 hours. Figure 5.25(A) presents the average resistance values of the sensor structures depending on the sintering duration times. It is evident that with an increase in sintering duration time, resistances of both structures are not only decreasing but also the distribution of their values from sample to sample is getting narrower. Resistance is reduced from 150Ω with a standard deviation of about 20Ω for 2 hours of sintering time to approximately 50Ω with a standard deviation of about 3Ω. Another advantage of the longer

sintering time is a decrease in resistance differences between the radial and arc structures $|R_{radial} - R_{arc}|$ (shown in Figure 5.25(B)) that is a critical factor in the context of the compensation of the temperature effects on the sensor's performance.

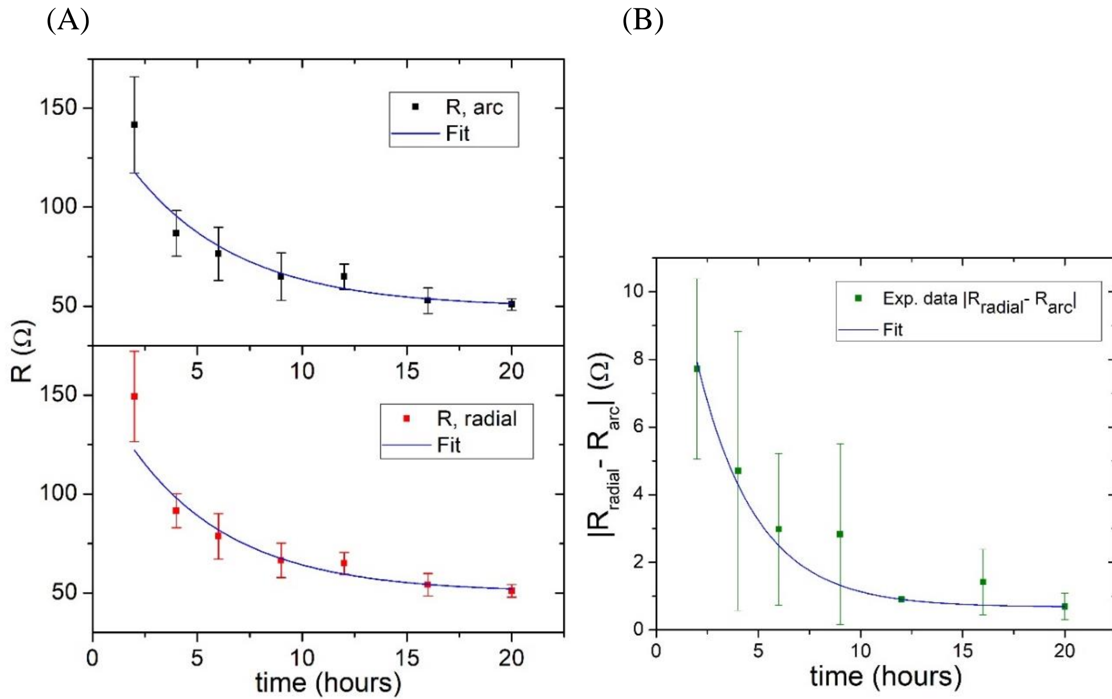

Figure 5. 25 A) Sensor's structure resistance dependence on the sintering time at 200°C and 0N load; B) variation of resistance difference between sensor's structures with the sintering duration time. (Figure acknowledgment: Andriy Sherehiy)

5.1.2.5.2 Temperature Drift Test

Temperature drift significantly affects the performance of the tactile sensor. For instance, during operation, due to human touch, the sensor's temperature might increase. Thus, temperature drift compensation is critical for the efficient operation of the tactile sensor, for that purpose, we have conducted measurements to determine the sensor's resistance depending on the temperature. Temperature measurements with the tactile sensor were performed with the help of the Linkam Scientific Instruments® Analysa-LTS350 temperature chamber shown in Fig. 5.21, Resistance measurements were

performed in the chamber with a temperature range from 20°C to 100°C, and results are presented in Fig. 5.26. It is evident that resistance depends on the temperature is linear (R^2 = 1), which is consistent with the behavior of the bulk metal. There is also no evidence of effects associated with the heating of the Kapton substrate. Therefore, these results indicate that in this range of temperature (20°C to 100°C), the sensors can be reliably operated where temperature compensation can be efficiently realized.

This combined-structure tactile sensor was designed to realize temperature compensation function when using the sensor in the applications. A Wheatstone half-bridge circuit was designed to measure the voltage output of one resistor of two in-series connection resistors using the voltage divider method, which was mentioned in Section 5.1.2.2.1. As we know, the resistance of metallic structure will be changed depending on the surrounding temperature T and the strain Ɛ on it. Thus, the output voltage can be formulated as

$$V_{out} = \frac{R_2(\varepsilon,T)V_{in}}{R_1(\varepsilon,T)+R_2(\varepsilon,T)} \tag{5.18}$$

Thermal stimuli causes the variations in the output voltage that are [38]:

$$\frac{dV_{out}}{dT} = \frac{\partial V_{out} dR_2}{\partial R_2 dT} + \frac{\partial V_{out} dR_1}{\partial R_1 dT} \tag{5.19}$$

$$\frac{dV_{out}}{dT} = -\frac{R_2 V_{in}}{(R_1+R_2)^2}\frac{dR_1}{dT} + \frac{R_1 V_{in}}{(R_1+R_2)^2}\frac{dR_2}{dT} \tag{5.19}$$

$$\frac{dV_{out}}{dT} = \frac{V_{in}}{(R_1+R_2)^2}\left(R_1\frac{dR_2}{dT} - R_2\frac{dR_1}{dT}\right) \tag{5.20}$$

As temperature fluctuations produce a similar response in both structures, because of the almost same slopes of the resistances' changes during the increasing temperature. The equation (5.20) approaches zero, which means V_{out} is invariable to the thermal effects. In this theory, the combined-structure tactile sensor can realize the temperature compensation functions with the changes in the surrounding temperature.

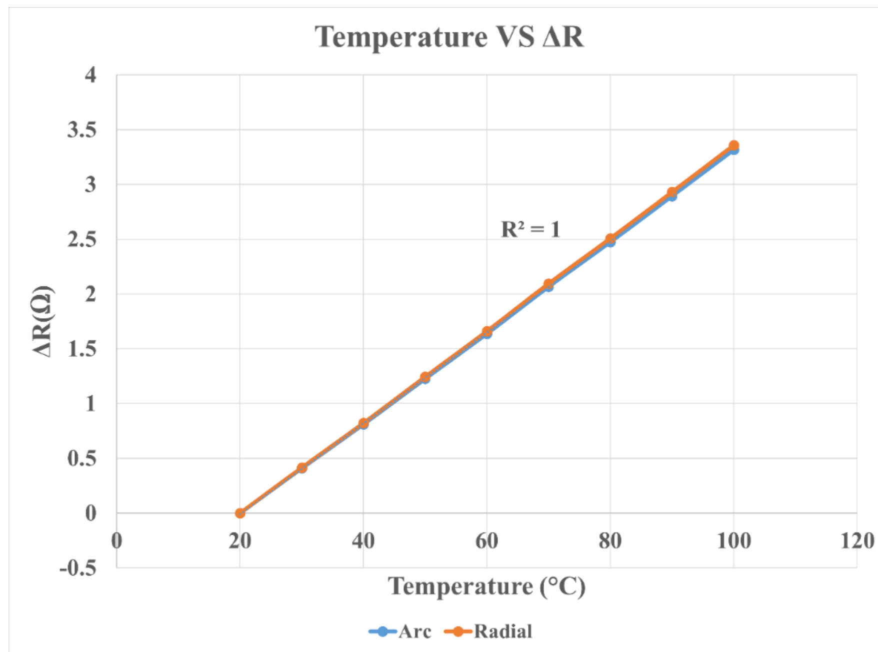

Figure 5. 26 Temperature performance of the radial and arc structures.

5.1.2.5.3 Single Sub-indenter Test

In the single sub-indenter test, a single force (1N, and 2N) was applied separately to the center of the tactile sensor. The changes of the resistance ΔR and the sensitivities ΔR/R of the radial structure and arc structure are presented in Fig. 5.27. Otherwise, when a ladder force, 0-0.5-1-1.5-2N, was applied to the tactile sensor gradually, the changes in the resistance (ΔR) of the radial and arc structure are depicted in Fig. 5.28. The responses of the radial and arc structure of the tactile sensor are symmetrical with respect to the time axis closely following the profile of the increasing and decreasing loads in Fig. 5.29. It was

observed that the dependence of the sensitivity on applied force is almost linear for both individual structures under almost 4N force which has similar approaches compared with the COMSOL® simulated results in Fig. 5.19. On the other hand, experimental trials have revealed that the level of response is higher for the radial structure rather than for the arc structure which disagrees with the simulated results. For the load of 2N experimentally determined sensitivity for the radial structure is 0.15% and for arc structure 0.1% in Fig. 5.29. This disagreement is most likely due to the idealization of the COMSOL model with respect to the simplification of the elastic properties of the sensor's Kapton® substrate and neglecting behavior of the Aerosol Jet printer printed metallic paths during mechanical deformation possibly different when compared to bulk silver.

Also, in Fig.5.29, the force is gradually increased from 0N to 5.5N with a step of 0.25N. When the force is over 4N, the response of the arc structure seems constant, even the radial structure still has a linear response. Therefore, it can be concluded the max force for the tactile sensor is 4N. When the force is between 0 to 4N, the sensor can keep stable and repeatable force responses of the radial and arc structures. Due to the linear relationship between applied force and the sensitivity of the sensor, the resolution of the force can be so small (such as 0.25N), but for better sensor performance, the applied force should be controlled under 4N.

Compared with the simulation result of the responses of the radial structure and the arc structure in Fig. 5.19, which has some discrepancies from the experimental results as depicted in Fig. 5.29. In the simulated plots of the two structures, the slope of the arc structure is greater than the radial structure; while in the experimental plot, the slope of the radial structure is greater than the arc structure. The discrepancies probably come from the

thickness of the Kapton, the variations of the thickness of your prints at different locations, the width variation of your printed feature size, and maybe the boundary conditions of the Kapton over the silicone.

In the simulation environment, it can help people to study the trend of change, rather than an exact replica of experiments because many physical aspects are unknown, but some assumptions are in the simulation. For example, the stiffness (Young's moduli) of the silicone bedding affects the magnitude of sensor sensitivity, but the actual value is unknown as well. Also, the contact or friction between the bedding and the polyimide sheet is unknown that is difficult to measure.

But in the simulation environment, it needs to assume they are fully attached which may affect the bedding deformation. Otherwise, bulk silver was used in the simulation but cured silver nanoparticles were used to print the structures. The curing process bonds the nanoparticles thus the silver lines are conductive. However, the curing process may not fully restore the crystal structure of the bulk silver metal, which would influence sensitivity as well. During the curing process, the solvent in the silver nanoparticles ink was removed or evaporated, which may cause surface tension of the polyimide sheet that may induce residue stress on the substrate. The probabilities above may result in the discrepancies between simulation results and experimental results.

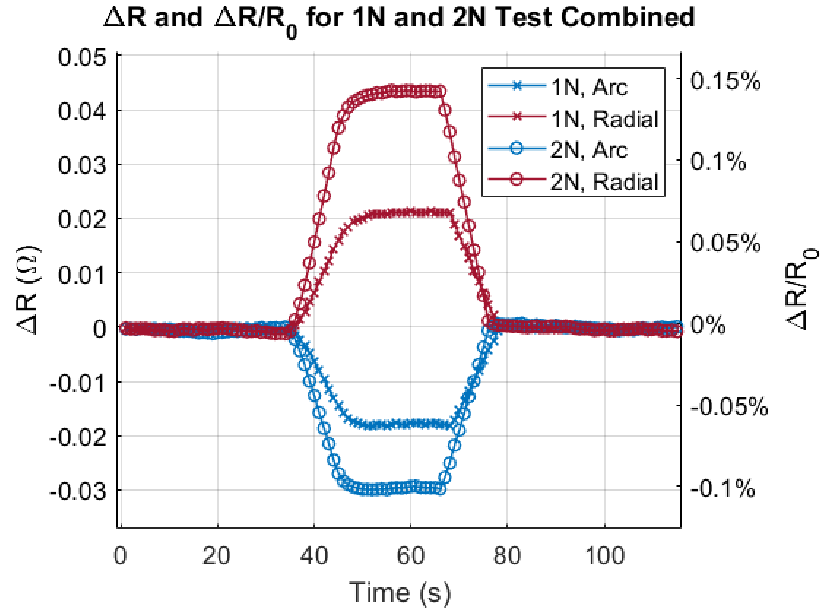

Figure 5. 27 The changes of resistance and the sensitivities of the radial structure and arc structure under the single force 1N and 2N. (Figure acknowledgment: Ruoshi Zhang)

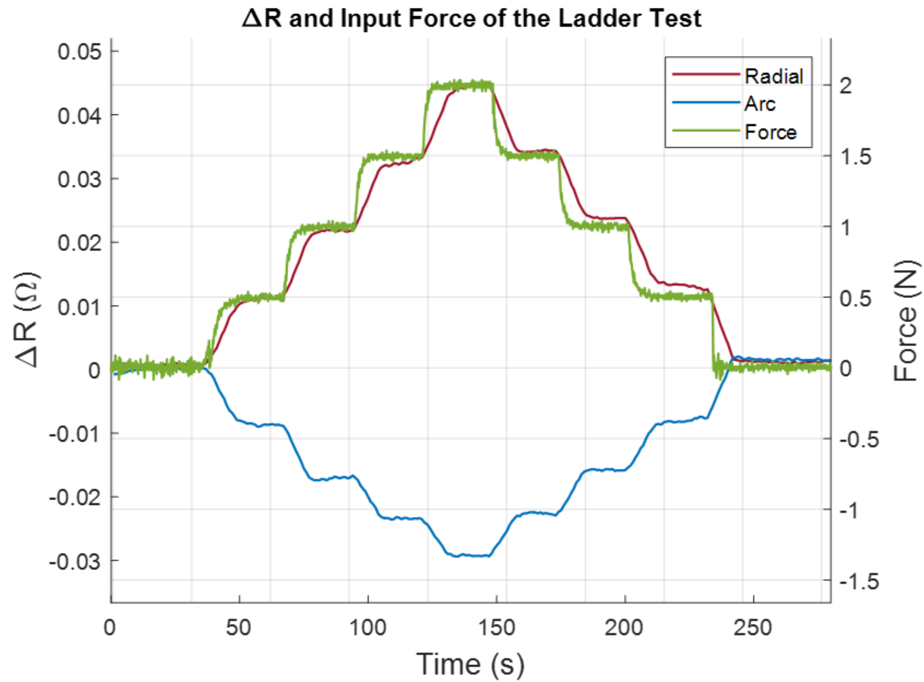

Figure 5. 28 The changes in the resistance of the radial and arc structures under the ladder force 0-0.5-1-1.5-2N. (Figure acknowledgment: Ruoshi Zhang)

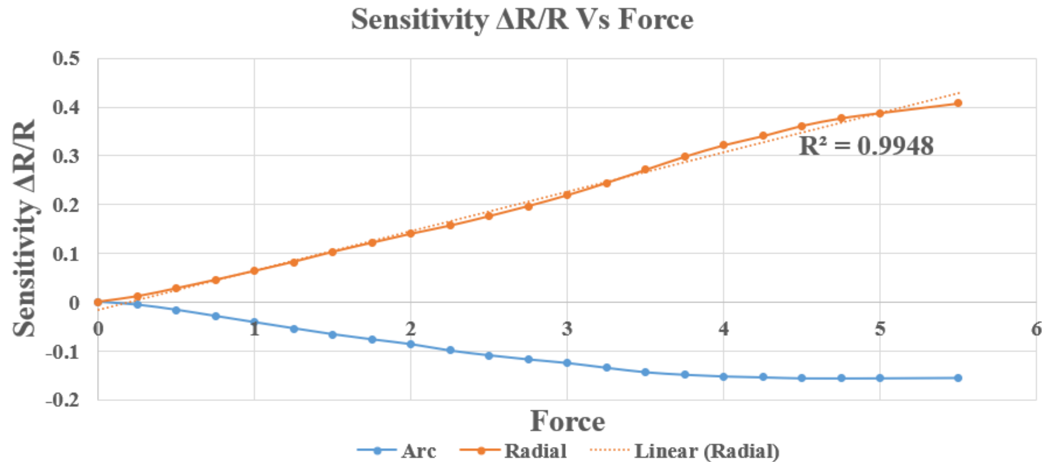

Figure 5. 29 The sensitivities of the radial and arc structures under the ladder force 0-5.5N with a step of 0.25N.

5.1.2.5.4 Multiple Sub-indenters Test

In the multiple sub-indenters tests, we propose the characterization of the tactile sensor's performance with respect to the different locations of the load relative to the geometry of the fabricated metallic structures on the substrate. We have conducted a series of the test for 5 locations of the sub-indenters in each of the 4 directions, 0°, 45°, 90°, and 135 as depicted in Fig. 5.30. The indenter was kept for 5 seconds with 2N on each sub-indenter location. The responses of the radial and arc structures are shown in Fig. 5.31. It is observed that for the 0° direction, there is a symmetrical response of the tactile sensor. When the load is applied on 0°-1 and 0°-5 sub-indenters, both resistances of the radial and arc structures are decreasing. However, when the load is on 0°-2 and 0°-4, only the resistance of the radial structure increases because the load is applied closer to the radial structure, as a result of performed domain response.

For the 45° and 135° directions, it is observed similar responses of the load. When the load is applied on 45°-1 and 135°-1, both resistances of the radial and arc structures only slightly decrease compared to the 0°-1 sub-indenter, most likely due to the contact

area of the sub-indenter on the FPC substrate in these locations. When the load is at 45°-4 and 135°-4, the resistance of the radial structure increases significantly because the load is applied to the external printed trace of the radial structure. When the load is applied on 45°-5 and 135°-5, both radial and arc structures have almost no responses. For the 90° direction, when the load is applied on 90°-4 and 90°-5, due to the load on the external trace of the arc structure, it is observed that a significant increase of the response is compared with the "4" and "5" sub-indenters' load response in other directions. As expected, when the load is applied on the "3" sub-indenter location, the response of the tactile sensor is almost identical for all the directions. Interestingly, for the sub-indenter location in directions 45°, 90°, and 135°, we have not observed a detectable response for the arc structure, which indicates that in these locations a load of 2N deformation of the substrate is not sufficient to induce a significant change of resistance ΔR of the tactile sensor's arc geometry.

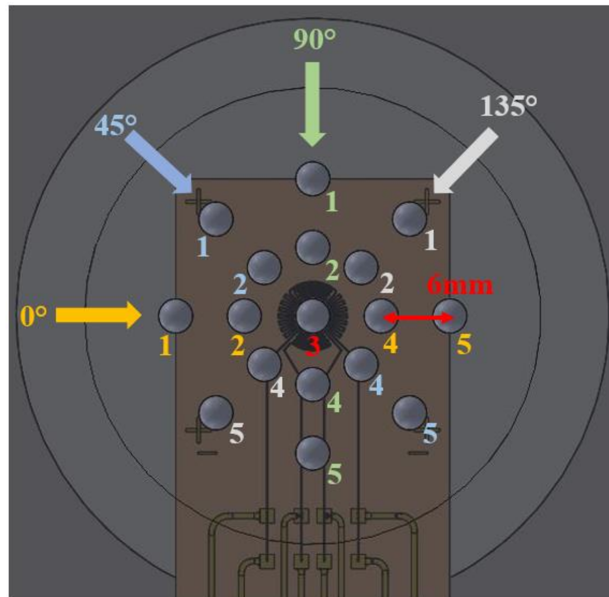

Figure 5. 30 Characterization of tactile sensor printed on the Kapton® substrate with indicated 5 different sub-indenter locations for 4 directions 0°, 45°, 90°, and 135°.

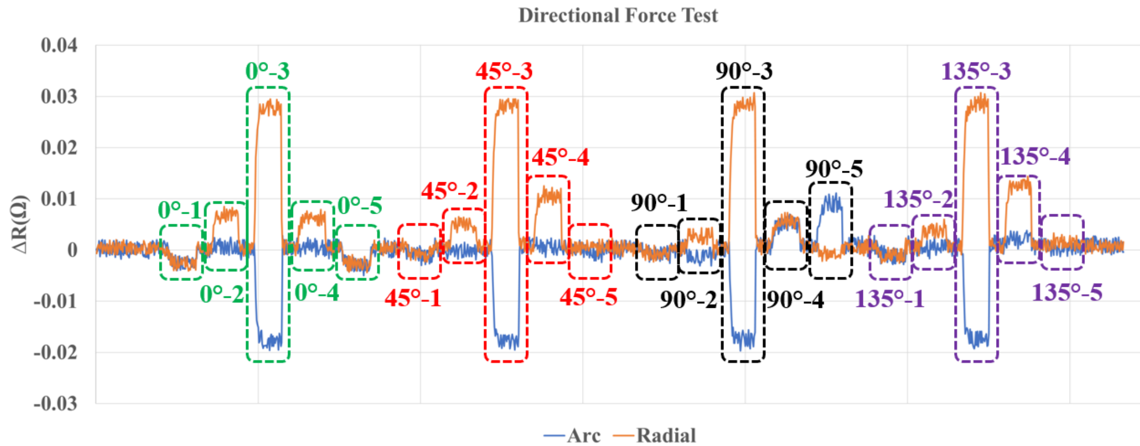

Figure 5. 31 Load responses of directional force test.

5.1.2.5.5 2x2 Sensor Array Test

For a large-scale tactile sensor force test, we expanded the single tactile sensor to a 2x2 tactile sensor array. In Fig. 5.32, a specific substrate was designed to measure 8 individual resistances (4 sensors) via a 4-wire measurement method. A 7x7 sub-indenters PDMS cover was made to test the responses of 4 tactile sensors when the 4N force on each sub-indenter location. In Fig. 5.33, when the force was only applied on Line 1(L1), L7, Column 1(C1), or C7, there was no response of the force on each of the sensors because the applied force is far away from the sensing area of the sensors. However, when the force was applied on L2 or L6 from left to right, the sensor 1(S1) and S3 or S2 and S4 started to have certain responses. For instance, the force was on L2C3 (6mm away from the center of S1), and the radial structure and arc structure of S1 has responses, whose resistances were increasing. Here, the resistance of the arc structure was increasing because the force on the side of the sensor was to pull the arc structure longer which cause the resistance increased. In contrast, when the force was on L3C2, the resistance of the arc structure of S1 was decreasing because the force was on the axis which makes the resistance of the arc structure decrease. When the force was applied on L3C3, L5C3, L3C5, or L5C5, the S1,

S2, S3 or S4 has the max responses of the force, meanwhile, when the force on each above location, only the corresponding sensor has the response, other sensors have no responses because the force is far away from other sensors (12mm away). Thus, the spatial distance range is at least 6mm based on the sensor and sub-indenter distributions. When the force passed through L4 from left to right, the responses of the 4 sensors are the combination of the responses when the force passed through L2 and L6 from left to right.

Figure 5.33 depicts the single sensor's sensitivity responses of the radial and arc structures when the force comes from the x-axis, y-axis, and two diagonal directions. Those responses are demonstrated as a Gaussian distribution. Furthermore, 3D Gaussian figures were generated (in Figure 5.34) to show the 2x2 sensor array sensitivity's response in spatial. According to the feedback of the 4 sensors' radial and arc structure sensitivities' change, it can be determined where the force is applied on the PDMS cover, which clearly indicates the force locations and strengths.

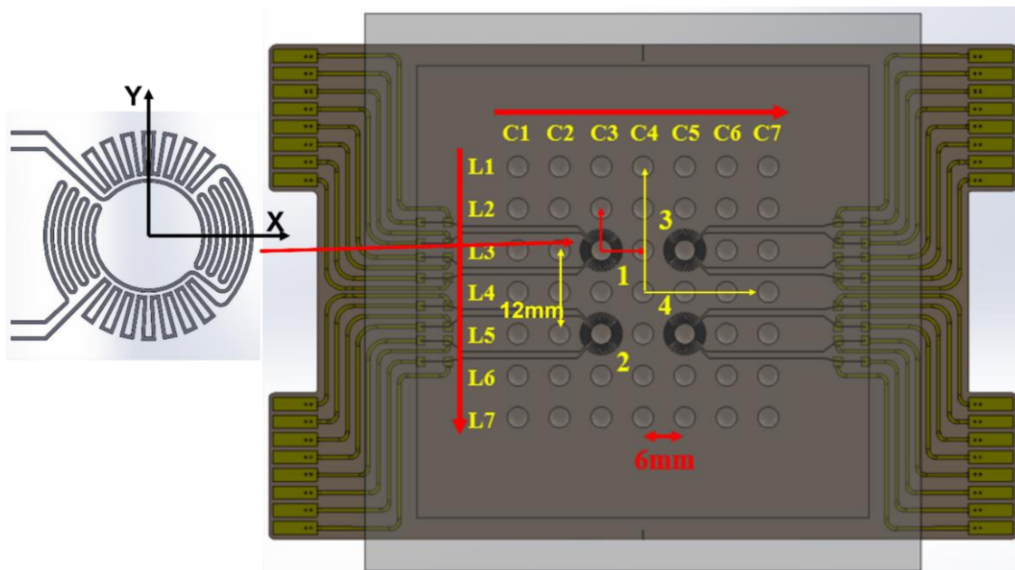

Figure 5. 32 2x2 sensor array with 7x7 sub-indenters PDMS cover.

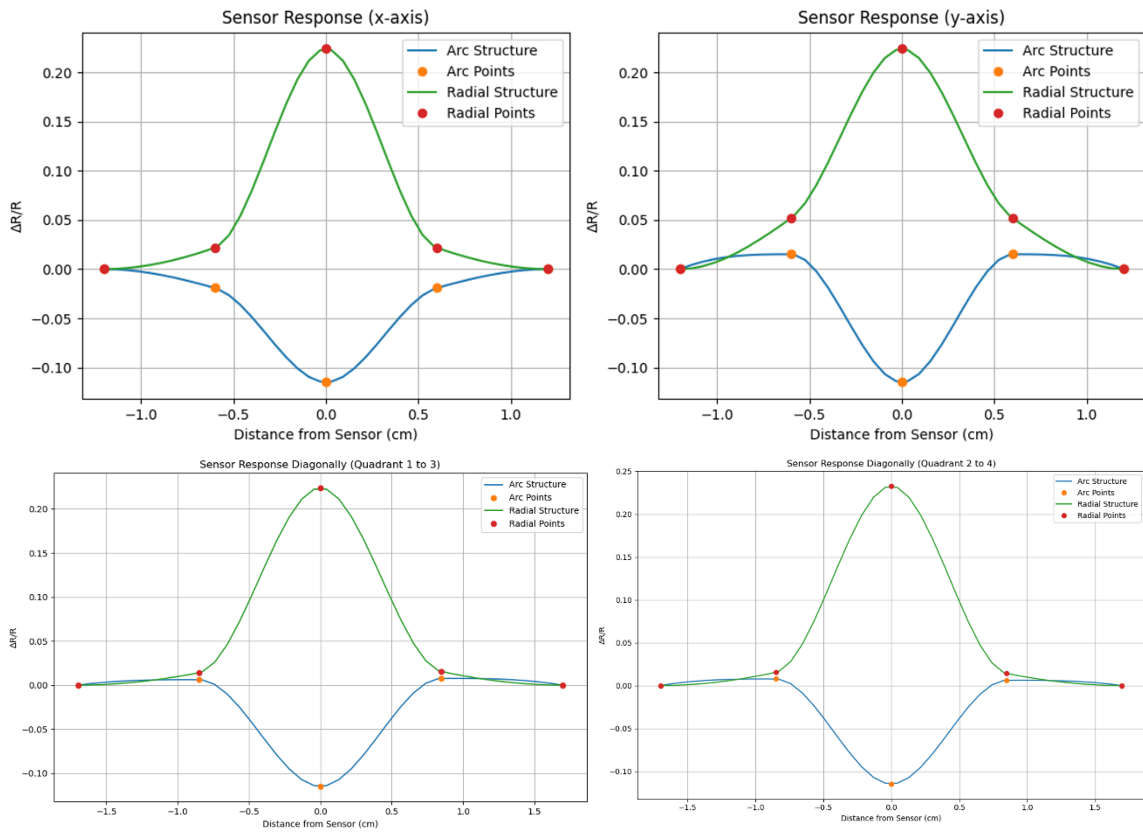

Figure 5. 33 The single sensor sensitivity's responses of the radial and arc structures when the load comes from different directions. (Figure acknowledgment: Jordan Dowdy)

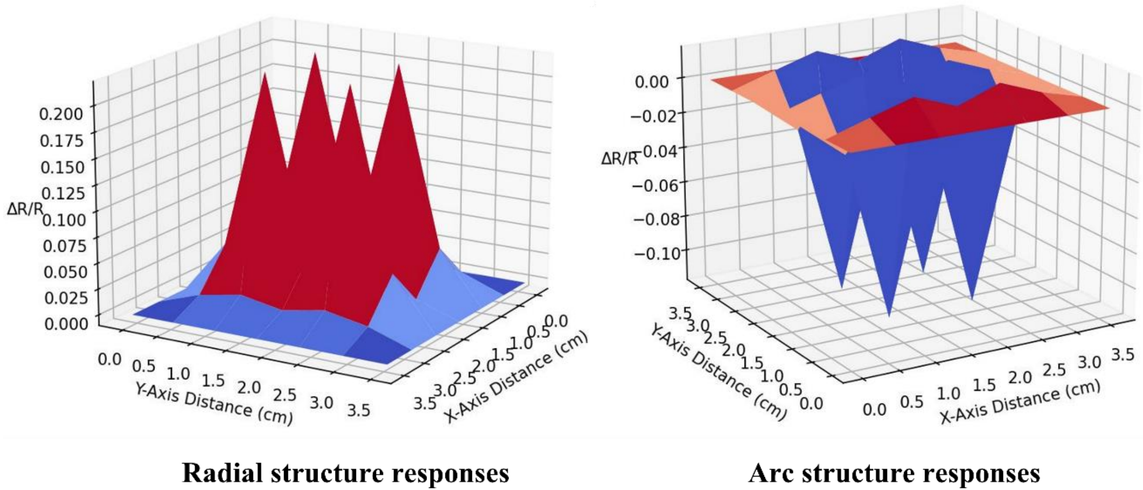

Figure 5. 34 The Gaussian distribution of sensitivity's responses of the radial and arc structure in a 2x2 sensor array. (Figure acknowledgment: Jordan Dowdy)

5.2 Electronic Textiles Fabrication

Because conventional fiber assemblies are irregular in nature and are subject to distortion, stretching, and shrinking, it makes the process of identifying functional fiber crossings a laborious task. To keep the fabric structures and fiber crossings at constant features and locations, we fixed the fabric structures with a 3D printed frame for the 1st generation deterministic alignment process of fabric structures with a MEMS gripper [68]. In this 1st generation alignment process, three manual linear stages, two motorized linear stages, and one motorized rotation stage were set up for hardware to complete the alignment process. However, the 3D-printed frame was not rigid enough, it had some deformations when it was clamped. Also, the level of the frame was adjusted by manual operation. It was not very precise and repeatable. In addition, because the stages had a limited travel range, the human operator had to adjust the camera to reach different MEMS clamps locations to check the alignment results, which resulted in more uncertainties in the alignment process. Due to the above disadvantages of the 1st generation alignment process, we developed a 2nd generation alignment process with a multi-robot collaboration including two industrial robotic arms and one custom high-resolution positioner integrated with multiple functions, these functions include a robotic tool change process, visual servoing, target detecting, and UV curable adhesive printing. Also, a metal frame was made to clamp the fabric substrate to secure fibers deterministically and ensure dimensional stability. A corresponding sample chuck was designed to carry a 4-inch wafer placed on the custom positioner. Metalized MEMS clamps fabricated on the 4-inch wafer were to contact conductive fibers toward electronic integration of MEMS with E-textile. The reason to use

MEMS clamps rather than adhesives to fix the fabric intersections is due to the desire to not interfere with the surface micromachining release process.

5.2.1 Electronic Textiles Design

To fabricate the electronic textile, a novel process was developed to integrate fabric material with MEMS clamps. The fabrication process is described below:

- **Create a fabric sample:** The fabric mesh design consists of 500 to 1000 microns thick non-conductive base fibers arranged in a grid format with an inter-fiber spacing of 4mm. The design has two 400 to 800 microns thick non-touching parallel conductive fibers which follow a serpentine course along the intersections of the base mesh grid, such that an angle of 45 degrees is formed between the base fiber and the conductive fiber at their intersections. After the fabric mesh was weaved, it was stretched to keep the fabric surface flat by a stretcher device, then a designated pair of metal frames was employed to clamp the fabric mesh by magnetic force. The fabric sample was ready for the next fabrication process after cutting the unnecessary material surrounding the metal frame.
- **Identify the intersections in the fabric:** A binary image processing algorithm was employed in MATLAB® based on the high-resolution image of the framed fabric to identify the intersections in the fabric. The binary image processing algorithm routine converts the fiber matrix image into a binary form (white and black pixels from thread and background, respectively) using the "imbinarize" function that implements Otsu's threshold method through an intermediary grayscale conversion. The size of the binary image matrix determines the frequency of a subroutine wherein, which is specific to the case of the test sample, the element position of each

white pixel surrounded by relatively diagonal white pixels and relatively vertical and horizontal black pixels within the range of the pixel distance between consecutive fiber intersections is stored in a 2-D matrix, and it is identified to contain the coordinates of the fiber intersections. Since a number of pixels are presented at each fiber crossing, the fiber intersections get identified as a group of white pixels. Therefore, the consecutive sub-routine determines the mean of the group of points at each intersection such that each fiber crossing is represented by a single pixel point which is plotted on the image of the test sample as shown in Fig. 5.36(a). The algorithm was implemented on the smaller quadrant parts of the image versus taking the entire image as input. The MATLAB® routine then takes in the intersection coordinates (X, Y) to place the clamp shaped '+' at each intersection location. The length, rotation, and distribution of the clamps are determined by a clamp collision detection subroutine that identifies the overlapping or colliding clamps and colors them in red, while the green clamps are the ones that are free of collision. In Fig. 5.35, the length of the finger of the clamp increases, and the percentage of overlap or collision of the clamps increase. The maximum length of the finger is 2500µm without any overlap or collision between the clamps as shown in Table 5.7. Thus, the length of actual MEMS clamp fingers is designed with 2500 µm as shown in Fig. 5.35(d).

Sometimes the fiber distortions and imperfect fiber paths can affect this pixel neighborhood distribution which might not match the predefined intersection pattern within the tolerance range as shown in Fig. 5.35(e). This results in false negatives

and false positives affecting the efficiency and accuracy of the algorithm. For the test sample, the efficiency of fiber intersection identification can reach up to 97.8%.

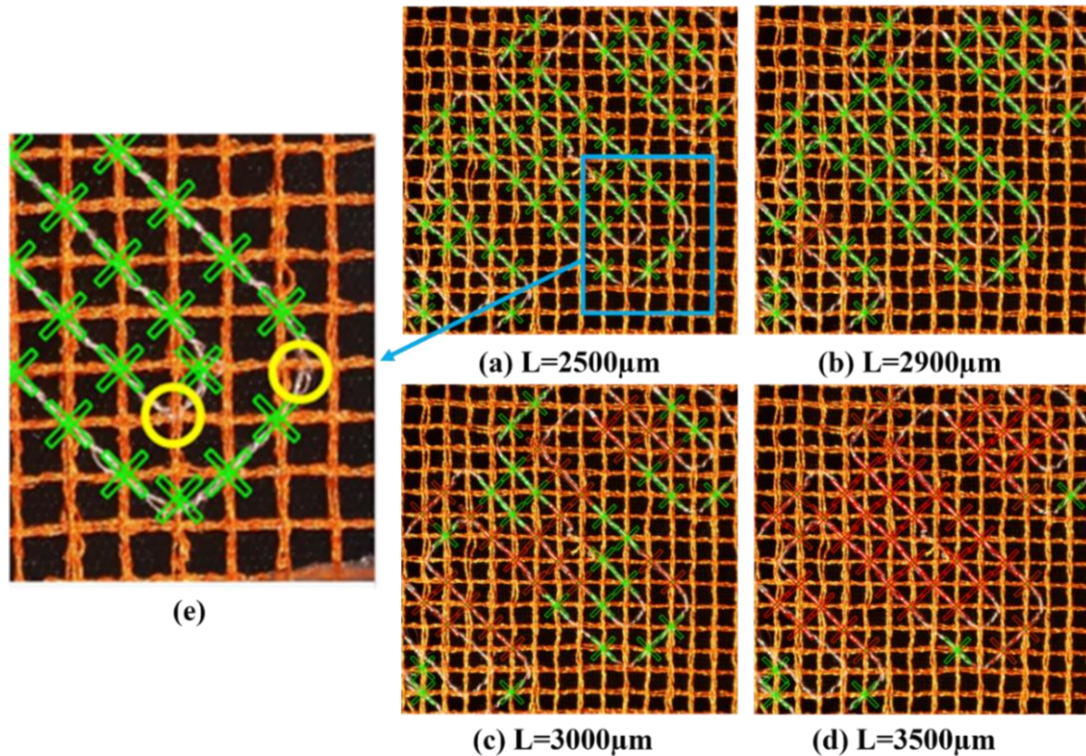

Figure 5. 35 Red crosses mean MEMS clamps overlap or collide; green crosses mean MEMS clamps without overlap or collision; (e) Missed electrical intersections at fiber distorted turnings circled in yellow. (Figure acknowledgment: Sushmita Challa)

Table 5. 7 length of MEMS clamp finger and corresponding percentage of overlap or collision of Mems clamps.

Length of MEMS clamp finger	**Percentage of overlap or collision**
2500 µm	0%
2900 µm	4%
3000 µm	52%
3500 µm	90%

- **Design a MEMS clamps layout in Fig. 5.36(c):** The MEMS layout design specific to the framed fabric was created in L-edit layout software according to the identified intersections in the fabric. The 12-finger clamp design in Fig. 5.36(d) consists of T-shaped traces which are aimed to clasp the conductive fibers toward making electrical contact, while the L-Shaped clamp arms clasp the base fiber intersections for mechanical support. The trace lengths are chosen such that reliable scope of the clasp is obtained which further depends on the radius of curvature of the clamp and fiber feature. Otherwise, a specific alignment mark in Fig. 5.36(f) was added in the MEMS layout to be the specific target in the deterministic alignment process with the visual servoing function.

- **Fabricate MEMS clamps in the cleanroom:** After the MEMS clamps layout was generated and corresponding masks were printed for fabricating MEMS clamps in the cleanroom using MEMS fabrication techniques. The whole fabrication process of MEMS clamps will be described in the next section.

- **Align the MEMS wafer with the framed fabric:** Instead of using the hardware in the 1st generation alignment process [68], a multi-robot collaboration technique was developed and implemented to complete the 2nd generation deterministic alignment process, which will be detailed in the next sections.

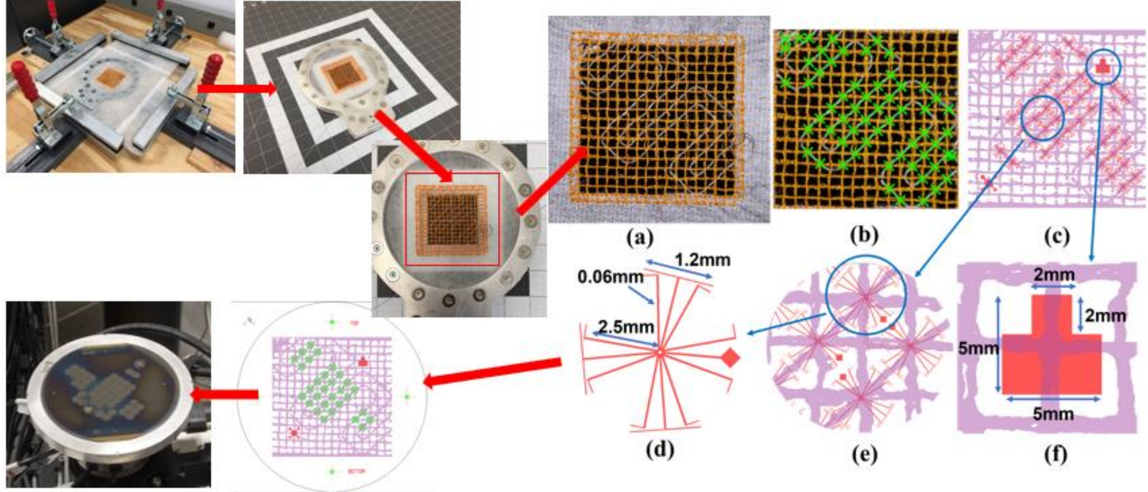

Figure 5. 36 (a) The image of the fabric structure. (b) (c) MEMS gripper and alignment mark distribution for mask design. (d) Single MEMS gripper structure dimension. (e) MEMS grippers align on the intersections of the fabric. (f) Alignment mark dimension.

5.2.2 Simulation of the Grasp Tolerance of MEMS Clamp

Based on the MEMS clamp dimension in Fig. 5.36(d), the length of the finger is 2500µm and the diameter of the fiber is defined as 600µm. The grasp tolerance range of the MEMS clamp was simulated in the COMSOL® finite element analysis (FEA) software. The curvature of the pop-up finger was simulated based on the Timoshenko formula [69]. The curvature's radius of the bi-metallic strip is given by:

$$\rho = \frac{h\left[3(1+m)^2+(1+mn)\left(m^2+\frac{1}{mn}\right)\right]}{6(\alpha_2-\alpha_1)(t-t_0)(1+m)^2} \tag{5.18}$$

Where ρ is the radius of curvature of the strip; α_1 and α_2 are the coefficient of expansion of the two metals respectively; $t - t_0$ are the change of temperature for uniformly heating two metals to be welded together, the bi-metallic strip will be bending during heating if the coefficient of linear expansion of two metals are different; h is the total thickness of the bi-metallic strip; m is a_1/a_2 the ratio of the thickness of each metal layer; n is E_1/E_2 the

ratio of elastic modulus or Young's modulus of each layer. In our sample, the upper metal layer a_1 (Ti and Au) and lower SiO_2 layer a_2 are treated as the bi-metallic strip.

Fig. 5.37 depicts the 2500μm length MEMS finger bending in a half circle, whose highest point reaches around 1592.35μm, and a 600μm diameter fiber. Due to the extra fabric material on the edges, the wafer was moved up to reach the bottom of the fabric textiles, the edges of the textiles will touch the wafer first, which results in an approximate 600μm distance between the center of the fiber and the surface of the MEMS clamps. In Fig. 5.37, to grasp the fiber efficiently, the maximum height that the center of the fiber can reach is around 1300μm, while the maximum distance in the x-axis that the center of the fiber can reach is about 2100μm at 600μm height, the MEMS finger can grasp the fiber stably.

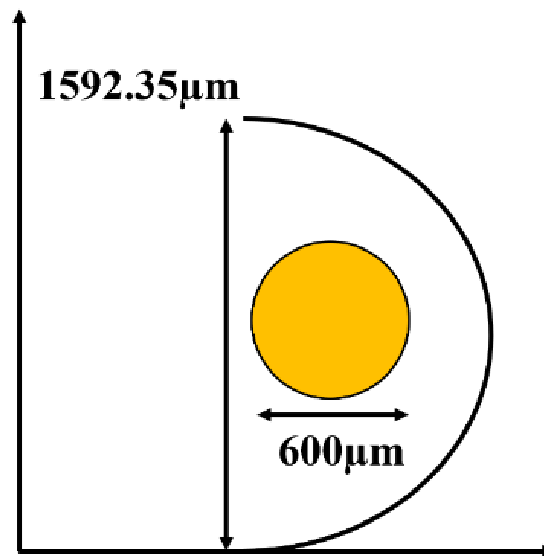

Figure 5. 37 2500μm length MEMS finger bends in half circle and a 600μm diameter fiber.

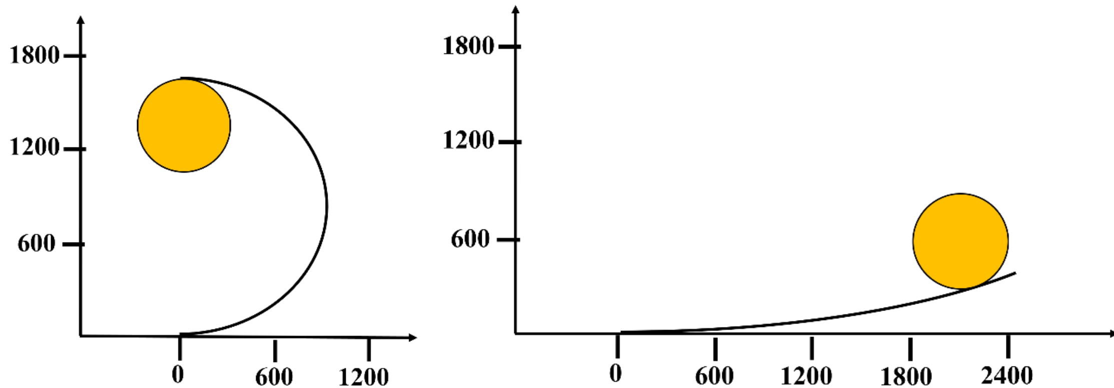

Figure 5. 38 left: the fiber reaches the maximum y-height for grasping; right: the fiber reaches the maximum x-axis for grasping.

5.2.3 Fabrication Process of Electronic Textiles

5.2.3.1 MEMS Clamps Fabrication Process

After identifying intersections of the non-conductive and conductive fibers, the designed 12-finger MEMS clamps were placed in the corresponding locations in the layout design. Then corresponding masks were printed to fabricate the MEMS clamps on the 4-inch Silicon wafer. The fabrication process of MEMS clamps in detail is described below and a simple demonstration of the MEMS fingers fabrication process is shown in Fig. 5.39:

1. A pure polished 4-inch Silicon wafer was thermally oxidized to generate an approximate 560nm thick SiO_2 layer.

2. A mask was used for the first photolithography process to generate the MEMS clamps pattern windows before sputtering metal layers on them. In order to make the metal lift-off process more efficient, an image reversal process was applied for the MEMS clamps pattern windows generation.

3. A PVD75 was used to sputter two different metal layers on the SiO_2 layer: Titanium (Ti) and Gold (Au). The total thickness of the metal layers is around 470nm.

4. After sputtering the metal layers, the lift-off process with the ultrasonic assist removes unnecessary metal material. When the lift-off process was done successfully, only the MEMS clamps pattern was left on the SiO_2 layer.

5. The second photolithography process with the second mask was completed to generate the windows around MEMS clamps for etching the SiO_2 layer to expose the underneath Si layer.

6. A Trion instrument was used to etch an approximate 560nm thick SiO_2 layer around MEMS clamps. The 1827 photoresist was coated to protect the metal layer during SiO_2 etching.

7. After designated areas of SiO_2 etching, the underneath Si was exposed. However, before etching the Si isotropically to pop up the MEMS clamps, a deterministic alignment process for the fabric sample and MEMS clamps needs to be completed.

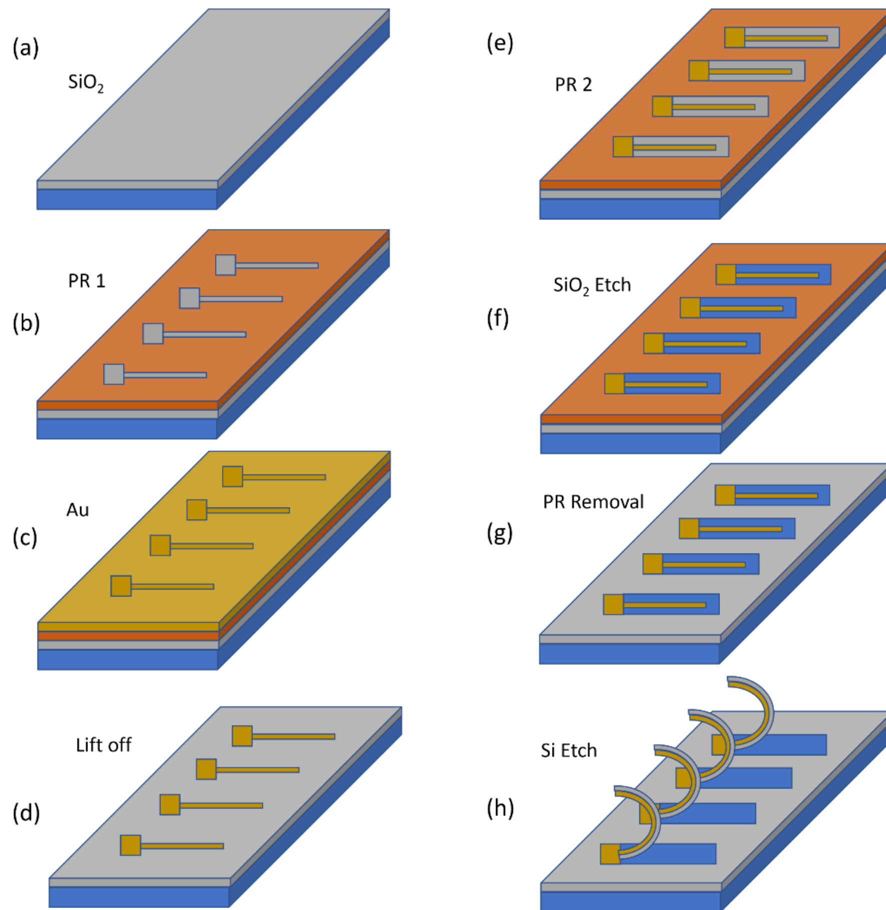

Figure 5. 39 A simple demonstration for the MEMS fingers fabrication process.(a)Si wafter with SiO_2 layer; (b)Photolithography for MEMS finger pattern; (c) Sputter Au layer; (d) lift-off process; (e) Photolithography for SiO_2 etching pattern; (f) Etch SiO_2 around MEMS fingers;(h)Etch Si isotropically to pop up the MEMS fingers. (Figure acknowledgment: Sushmita Challa)

Compared with 1st generation hardware setup (shown in Figure 5.40), due to its disadvantages, for example, the 3D printed frame fixed the fiber textile structures was not rigid enough, it was easy to deform during clamping. Also, the stages had a very limited travel range for large-scale samples. The vertical camera had to be adjusted manually to locate the desired positions, which was not convenient for operators.

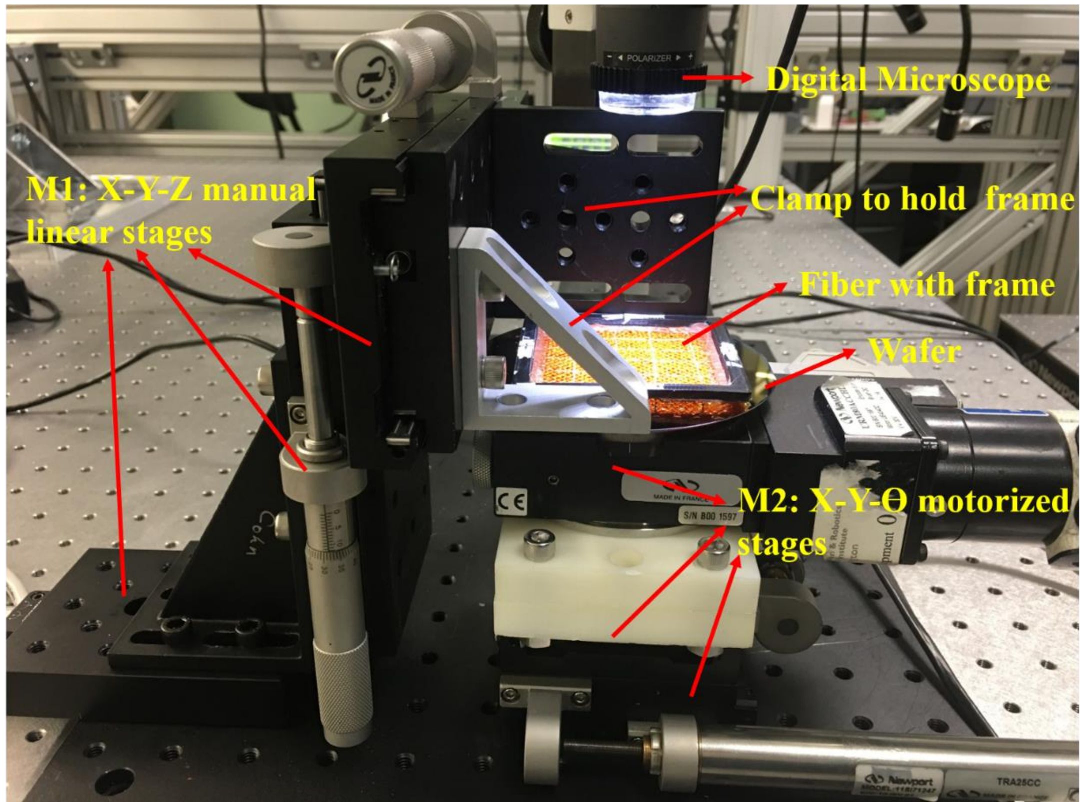

Figure 5. 40 1st generation hardware for deterministic alignment process of textiles with MEMS grippers

For deterministic alignment of fabric structure with MEMS clamps, we employed three different robots in the NeXus: the 6-DOF robotic arm, the 4-DOF robotic arm, and the 6-DOF positioner as well as different tools, like HIWIN XEG-32 electrical gripper (HIWIN Corporation, IL, USA) and Nordson EFD794 Auger Valve (Nordson Corporation, OH, USA), on the tool change station. Each robot has specific functions for the deterministic alignment process.

- **6-DOF robotic arm:** it is an industrial robot DENSO VS-6577B (DENSO Corporation, CA, USA), which was ceiling mounted on a large X-Y gantry (Macron Dynamics, Inc., PA, USA) with a 2800mm x 2250mm (X x Y) travel range to maximize the workspace of the 6-DOF robotic arm in the NeXus system. The 6-DOF robotic arm is

responsible for picking up the HIWIN electrical gripper on the tool change station to grasp the metal frame clamping the fabric structure in Fig. 5.41 (a).

- **4-DOF robotic arm:** it is another industrial robot DENSO HM-40A04M (DENSO Corporation, CA, USA), which was mounted on a robotic transport unit (RTU) (Macron Dynamics, Inc., PA, USA) with a 2300mm linear travel range. A Dino-lite camera AM73915MZTL (Dunwell Tech, Inc., CA, USA) was mounted on a 4-DOF robotic arm for detecting targets, like the intersection for the center of the alignment mark and the MEMS clamps to check the alignment results after visual servoing completion. With the feedback from the camera, the alignment mark can be fine-adjusted to match the corresponding intersection on the fabric. Also, the 4-DOF robotic arm needs to pick up the Auger Valve to dispense UV-curable adhesive on the fabric to make the wafer stick to the bottom of the fabric.

- **6-DOF positioner:** it is composed of a long coarse linear stage with 2500mm travel (IAI America, Chicago, IL, USA), two fine linear stages (Newport® M-ILS300LM-S), a Z stage (Newport® GTS70VCC), a tilt (T) stage (Newport® BGS80CC) and a rotation (R) stage (Newport® URS50BCC) (Newport® Corporation, CA, USA). Those six motorized stages built up an X-Y-X-Z-T-R, total 6 degrees of freedom, positioner. The 6-DOF positioner can be transferred to different stations along with the IAI stage for specific applications on the long optical table. A 4-inch wafer sample chuck in Fig. 5.41(b) was designed to couple the metal frame. It was fixed on the top of the 6-DOF positioner by the ATI QC-11 tool change coupler in Fig. 5.41(c) (ATI Industrial Automation, Inc., NC, USA). The wafer with the MEMS clamps was loaded on the sample chuck and attacked by a vacuum.

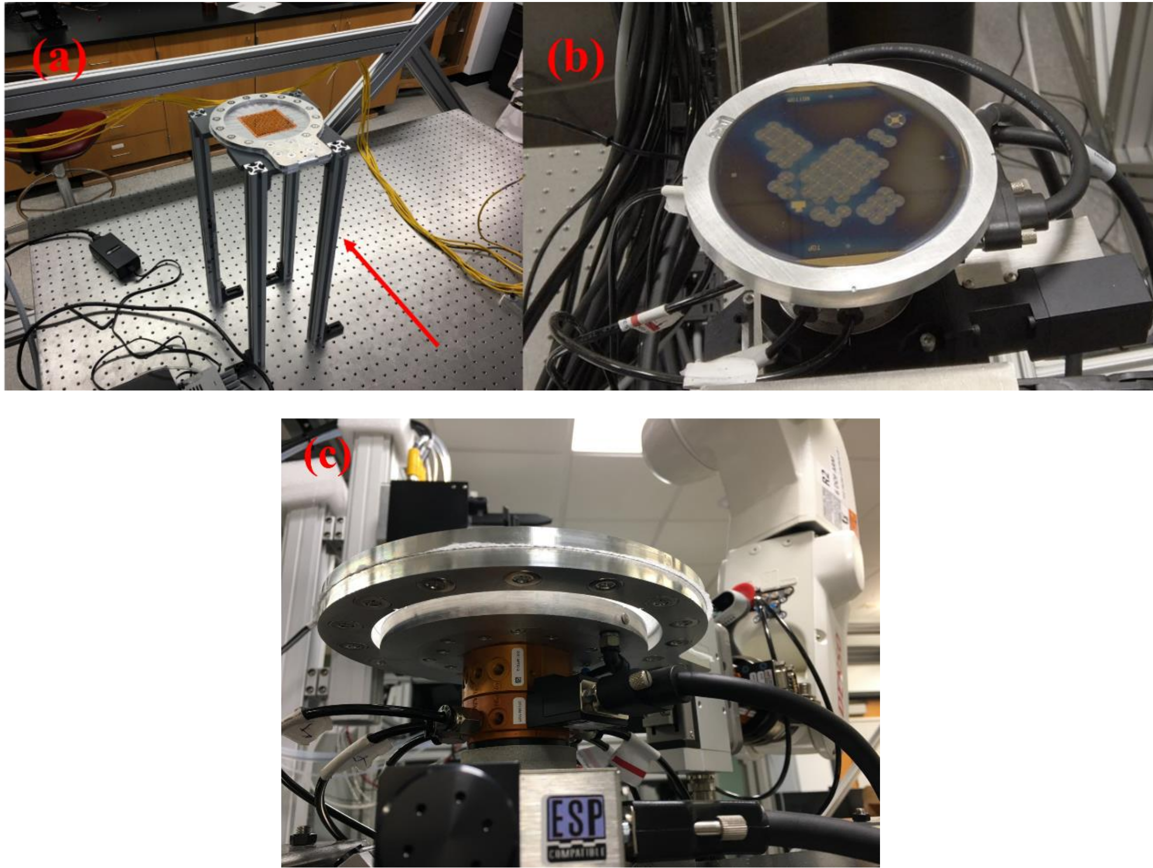

Figure 5. 41 Metal frame clamping fabric material on the standing; (b) 4-inch wafer sample chuck carrying the wafer with MEMS clamps; (c) Metal frame coupling with 4-inch wafer sample chuck.

5.2.3.2 Deterministic alignment process

The deterministic alignment of fabric structure with MEMS clamps is a process of three-robot collaboration depicted in Fig. 5.42 and implemented in Fig. 5.43. To carry out the process, a sequence of automated robot operation steps was formulated and implemented in our robot controller, including sample loading, robotic tool change process, visual servoing, and SU-8 photoresist dispensing. A complete description of these steps is listed below:

1. The 4-inch wafer sample chuck needs to be placed on the 6-DOF positioner, then needs to load the 4-inch wafer with the fabricated MEMS clamps on the chuck and turn on the vacuum to attack the wafer.
2. Load the frame that clamps the fabric material on the specific frame station in Fig. 5.41(a). The metal frame has two pieces of metal plate inserted with several magnets to clamp the fabric sample by magnetic force.
3. Initialize the 6-DOF positioner and then rotate the sample chuck in a 45-degree orientation. Then, initialize two robotic arms at the rest positions, respectively.
4. The 6-DOF robotic arm moves to the tool change station to pick up HIWIN electrical clamps by QC-11 tool change coupler and moves to grasp the fabric frame, then moves the frame above the 4-inch wafer sample chuck.
5. The 4-DOF robotic arm moves to the fabric frame and adjusts the Dino-lite camera above the fabric to focus on the intersection which is for the alignment mark on the wafer. The coordinate of the intersection can be acquired by the MEMS layout design. When the intersection is moved into the camera's field of view, the coordinates and orientation of the intersection can be recorded from the image of the camera.
6. Remove the fabric frame from the top of the wafer and adjust the height of the camera to focus on the alignment mark on the wafer. At this moment, the alignment mark should have some offsets due to errors in loading the wafer on the sample chuck and the frame on the frame station as well as the repeatability and accuracy of the 6-DOF robotic arm and the 6-DOF positioner.

7. Due to the offsets of the alignment mark on the wafer, the visual servoing function was implemented to fine-adjust the center of the alignment mark to match the coordinate and orientation of the intersection.

8. When the visual servoing process is completed, the metal frame is moved back to the previous position, thus the center of the alignment mark should match its corresponding intersection. In the vertical direction, the wafer is moved up by the Z stage of the 6-DOF positioner to gently touch the bottom of the fabric material.

9. Adjust the camera to check how MEMS clamps align their specific intersections referred to the coordinate of the center of each MEMS clamp acquired from the MEMS layout design. If the alignment results are not acceptable, repeat steps 6 to 8. Note that before repeating step 6, the wafer needs to move down back to the initial height to avoid crashes during removing the fabric frame from the top of the wafer.

10. Assuming that the alignment results are acceptable, the 4-DOF robotic arm moves to the tool change station to pick up the Auger valve and then moves back to the 6-DOF positioner and adjusts the nozzle above the fabric by about a 1mm distance.

11. Control the Auger valve to dispense SU-8 photoresist on the fabric edges following a square pattern with G-code commands.

12. Remove the Auger valve and place it back on the tool change station. Then turn on UV light to cure the SU-8 photoresist for at least 10 minutes.

13. Turn off the UV light and the vacuum of the sample chuck and move down the sample chuck. At this moment, the wafer should be stuck on the bottom of the fabric material with the cured SU-8 photoresist.
14. Move the fabric frame back to the frame station. Open the electrical gripper to release the frame. Then place the electrical gripper back in the tool change station. All three robots are reset to their initial positions.
15. Unload the fabric frame and open it to take out the fabric with the wafer. Cut off unnecessary material around the wafer, and the fabric with the wafer is ready for the release process.

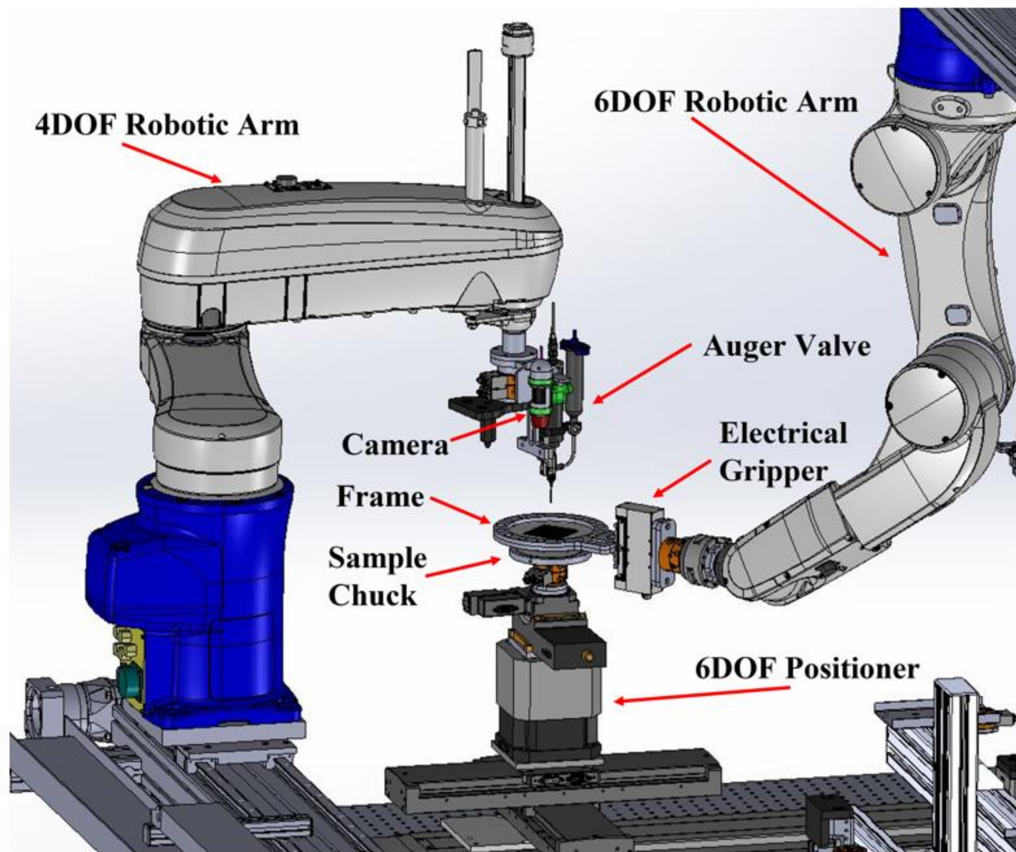

Figure 5. 42 Design of the NeXus system manipulators for fiber and MEMS clamps handling and alignment.

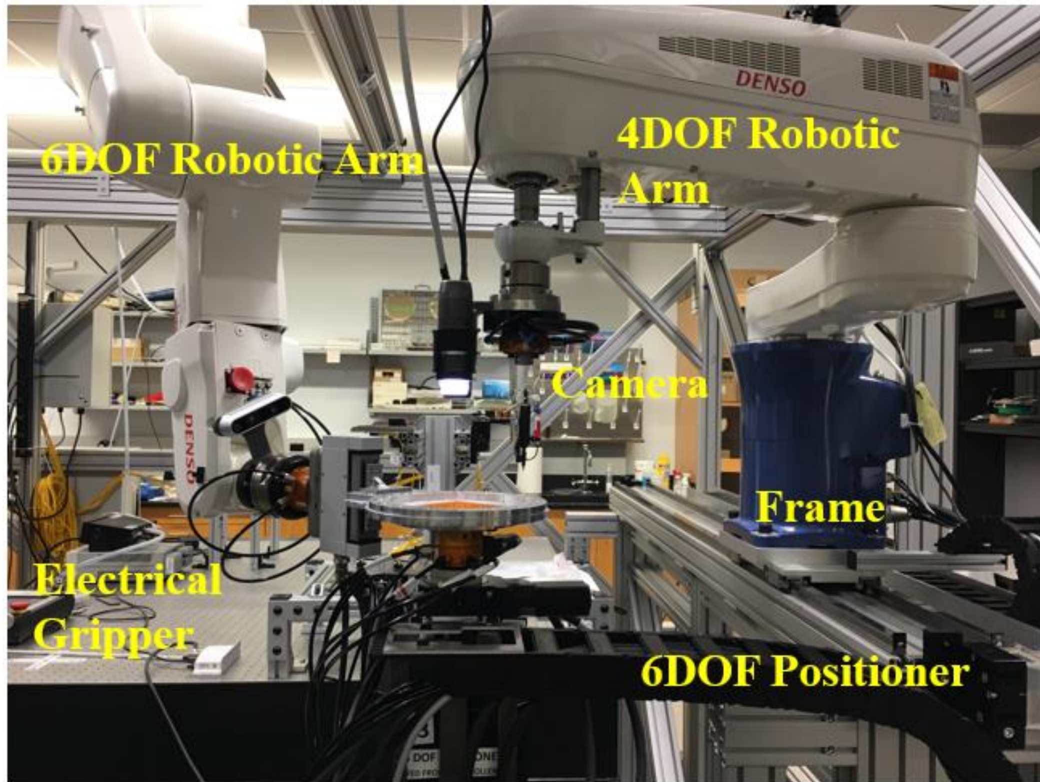

Figure 5. 43 An image of the NeXus system in our lab.

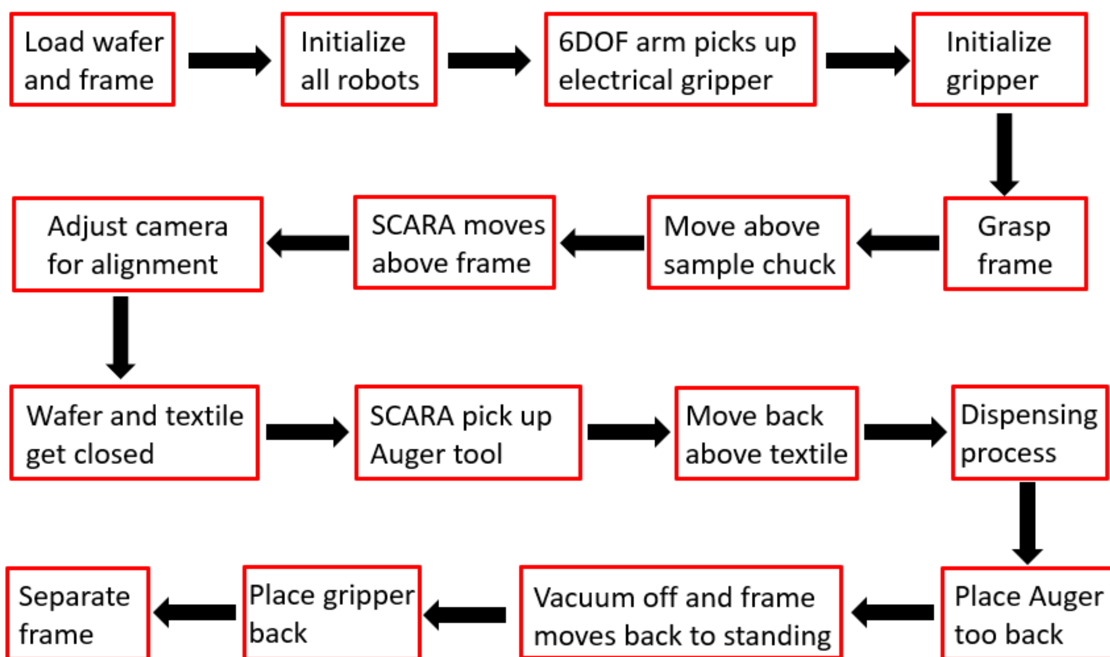

Figure 5. 44 Flow chart of the deterministic alignment process.

5.2.4 Experimental results

During the deterministic alignment process with the multi-robot collaboration, several significant functions were implemented, such as the robotic tool change process, visual servoing, target detecting, and SU-8 photoresist printing.

5.2.4.1 Robotic Tool Change Process

There are two tools on the tool changer station in NeXus employed in the alignment process, HIWIN electrical gripper and the Nordson Auger valve. The tools were picked up by the 6-DOF robotic arm and the 4-DOF robotic arm respectively using the ATI QC-11 tool change coupler. An electrical gripper was used for grasping the metal frame and holding it parallel to the 4-inch wafer sample chuck. The Auger valve was used for dispensing MICROCHEM® SU-8-50 photoresist (MicroChem Corporation) on the fabric material to stick it to the wafer after the alignment process. When the alignment process was done, both tools were placed back in the tool change station at their constant locations.

5.2.4.2 Visual Servoing and Target Detecting

With the visual feedback of the Dino-lite® camera on the 4-DOF robotic arm, targets, like the intersection for alignment and the MEMS clamps alignment results, can be detected and checked. Also, to improve the precision of alignment results, a visual servoing function was adopted to enhance the accuracy of the alignment between the fabric intersection and the alignment mark. In the visual servoing function, image Jacobian was employed to adjust the center of the alignment mark reaching its corresponding intersection on the fabric based on the coordinate and orientation of the intersection in the image. Equation (5.7), (5.8), and (5.9) [70] expresses how to calculate the motion of stages of the 6-DOF positioner to move the alignment mark to reach its corresponding intersection on

the fabric. Based on the vision feedback values, the alignment mark can move to the corresponding intersection in a fast and precise method by using the visual servoing technique in Fig. 5.45.

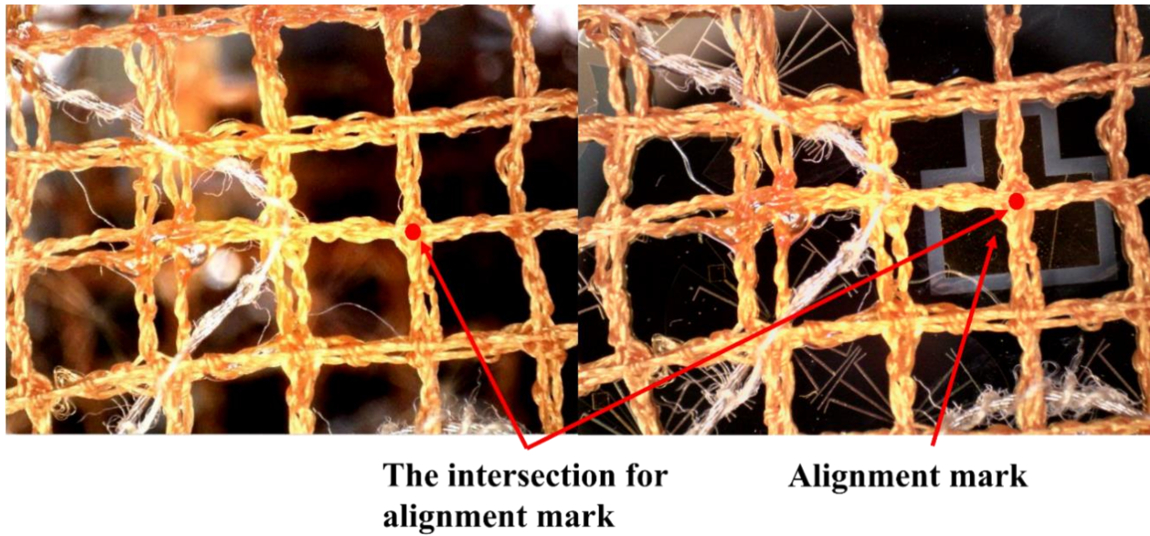

Figure 5. 45 The alignment mark aligns with the specific intersection after the visual servoing process.

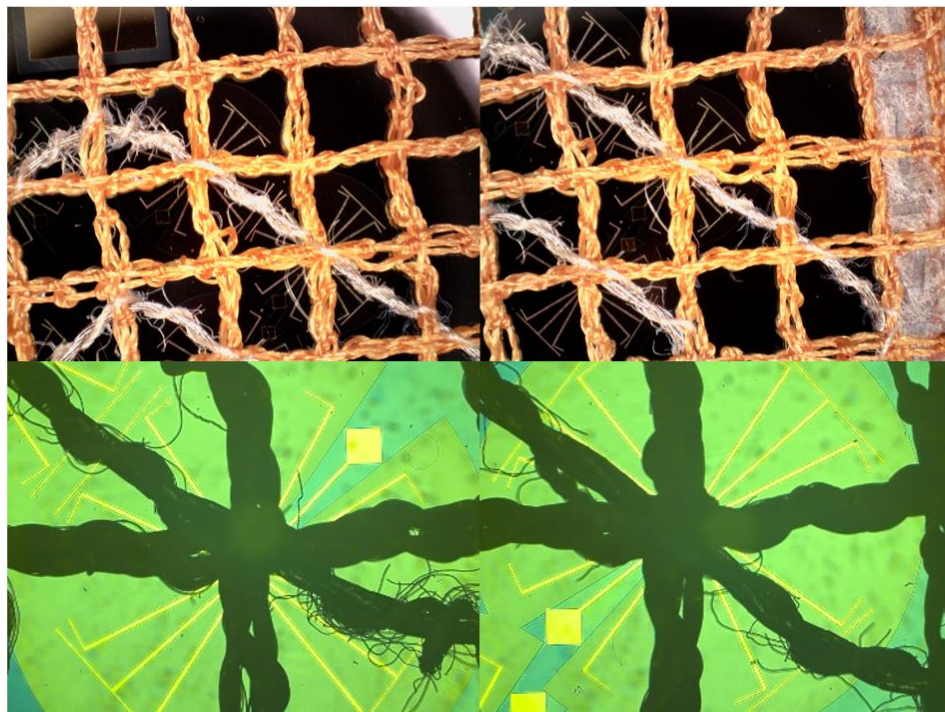

Figure 5. 46 Alignment results of MEMS grippers with fiber intersections.

After the alignment mark on the wafer was aligned with the intersection on the fabric, the Dino-lite® camera was controlled to check random MEMS clamps' alignment results. Fig. 5.46 depicts some MEMS clamps aligned with their corresponding intersections. Compared with the layout design of the mask for the MEMS clamps fabrication in Fig. 5.36, after the alignment process with the multi-robot collaboration in the NeXus, the center of each MEMS clamp was aligned with its corresponding intersection properly, during the visual servoing process, there are some buffers programmed in translational and rotational direction to adjust the target to move to the desired position and orientation. Those buffers resulted in +/- 20μm in translation and +/- 0.5° in rotation in Fig. 5.47. Moreover, considering adding 35μm of the repeatability of the 6-DOF robotic arm, the alignment errors are still under the grasp tolerance of the MEMS clamps, which matched the yield in the layout design. The yield of alignment results was more than 95%.

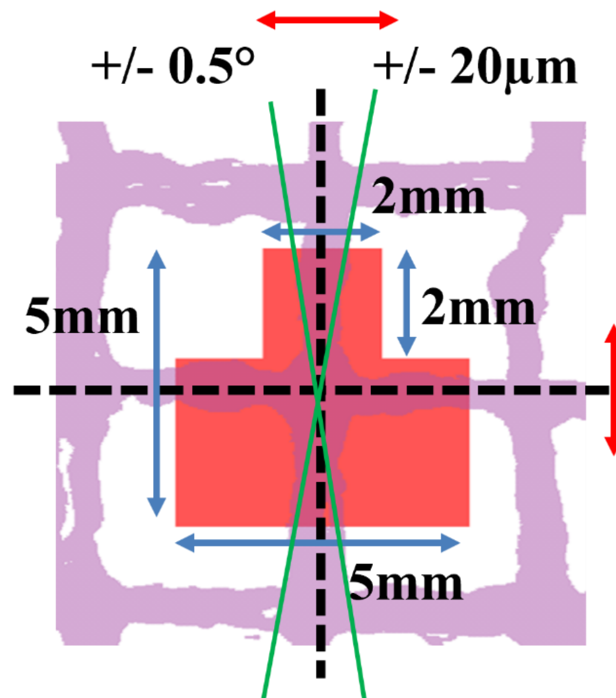

Figure 5. 47 The alignment errors in translational and rotational directions.

5.2.4.3 Auger Valve Printing

When the alignment process was done, the 4-DOF robotic arm moved to pick up the Auger valve on the tool change station, the MICROCHEM® SU-8-50 photoresist was set up on the Auger valve, and a gauge-14 nozzle was mounted on the bottom of the Auger valve. The nozzle position was calibrated with respect to the center of the Dino-lite camera. Based on the coordinate of the alignment mark intersection in the image of the camera, the center coordinate of the fabric can be calculated with respect to the center of the camera. The nozzle can be homogeneously transformed to the center of the fabric (shown in Fig. 5.48) to start the SU-8 photoresist printing referred to the G-code generated by Inkscape® software. There was a 55mm x 55mm square pattern of SU-8 photoresist was printed along the outline of the fabric. Then the Auger valve was removed from the top of the frame, the UV light was turned on for at least 10 minutes to cure the SU-8 photoresist.

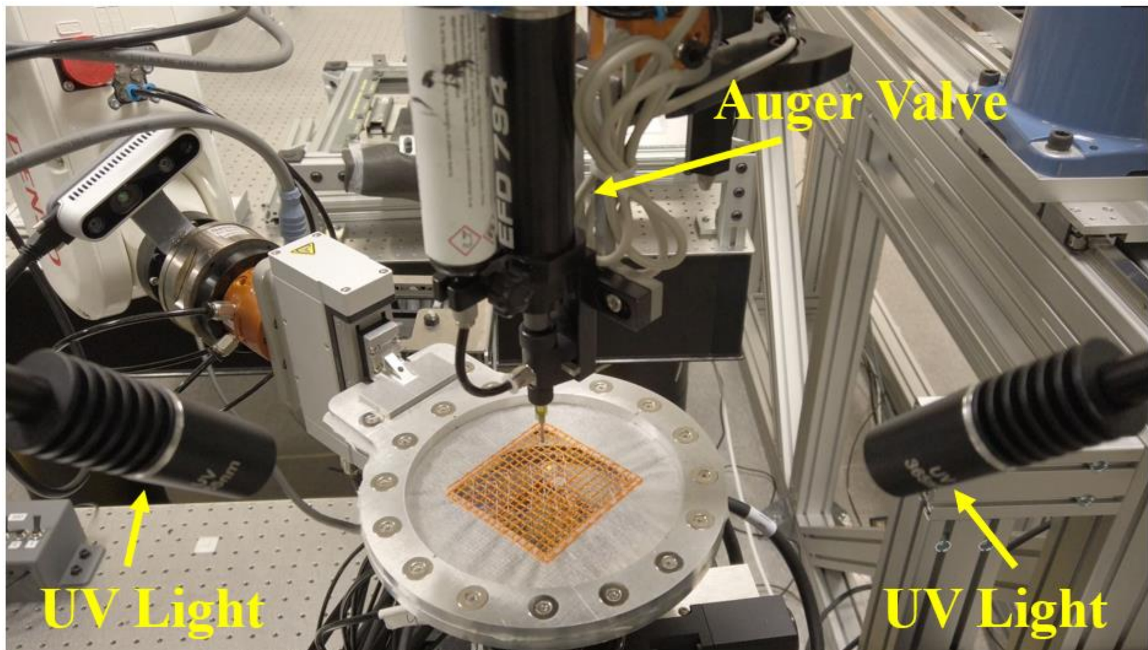

Figure 5. 48 The Auger valve dispenses the SU-8 photoresist on the fabric.

5.2.4.4 Releasing Results and Measurement

After the alignment process of MEMS microgrippers with intersections on the fiber textile via multi-robot collaboration in the NeXus system, the Silicon wafer was stuck on the bottom of the fiber textile with SU-8 photoresist. The metal frame needs to depart and remove from the textile, then the whole textile with a Silicon wafer was brought to the cleanroom for MEMS microgripper releasing process with XeF_2 gas etching. The releasing results of MEMS grippers are shown in Figure 5.49. Due to the polymer layer generation during the releasing process, the MEMS microgrippers were not released successfully even after several times and more cycles of releasing. However, fortunately, some microgrippers were released and grasped the intersections and conductive wires. By measuring the resistance between one microgripper pad to the end of the conductive wire, the measured result is around 850Ω, which conducted the potential of electrical textiles fabrication for wearable sensors.

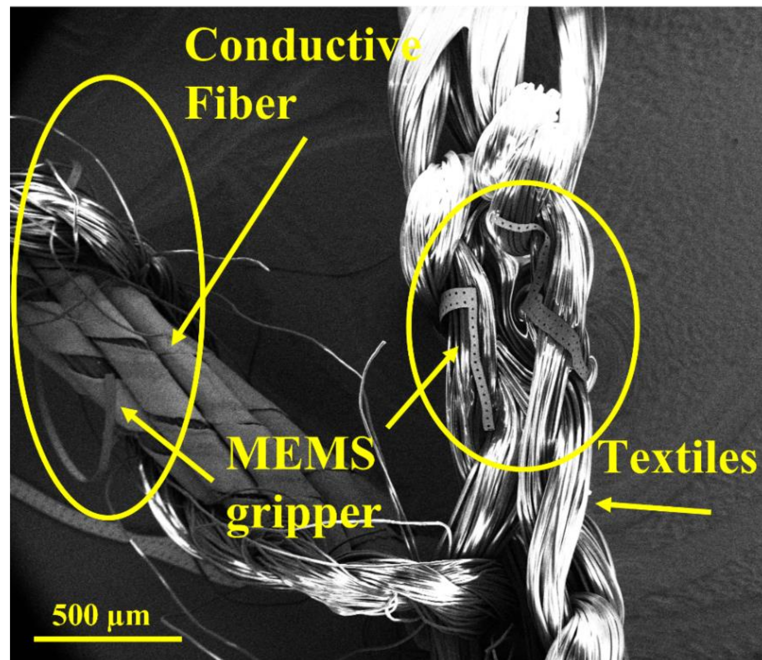

Figure 5. 49 Releasing results of MEMS microgrippers. (Figure acknowledgment: Chuang Qu)

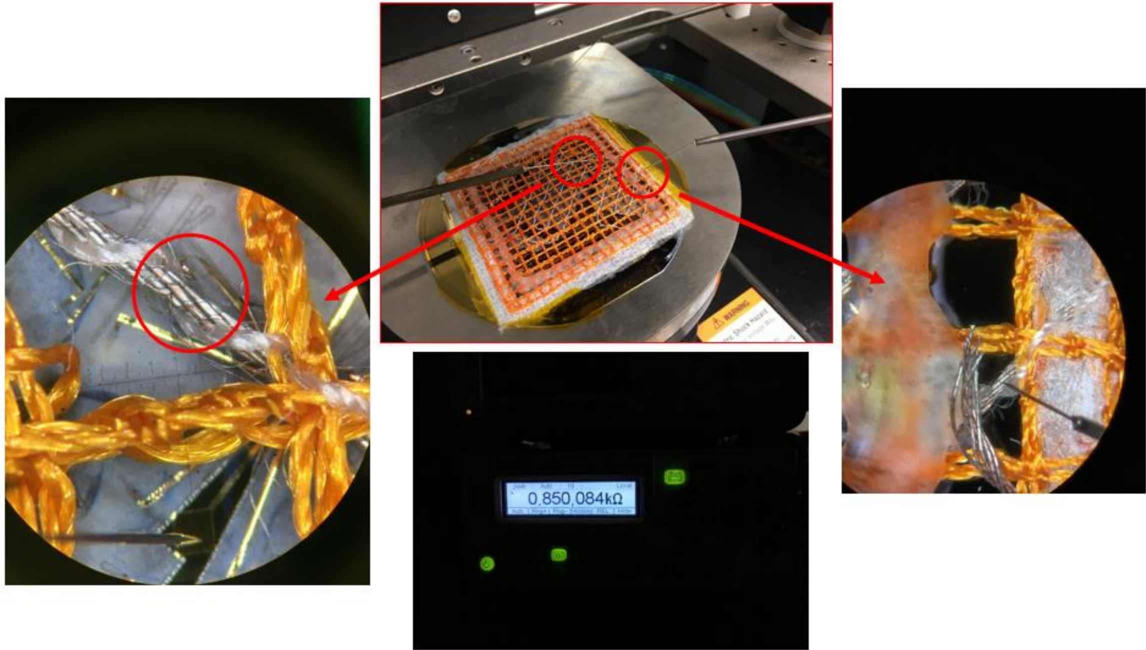

Figure 5. 50 Measurement of conductive fibers from a microgripper pad.

CHAPTER VI CONCLUSIONS AND FUTURE WORK

6.1 Conclusions

This thesis primarily introduces the use of the Lean Robotic Micromanufacturing (LRM) design methodology to configure the NeXus: a custom multi-scale additive manufacturing platform integrated with 3D printing and robotic assembly. The Lean Robotic Micromanufacturing design principles have been adopted for the NeXus design, simulation, implementation, integration, evaluation, calibration, optimization, synchronization, and control. After implementation and characterization, the NeXus was used to as fabricate several demonstrators, including tactile robotic skin, and electronic textiles.

The CAD design of the NeXus platform was created in Solidworks software which the simulation of some demonstrators was realized by Solidworks® Animation and the simulated NeXus system was controlled using a Digital Twin created LabVIEW® environment. The use of LabVIEW speeds up the deployment and programming of NeXus operations in the real environment. When the prediction of uncertainties produced by simulation matches the tolerance and budget of the design requirement in the LRM inner loop, we moved forward to finalizing specifications and purchasing the required hardware and instruments of the NeXus system. Hardware and instruments, such as optical tables, industrial robotics arms, high precision stages, pieces of the beam of the frame, and so on, are needed to be well organized and optimally distributed according to the system simulation results obtained through the digital twins.

A custom Aluminum frame was designed and installed to support the X-Y gantry with a ceiling-mounted 6-DOF industrial robotic arm. Given that frame's mechanical stiffness and its stability affect the robot motion performance and high-precision assembly applications, a careful static and dynamic analysis of the frame was critical.

Starting with the initial design and considering the first 3 eigenfrequencies and total deformation as design criteria, a progressive approach to improving the initial frame design was proposed. Using the FEA technique and COMSOL® simulation software, we investigated and simulated 4 various modular versions of frame design aiming to increase eigenfrequency and reduce total deformation in the frame structure.

By analyzing 5 different frame design versions, our study shows a consistent reduction occurring in maximum deflection in the frame from 3.5 mm in the initial design to 0.8mm in the final version. Similarly, considerable mitigation appeared in vibrational response, nearly by a factor of 2, as eigenfrequency jumped to 19.9Hz in the final version. In all cases, each frequency mode falls well below the measured end-effector frequency, ensuring no cross resonance will occur between the robot base (frame) and the end-effector. The nature of the frame structure also allows for a further increase in the structural stiffness to meet special requirements and applications, if necessary, in the future.

Evaluation of the robotic arm performance was realized with an Edmund microscope camera, two Keyence® displacement sensors, and a Mitutoyo Digimatic® indicator in three methods. The pose accuracy and repeatability of the robotic arm, X-Y gantry, and the combination of both were measured and calculated, respectively. Precision metrics results are consistent with expectations based on the manufacturer design metrics of the robotic arm and X-Y gantry structural features.

Tactile sensor fabrication and E-textiles fabrication are presented as demonstrators of the NeXus in the thesis. For tactile sensor fabrication, before completion of it in the NeXus, a new fabrication process to create PEDOT: PSS organic piezoresistive robotic skins was realized in the cleanroom. Improvements to the sensor material formulation with DMSO and PVP were introduced, while a protective layer of Parylene and Titanium was proposed. The protective layer is used during dry etching to protect the tactile areas. Furthermore, a lamination process was introduced to create double-sided sensors for temperature compensation and increased load sensitivity. Using an electronic data acquisition board, we collected amplified signals from sensor pairs, and we used a MATLAB® interface to visualize the response of each sensor pair strain gauge during load application. The experimental results indicate 100% process yield after fabrication (16 tactile sensors out of 16), and 82% yield after lamination (13 tactile sensors out of 16), results which are an improvement over prior work.

Instead of fabricating skin tactile sensors in the cleanroom using MEMS fabrication techniques, the NeXus system was developed and kinematically calibrated for strain gauge sensors fabrication on the flexible Kapton® substrate. Three calibration procedures were employed to align the printing tool with the samples by means of optical metrology. Inverse kinematic and visual servoing calibration techniques were applied to calibrate the OPTOMEC® Aerosol Inkjet printer nozzle with the starting point for printing the sensor on the substrate more precisely. During the visual servoing calibration process, the precision of calibration results of the fiducial mark is around +/-1.33μm in translation and +/-0.5 degrees in rotation. The calibration precision for the sensor printing is smaller than 200 microns, which is considerably less than the printing tolerance on the contact pads.

After the precision calibration of the manufacturing line for the tactile sensor in the NeXus, a novel circular combined-structure strain gauge tactile sensor is proposed in this paper. Based on two individual strain gauge structures: the radial structure and the arc structure, which have two opposite responses when the force is applied to its geometric center. It was established that our tactile sensor has stable performance at elevated temperatures from 20°C up to 100°C enabling efficient temperature drift compensation. Furthermore, several experiments were performed as a part of the study, such as single sub-indenter and multiple sub-indenters tests on the PDMS sensor's covers to determine the dependence of the sensor's responses on the geometry of the structure and its anisotropic character. Also, a 2x2 sensor array based on the tactile sensor was fabricated and tested with a 7x7 sub-indenters PDMS cover to characterize the spatial distance range for the responses of the sensor when the force was applied. In the future, based on this tactile sensor design, a larger sensor array, such as 3x3, or more, will be fabricated on the flexible substrate. Meanwhile, the corresponding PCB will be designed and produced to integrate the sensor array for robotics applications.

For the E-textiles fabrication demonstrator, except for fabricating the MEMS clamps and releasing the clamps to make them pop up to grasp the fabric structures, a multi-robot collaboration was employed to complete an electronic textile deterministic alignment process in the NeXus system. Compared with the 1st generation alignment process, in the 2nd generation alignment process in the NeXus, a metal frame was designed to clamp the fabric material to secure fibers deterministically and ensure dimensional stability, and a 4-inch wafer sample chuck was made to carry the wafer with the MEMS structures. Otherwise, two industrial robotic arms and a custom positioner as well as different tools,

like A Dino-lite® camera, an electrical gripper, and an Auger valve, were employed to accomplish the alignment process with high precision and repeatability. The yield of alignment results of the MEMS clamps and the corresponding fabric intersections are more than 95%.

6.2 Future work

Even though most hardware and software of the NeXus system have been completed, there still have many works that need to continue being investigated and developed. For example, each loop of the LRM design principle needs deeper research for more demonstrators or other possible tasks. Some functionalities, such as a custom 3D printer: stationary and movable, ultrasonic head for metal wire bonding or embedding on or into specific material, and microassembly station in the NeXus, should keep developing until completing corresponding demonstrators. Eventually, an additive manufacturing process of an entire product can be completed in the NeXus via an automated or semi-automated control in sequence.

For tactile sensor fabrication, some improvements need to be completed in the future, for instance, the probe station extended in the microassembly station can be integrated into the probe test function for measuring the resistances of the tactile sensors. Also, it needs to improve the calibration precision of the manufacturing line for the tactile sensor fabrication process, which can enhance the yield of products with high precision, reliability, and repeatability. The user interface of the NeXus needs to simplify and realize multi-functions to be compatible with different manufacturing tasks.

For E-textile fabrication, since new materials (nylon and SU-8 photoresist) have been tested and applied to the new recipe of the fabrication process, there is no more

polymer layer generation and improve the yield of products. Moreover, the UI for operating the multi-robot collaboration for the deterministic alignment process in the NeXus needs to simplify for the user to operate conveniently. Also, some electronic components, such as sensors, batteries, LEDs, etc., can be embedded into the fabrics to increase the functionalities of the E-textiles. some additional tools will be integrated into the NeXus, like a laser cutter, to cut off the mesh or a specific tool to remove or dissolve the UV curable adhesive to depart the fiber mesh and wafer after the MEMS clamps grasped the intersections of the textiles. The individual fiber mesh will be the end product for further applications.

REFERENCES

[1] J. Giannatsis and V. Dedoussis, "Additive fabrication technologies applied to medicine and health care: a review," *The International Journal of Advanced Manufacturing Technology,* vol. 40, no. 1-2, pp. 116-127, 2009.

[2] Y. Song, Y. Yan, R. Zhang, D. Xu, and F. Wang, "Manufacture of the die of an automobile deck part based on rapid prototyping and rapid tooling technology," *Journal of materials processing technology,* vol. 120, no. 1-3, pp. 237-242, 2002.

[3] C. L. Thomas, T. M. Gaffney, S. Kaza, and C. H. Lee, "Rapid prototyping of large scale aerospace structures," in *1996 IEEE Aerospace Applications Conference. Proceedings*, 1996, vol. 4: IEEE, pp. 219-230.

[4] J. Comb, W. Priedeman, and P. W. Turley, "FDM® Technology process improvements," in *1994 International Solid Freeform Fabrication Symposium*, 1994.

[5] P. F. Jacobs, "Fundamentals of stereolithography," in *1992 International Solid Freeform Fabrication Symposium*, 1992.

[6] J. Mazumder, A. Schifferer, and J. Choi, "Direct materials deposition: designed macro and microstructure," *Material Research Innovations,* vol. 3, no. 3, pp. 118-131, 1999.

[7] M. Feygin and B. Hsieh, "Laminated object manufacturing (LOM): a simpler process," in *1991 International Solid Freeform Fabrication Symposium*, 1991.

[8] J. J. Beaman, J. W. Barlow, D. L. Bourell, R. H. Crawford, H. L. Marcus, and K. P. McAlea, "Solid freeform fabrication: a new direction in manufacturing," *Kluwer Academic Publishers, Norwell, MA,* vol. 2061, pp. 25-49, 1997.

[9] C. Groth, N. D. Kravitz, P. E. Jones, J. W. Graham, and W. R. Redmond, "Three-dimensional printing technology," *J Clin Orthod,* vol. 48, no. 8, pp. 475-85, 2014.

[10] P. Dennis, *Lean Production simplified: A plain-language guide to the world's most powerful production system*. Crc press, 2017.

[11] R. Murthy, A. N. Das, and H. E. Stephanou, "Micro-nano integration via hybrid control of multiscale manipulators," in *2010 IEEE Nanotechnology Materials and Devices Conference*, 2010: IEEE, pp. 61-64.

[12] R. Murthy, A. N. Das, D. Popa, and H. Stephanou, "M3: Multiscale, deterministic and reconfigurable macro-micro assembly system for packaging of mems," in *Proceedings 2007 IEEE International Conference on Robotics and Automation*, 2007: IEEE, pp. 668-673.

[13] D. Popa, R. Murthy, M. Mittal, J. Sin, and H. Stephanou, "M3-modular multi-scale assembly system for MEMS packaging," in *2006 IEEE/RSJ International Conference on Intelligent Robots and Systems*, 2006: IEEE, pp. 3712-3717.

[14] R. Murthy, A. Das, and D. Popa, "Multiscale robotics framework for MEMS assembly," in *2006 9th International Conference on Control, Automation, Robotics and Vision*, 2006: IEEE, pp. 1-6.

[15] D. O. Popa and H. E. Stephanou, "Micro and mesoscale robotic assembly," *Journal of manufacturing processes,* vol. 6, no. 1, pp. 52-71, 2004.

[16] A. N. Das, D. O. Popa, and H. E. Stephanou, "Automated microassembly using precision based hybrid control," in *2010 IEEE International Conference on Robotics and Automation*, 2010: IEEE, pp. 4106-4112.

[17] B. Komati, M. R. Pac, I. Ranatunga, C. Clévy, D. O. Popa, and P. Lutz, "Explicit force control vs impedance control for micromanipulation," in *International Design Engineering Technical Conferences and Computers and Information in Engineering Conference*, 2013, vol. 55843: American Society of Mechanical Engineers, p. V001T09A018.

[18] M. R. Pac, M. Rakotondrabe, S. Khadraoui, D. O. Popa, and P. Lutz, "Guaranteed manipulator precision via interval analysis of inverse kinematics," in *International Design Engineering Technical Conferences and Computers and Information in Engineering Conference*, 2013, vol. 55843: American Society of Mechanical Engineers, p. V001T09A017.

[19] M. R. Pac and D. O. Popa, "Interval analysis of kinematic errors in serial manipulators using product of exponentials formula," *IEEE Transactions on Automation Science and Engineering,* vol. 10, no. 3, pp. 525-535, 2013.

[20] A. N. Das and D. O. Popa, "Precision-based robot path planning for microassembly," in *2010 IEEE International Conference on Automation Science and Engineering*, 2010: IEEE, pp. 527-532.

[21] D. Popa, B. H. Kang, J. Sin, and J. Zou, "Reconfigurable micro-assembly system for photonics applications," in *Proceedings 2002 IEEE International Conference on Robotics and Automation (Cat. No. 02CH37292)*, 2002, vol. 2: IEEE, pp. 1495-1500.

[22] R. Murthy and D. O. Popa, "Millimeter-scale microrobots for wafer-level factories," in *2010 IEEE International Conference on Robotics and Automation*, 2010: IEEE, pp. 488-493.

[23] R. Murthy and D. O. Popa, "A four degree of freedom microrobot with large work volume," in *2009 IEEE International Conference on Robotics and Automation*, 2009: IEEE, pp. 1028-1033.

[24] D. O. Popa, R. Murthy, and A. N. Das, "${\rm M}^{3} $-Deterministic, Multiscale, Multirobot Platform for Microsystems Packaging: Design and Quasi-Static Precision Evaluation," *IEEE Transactions on Automation Science and Engineering,* vol. 6, no. 2, pp. 345-361, 2009.

[25] A. N. Das, P. Zhang, W. H. Lee, D. Popa, and H. Stephanou, "μ 3: Multiscale, deterministic micro-nano assembly system for construction of on-wafer microrobots," in *Proceedings 2007 IEEE International Conference on Robotics and Automation*, 2007: IEEE, pp. 461-466.

[26] A. N. Das, J. Sin, D. O. Popa, and H. E. Stephanou, "Design and manufacturing of a fourier transform microspectrometer," in *2008 8th IEEE Conference on Nanotechnology*, 2008: IEEE, pp. 837-840.

[27] A. A. Fasoro, M. Mittal, D. O. Popa, D. A. Agonafer, and H. E. Stephanou, "Design for Reliability Applied to Packaging of a MOEMS Switch," 2008.

[28] C. Bartolozzi, L. Natale, F. Nori, and G. Metta, "Robots with a sense of touch," *Nature materials,* vol. 15, no. 9, pp. 921-925, 2016.

[29] M. Johnsson and C. Balkenius, "Sense of touch in robots with self-organizing maps," *IEEE Transactions on Robotics,* vol. 27, no. 3, pp. 498-507, 2011.

[30] B. Ward-Cherrier, L. Cramphorn, and N. F. Lepora, "Tactile manipulation with a TacThumb integrated on the open-hand M2 gripper," *IEEE Robotics and Automation Letters,* vol. 1, no. 1, pp. 169-175, 2016.

[31] T. Mukai, M. Onishi, T. Odashima, S. Hirano, and Z. Luo, "Development of the tactile sensor system of a human-interactive robot "RI-MAN"," *IEEE Transactions on robotics,* vol. 24, no. 2, pp. 505-512, 2008.

[32] T. Hoshi and H. Shinoda, "Robot skin based on touch-area-sensitive tactile element," in *Proceedings 2006 IEEE International Conference on Robotics and Automation, 2006. ICRA 2006.*, 2006: IEEE, pp. 3463-3468.

[33] M. Inaba, Y. Hoshino, K. Nagasaka, T. Ninomiya, S. Kagami, and H. Inoue, "A full-body tactile sensor suit using electrically conductive fabric and strings," in *Proceedings of IEEE/RSJ International Conference on Intelligent Robots and Systems. IROS'96*, 1996, vol. 2: IEEE, pp. 450-457.

[34] L. Misery, K. Loser, and S. Ständer, "Sensitive skin," *Journal of the European Academy of Dermatology and Venereology,* vol. 30, pp. 2-8, 2016.

[35] C. Wang *et al.*, "User-interactive electronic skin for instantaneous pressure visualization," *Nature materials,* vol. 12, no. 10, pp. 899-904, 2013.

[36] B. D. Argall and A. G. Billard, "A survey of tactile human–robot interactions," *Robotics and autonomous systems,* vol. 58, no. 10, pp. 1159-1176, 2010.

[37] R. S. Dahiya, G. Metta, M. Valle, and G. Sandini, "Tactile sensing—from humans to humanoids," *IEEE transactions on robotics,* vol. 26, no. 1, pp. 1-20, 2009.

[38] M. N. Saadatzi, J. R. Baptist, Z. Yang, and D. O. Popa, "Modeling and fabrication of scalable tactile sensor arrays for flexible robot skins," *IEEE Sensors Journal,* vol. 19, no. 17, pp. 7632-7643, 2019.

[39] J. Baptist, R. Zhang, D. Wei, M. Saadatzi, and D. Popa, "Fabrication of strain gauge sensor arrays for tactile skins," in *Proc. SPIE*, 2017, vol. 10216, p. 1021619.

[40] S. K. Das, J. R. Baptist, R. Sahasrabuddhe, W. H. Lee, and D. O. Popa, "Package analysis of 3D-printed piezoresistive strain gauge sensors," in *Sensors for Next-Generation Robotics III*, 2016, vol. 9859: International Society for Optics and Photonics, p. 985905.

[41] M. N. Saadatzi, J. R. Baptist, I. B. Wijayasinghe, and D. O. Popa, "Characterization of large-area pressure sensitive robot skin," in *Smart Biomedical and Physiological Sensor Technology XIV*, 2017, vol. 10216: International Society for Optics and Photonics, p. 102160G.

[42] C. Nothnagle, J. R. Baptist, J. Sanford, W. H. Lee, D. O. Popa, and M. B. Wijesundara, "EHD printing of PEDOT: PSS inks for fabricating pressure and strain sensor arrays on flexible substrates," in *Next-Generation Robotics II; and Machine Intelligence and Bio-inspired Computation: Theory and Applications IX*, 2015, vol. 9494: International Society for Optics and Photonics, p. 949403.

[43] D. Wei, R. Zhang, M. N. Saadatzi, O. O. Olowo, and D. O. Popa, "Organic Piezoresistive Pressure Sensitive Robotic Skin for Physical Human-Robot Interaction," in *International Design Engineering Technical Conferences and Computers and Information in Engineering Conference*, 2020, vol. 83907: American Society of Mechanical Engineers, p. V001T01A013.

[44] H. Zhang, X. Tao, T. Yu, and S. Wang, "Conductive knitted fabric as large-strain gauge under high temperature," *Sensors and Actuators A: Physical,* vol. 126, no. 1, pp. 129-140, 2006.

[45] A. Dhawan, A. M. Seyam, T. K. Ghosh, and J. F. Muth, "Woven fabric-based electrical circuits: Part I: Evaluating interconnect methods," *Textile Research Journal,* vol. 74, no. 10, pp. 913-919, 2004.

[46] E. R. Post, M. Orth, P. R. Russo, and N. Gershenfeld, "E-broidery: Design and fabrication of textile-based computing," *IBM Systems journal,* vol. 39, no. 3.4, pp. 840-860, 2000.

[47] A. A. Tracton, *Coatings technology handbook*. CRC press, 2005.

[48] Y. Hasegawa, M. Shikida, D. Ogura, and K. Sato, "Novel type of fabric tactile sensor made from artificial hollow fiber," in *2007 IEEE 20th International Conference on Micro Electro Mechanical Systems (MEMS)*, 2007: IEEE, pp. 603-606.

[49] D. Zabetakis, M. Dinderman, and P. Schoen, "Metal-Coated Cellulose Fibers for Use in Composites Applicable to Microwave Technology," *Advanced Materials,* vol. 17, no. 6, pp. 734-738, 2005.

[50] Q. Wei, Y. Xu, and Y. Wang, "Textile surface functionalization by physical vapor deposition (PVD)," in *Surface modification of textiles*: Elsevier, 2009, pp. 58-90.

[51] A. Kaynak, L. Wang, C. Hurren, and X. Wang, "Characterization of conductive polypyrrole coated wool yarns," *Fibers and Polymers,* vol. 3, no. 1, pp. 24-30, 2002.

[52] M. Sauer and S. Meilchen, "Screen Printing in Sol-Gel Technologies for Glass Producers and User," ed: Springer Science & Business Media, 2004.

[53] L. M. Castano and A. B. Flatau, "Smart fabric sensors and e-textile technologies: a review," *Smart Materials and structures,* vol. 23, no. 5, p. 053001, 2014.

[54] Y. Dong, Y. Zou, J. Song, Z. Zhu, J. Li, and H. Zeng, "Self-powered fiber-shaped wearable omnidirectional photodetectors," *Nano Energy,* vol. 30, pp. 173-179, 2016.

[55] T. L. Buckner and R. Kramer-Bottiglio, "Functional fibers for robotic fabrics," *Multifunctional Materials,* vol. 1, no. 1, p. 012001, 2018.

[56] K. N. Kim *et al.*, "Highly stretchable 2D fabrics for wearable triboelectric nanogenerator under harsh environments," *ACS nano,* vol. 9, no. 6, pp. 6394-6400, 2015.

[57] T. Agcayazi, K. Chatterjee, A. Bozkurt, and T. K. Ghosh, "Flexible interconnects for electronic textiles," *Advanced Materials Technologies,* vol. 3, no. 10, p. 1700277, 2018.

[58] J. Ou, D. Oran, D. D. Haddad, J. Paradiso, and H. Ishii, "SensorKnit: architecting textile sensors with machine knitting," *3D Printing and Additive Manufacturing,* vol. 6, no. 1, pp. 1-11, 2019.

[59] K. Niayesh, L. Niemeyer, and J. Fabian, "Matrix combination of elementary switches: general considerations and application to MEMS relays," *Electrical Engineering,* vol. 90, no. 1, pp. 19-31, 2007.

[60] M.-N. Nashed, D. A. Hardy, T. Hughes-Riley, and T. Dias, "A novel method for embedding semiconductor dies within textile yarn to create electronic textiles," *Fibers,* vol. 7, no. 2, p. 12, 2019.

[61] R. E. Owyeung, T. Terse-Thakoor, H. Rezaei Nejad, M. J. Panzer, and S. R. Sonkusale, "Highly flexible transistor threads for all-thread based integrated circuits and multiplexed diagnostics," *ACS applied materials & interfaces,* vol. 11, no. 34, pp. 31096-31104, 2019.

[62] M. N. Saadatzi, Z. Yang, J. R. Baptist, R. R. Sahasrabuddhe, I. B. Wijayasinghe, and D. O. Popa, "Parametric investigation of scalable tactile sensors," in *Smart Biomedical and Physiological Sensor Technology XIV*, 2017, vol. 10216: SPIE, pp. 51-60.

[63] D. Ratnayake, A. Curry, and K. Walsh, "Demonstrating a new ink material for aerosol printing conductive traces and custom strain gauges on flexible surfaces," in *2021 IEEE International Conference on Flexible and Printable Sensors and Systems (FLEPS)*, 2021: IEEE, pp. 1-4.

[64] D. Ratnayake, A. T. Curry, C. Qu, J. Usher, and K. Walsh, "Characterizing the Conductivity of Aerosol Jet Printed Silver Features on Glass," in *International Manufacturing Science and Engineering Conference*, 2021, vol. 85079: American Society of Mechanical Engineers, p. V002T08A007.

[65] D. Wei *et al.*, "Precision Evaluation of NeXus, a Custom Multi-Robot System for Microsystem Integration," in *International Manufacturing Science and Engineering Conference*, 2021, vol. 85079: American Society of Mechanical Engineers, p. V002T07A008.

[66] M. H. Saadatzi and D. O. Popa, "Kinematic Analysis of a 5-DOF Positioner for Precision Additive Manufacturing," in *International Design Engineering Technical Conferences and Computers and Information in Engineering Conference*, 2020, vol. 83990: American Society of Mechanical Engineers, p. V010T10A096.

[67] D. Wei *et al.*, "Automated Fabrication of Tactile Sensors Using a Custom Additive Manufacturing Platform," in *2022 International Conference on Manipulation, Automation and Robotics at Small Scales (MARSS)*, 2022: IEEE, pp. 1-6.

[68] S. Challa, M. S. Islam, D. Wei, J. Beharic, D. O. Popa, and C. Harnett, "Functional Fiber Junctions for Circuit Routing in E-Textiles: Deterministic Alignment of MEMS Layout With Fabric Structure," in *International Manufacturing Science and Engineering Conference*, 2021, vol. 85079: American Society of Mechanical Engineers, p. V002T08A009.

[69] S. Timoshenko, "Analysis of bi-metal thermostats," *Josa,* vol. 11, no. 3, pp. 233-255, 1925.

[70] D. Wei, M. B. Hall, A. Sherehiy, and D. O. Popa, "Design and Evaluation of Human–Machine Interface for NEXUS: A Custom Microassembly System," *Journal of Micro-and Nano-Manufacturing,* vol. 8, no. 4, p. 041011, 2020.

APPENDICES

Publications**:**

During the period of my Ph.D. program, my research regarding the NeXus project contributed to four ASME conference papers, two IEEE MARSS conference papers, and one ASME Journal of Micro-Nano Manufacturing paper regarding investigation and development of the NeXus subsystems and demonstrators have been published as the first author.

1. D. Wei et al., "Precision Evaluation of NeXus, a Custom Multi-Robot System for Microsystem Integration," in ASME 2021 16th International Manufacturing Science and Engineering Conference, 2021, vol. Volume 2: Manufacturing Processes; Manufacturing Systems; Nano/Micro/Meso Manufacturing; Quality and Reliability, V002T07A008, doi: 10.1115/msec2021-63687. [Online]. Available: https://doi.org/10.1115/MSEC2021-63687.
2. D. Wei, M. B. Hall, A. Sherehiy, S. Kumar Das, and D. O. Popa, "Design and Evaluation of Human-Machine Interface for NEXUS: A Custom Microassembly System," in ASME 2020 15th International Manufacturing Science and Engineering Conference, 2020, vol. Volume 2: Manufacturing Processes; Manufacturing Systems; Nano/Micro/Meso Manufacturing; Quality and Reliability, V002T08A018, doi: 10.1115/msec2020-8477. [Online]. Available: https://doi.org/10.1115/MSEC2020-8477.
3. D. Wei, R. Zhang, M. N. Saadatzi, O. O. Olowo, and D. O. Popa, "Organic Piezoresistive Pressure Sensitive Robotic Skin for Physical Human-Robot Interaction," in International Design Engineering Technical Conferences and Computers and Information in Engineering Conference, 2020, vol. 83907: American Society of Mechanical Engineers, p. V001T01A013.
4. D. Wei, C. M. Trombley, A. Sherehiy, and D. O. Popa, "Precise and Effective Robotic Tool Change Strategy Using Visual Servoing With RGB-D Camera," in *International Design Engineering Technical Conferences and Computers and Information in Engineering Conference*, 2021, vol. 85451: American Society of Mechanical Engineers, p. V08BT08A028.
5. D. Wei et al., "Automated Fabrication of Tactile Sensors Using a Custom Additive Manufacturing Platform," in 2022 International Conference on Manipulation, Automation and Robotics at Small Scales (MARSS), 2022: IEEE, pp. 1-6.

6. D. Wei, S. Challa, M. S. Islam, J. Beharic, C. K. Harnett, and D. O. Popa, "Multi-Robot Collaboration for Electronic Textile Fabrication," in 2022 International Conference on Manipulation, Automation and Robotics at Small Scales (MARSS), 2022: IEEE, pp. 1-6.
7. D. Wei, M. B. Hall, A. Sherehiy, and D. O. Popa, "Design and Evaluation of Human–Machine Interface for NEXUS: A Custom Microassembly System," Journal of Micro-and Nano-Manufacturing, vol. 8, no. 4, p. 041011, 2020.

Besides the conference and Journal papers listed above, I am also involved in two more Journal of Micro-Bio Robotics papers and several ASME and IEEE papers as the co-author collaborating with others NGS group members.

1. Zhang, R., Sherehiy, A., Wei, D., & Popa, D. O. (2019). Design and characterization of solid articulated four axes microrobot for microfactory applications. *Journal of Micro-Bio Robotics*, *15*(2), 119-131.
2. Zhang, R., Klotz, J. F., Wei, D., Yang, Z., Sherehiy, A., Saadatzi, M. N., & Popa, D. O. (2020). SolarPede: a stick-and-slip, light-powered, Mobile micro-crawler. *Journal of Micro-Bio Robotics*, *16*(1), 1-12.
3. Olowo, O. O., Wei, D., Ratnayake, D., Goulet, B., Curry, A., Sherehiy, A., ... & Popa, D. O. (2022, July). PEDOT: PSS Polymer Aerosol Jet-printing for Robotic Skin Sensors. In 2022 IEEE International Conference on Flexible and Printable Sensors and Systems (FLEPS) (pp. 1-4). IEEE.
4. Olowo, O. O., Zhang, R., Wei, D., Ratnayake, D., Jackson, D., & Popa, D. O. (2022, July). Aerosol Jet Printed Tactile Sensor on Flexible Substrate. In 2022 IEEE International Conference on Flexible and Printable Sensors and Systems (FLEPS) (pp. 1-4). IEEE.
5. Morice, S., Sherehiy, A., Wei, D., and Popa, D. O., " Characterization of the Direct Write Inkjet Printing Process for Automated Fabrication of PEDOT: PSS Thin Films," in Proceeding. ASME 2022 17th International Manufacturing Science and Engineering Conference.
6. Ferris, C., Ratnayake, D., Curry, A., Wei, D., Gerber, E., Druffel, T., and Walsh, K., " Characterizing the Conductivity of Aerosol Jet Printed Silver Traces on Glass Using Intense Pulsed Light (IPL)," in Proceeding. ASME 2022 17th International Manufacturing Science and Engineering Conference.
7. Olowo, Ola., Zhang, R., Sherehiy, A., Goulet, B., Curry, A., Wei, D., Yang, Z., Alqatamin, M., and Popa, D. O., " Inkjet Printing of PEDOT: PSS Inks for Robotic Skin Sensors," in Proceeding. ASME 2022 17th International Manufacturing Science and Engineering Conference.
8. Warn, C., Sherehiy, A., Alqatamin, M., Ritz, B., Zhang, R., Chowdhury, S.,

Wei, D., and Popa, D. O., " Machine Vision Tracking and Automation of a Microrobot (sAFAM)," in Proceeding. ASME 2022 17th International Manufacturing Science and Engineering Conference.

9. Nimon, A., Sherehiy, A., Alqatamin, M., Wei, D., and Popa, D. O., " Precision Evaluation of Large Payload SCARA Robot for PCB Assembly," in Proceeding. ASME 2022 17th International Manufacturing Science and Engineering Conference.
10. Alqatamin, M., Ritz, B., Sherehiy, A., Jackson, D., Zhang, R., Chowdhury, S.S., Wei, D. and Popa, D.O., 2021, August. Teleoperation Interface for sAFAM, a Solid Articulated Four Axes Microrobot. In International Design Engineering Technical Conferences and Computers and Information in Engineering Conference (Vol. 85482, p. V011T11A017). American Society of Mechanical Engineers.
11. Challa, S., Islam, M.S., Wei, D., Beharic, J., Popa, D.O. and Harnett, C.K., 2021, June. Functional Fiber Junctions for Circuit Routing in E-Textiles: Deterministic Alignment of MEMS Layout with Fabric Structure. In International Manufacturing Science and Engineering Conference (Vol. 85079, p. V002T08A009). American Society of Mechanical Engineers.
12. Sherehiy, A., Montenegro, A., Wei, D. and Popa, D.O., 2021, June. Adhesive Deposition Process Characterization for Microstructure Assembly. In International Manufacturing Science and Engineering Conference (Vol. 85079, p. V002T08A012). American Society of Mechanical Engineers.
13. Yang, Z., Sherehiy, A., Chowdhury, S.S., Wei, D., Zhang, R. and Popa, D.O., 2020, August. Design, Fabrication and Experimental Validation of a Steerable, Laser-Driven Microrobot in Dry Environments. In 2020 IEEE 16th International Conference on Automation Science and Engineering (CASE) (pp. 882-887). IEEE.
14. Chowdhury, S.S., Yang, Z., Sherehiy, A., Zhang, R., Wei, D. and Popa, D.O., 2020, July. Parametric Investigation of Laser-Driven Microrobot Maneuverability on Dry Substrates. In 2020 International Conference on Manipulation, Automation and Robotics at Small Scales (MARSS) (pp. 1-6). IEEE.
15. Yang, Z., Saadatzi, M.N., Zhang, R., Sherehiy, A., Wei, D., Harnett, C.K. and Popa, D.O., 2019, August. Multiphysics dynamic model validation methodology for laser-driven microrobots. In 2019 IEEE 15th International Conference on Automation Science and Engineering (CASE) (pp. 1555-1561). IEEE.
16. Klotz, J.F., Wei, D., Yang, Z., Zhang, R., Sherehiy, A., Saadatzi, M.N. and Popa, D.O., 2019, July. Concept validation for a novel stick-and-slip, light-powered, Mobile micro-crawler. In 2019 International Conference on Manipulation, Automation and Robotics at Small Scales (MARSS) (pp. 1-7).

IEEE.

17. Zhang, R., Sherehiy, A., Wei, D., Yang, Z., Saadatzi, M.N. and Popa, D.O., 2019, July. Tracking Experiments with ChevBot: A Laser-Actuated Stick-Slip Microrobot. In 2019 International Conference on Manipulation, Automation and Robotics at Small Scales (MARSS) (pp. 1-6). IEEE.
18. Zhang, R., Sherehiy, A., Yang, Z., Wei, D., Harnett, C.K. and Popa, D.O., 2019, May. ChevBot–An Untethered Microrobot Powered by Laser for Microfactory Applications. In 2019 International Conference on Robotics and Automation (ICRA) (pp. 231-236). IEEE.
19. Zhang, R., Wei, D. and Popa, D.O., 2018, July. Design, analysis and fabrication of sAFAM, a 4 DoF assembled microrobot. In 2018 International Conference on Manipulation, Automation and Robotics at Small Scales (MARSS) (pp. 1-6). IEEE.
20. Baptist, J.R., Zhang, R., Wei, D., Saadatzi, M.N. and Popa, D.O., 2017, May. Fabrication of strain gauge based sensors for tactile skins. In Smart Biomedical and Physiological Sensor Technology XIV (Vol. 10216, p. 102160F). International Society for Optics and Photonics.
21. Zhang, R., Yang, Z., Wei, D. and Popa, D.O., 2017, May. Design and fabrication of an articulated four axes microrobot arm. In Smart Biomedical and Physiological Sensor Technology XIV (Vol. 10216, p. 102160C). International Society for Optics and Photonics.

CURRICULUM VITA

Danming Wei, Ph.D.
Next Generation System Group (NGS)
Louisville Automation and Robotic Research Institute (LARRI)
Electrical and Computer Engineering Department
Louisville, Kentucky, 40209
Email: danming.wei@louisville.edu
Phone: (+86)13185089266

Education:

University of Louisville (Louisville, Kentucky)
Ph.D. Electrical Engineering Aug. 2018 to Nov. 2022
Dissertation: Design, evaluation, and control of NeXus: a multiscale additive manufacturing platform with integrated 3D printing and robotic assembly

University of Louisville (Louisville, Kentucky)
M.E. Electrical Engineering Aug. 2016 to May. 2018
Thesis: Challenges in flexible microsystem manufacturing: fabrication, robotic assembly, control, and packaging

Western Kentucky University (Bowling Green, Kentucky)
M.E. Chemistry Jan. 2014 to May. 2017
Thesis: Low-Cost Quartz Crystal Microbalance System Platform Designed for Chemical Nanoparticle Analysis

Dalian Jiaotong University (Dalian, China)
B.E. Automation Sept. 2007 to Jul. 2011

Technical Experience:

University of Louisville
Louisville Automation and Robotics Research Institute (LARRI)
Next Generation System (NGS) Groups

- **Graduate Research Assistant** Aug. 2018 to Dec. 2022
  - **MEMS/NEMS:** Fabrication of Microrobots, Skin Tactile Sensor, and Microgrippers for Electronic Textiles.
  - **Microsystem:** Microassembly Station and Human-Machine Interface (Semi-automation).

- **Robotic system:** 6DOF and 4DOF Industrial Robots (DENSO), Multiple Tools (Gripper, Dispenser, 3D printer, Aerosol Inkjet printer, etc.), Robotic Tool Changer, Robotic Force/Torque Sensor, and Vision Assistant.
- **Additive Manufacturing System:** Multi-scale additive manufacturing platform integrated with 3D printing and robotic assembly techniques. (Simulation, Integration, Synchronization, Optimization, and Automation)

University of Louisville

- **Graduate Teaching Assistant** Jan. 2017 to May. 2020
  1. **Foundation of Microfabrication and MEMS Laboratory (in Cleanroom)**
     Aug. 2018 to Dec. 2018
     Aug. 2017 to Dec. 2017
     Aug. 2019 to Dec. 2019
  2. **LabVIEW for Electrical Engineers** Jan. 2020 to May. 2020
  3. **Logic Design Laboratory** Jan. 2017 to May. 2017
     Jan. 2018 to May. 2018
  4. **Network Analysis Laboratory** Jan. 2018 to May. 2018

Western Kentucky University
Institute for Combustion Science and Environment Technology (ICSET)

- **Graduate Research Assistant** Jan. 2015 to May.2016
  - Chemical Analytical System: Design, Simulation, Test, and Control.

Western Kentucky University

- **Graduate Teaching Assistant** Aug. 2014 to Dec.2014

Honors, Patents, and Awards:

- **Mobile Microrobotics Challenge (MMC) 2017:** Finalist of IEEE Robotics and Automation Society, Mobile Microrobotics Challenge (MMC) 2017
- **Patent:** US, 63/213,002
- **Grosscurth Scholarship** Aug. 2018 to July.2020
- **Dissertation Completion Award** Aug. 2022 to Dec. 2022

Professional Skills:

- Proficient in MEMS/NEMS fabrication techniques in Class-100 Cleanroom – 5 years
  - **MEMS/NMES/IC Layout design and simulation:** Tanner L-Edit, ANSYS, COMSOL, and CoventorWare.
  - **Semiconductor fabrication processes:** Photolithography (Photoresist Spinner, Suss Mask Aligner MA6/MA8, Photoresist Development, YES Image Reversal Vacuum Oven, Lift-off process), Metal Sputtering System (Lesker PVD-75, Technics 4604), Dry Etch (March RIE,

XACTIX XeF_2 Etching System, Trion Metal Etcher, DRIE), and Wet Etch (RCA wafer clean, HF/BOE Etching).
    - **Metrology:** Veeco Dektak 8M Profilometer, Veeco FPP-5000 4-Point Probe, Zygo Optical Interferometer, and Veeco NT1100 Optical Profilometer.
    - **Scanning Electron Microscopy:** TESCAN Vega 3 SEM, Apreo C LoVac FESEM, and FEI Nova 600 SEM.
- Multi-scale robots (industrial robots and microrobots) control system – 5 years
- Additive manufacturing control system – 4 years
- Automatic control system – 8 years
- NI LabVIEW, MATLAB, Solidworks, Fusion360, Python, C++, ROS expertise – 6 years
- Proficient in Microsoft Office Software (Word, Excel, PowerPoint, etc.) – 8 years

Funded Projects Involved:

National Science Foundation (NSF)

1. **NSF IIP#1643989:** https://www.nsf.gov/awardsearch/showAward?AWD_ID=1643989

Project: Adaptive Robotic Nursing Assistants for Physical Tasks in Hospital Environments
Funds: $880,776

2. **NSF IIS#1208623:** https://www.nsf.gov/awardsearch/showAward?AWD_ID=1208623

Project: Multi-modal sensor skin and garments for healthcare and home robots
Funds: $1,349,766

3. **NSF IIS#1633119:** https://www.nsf.gov/awardsearch/showAward?AWD_ID=1633119

Project: Design Tools for Nanofactories with Robust Millimetric Assemblers
Funds: $149,948

4. **NSF CMMI#1734383:** https://www.nsf.gov/awardsearch/showAward?AWD_ID=1734383

Project: Light-Powered Microrobots for Future Microfactories
Funds: $778,259

5. **NSF MRI#1828355:** https://www.nsf.gov/awardsearch/showAward?AWD_ID=1828355

Project: Development of a Multiscale Additive Manufacturing Instrument with Integrated 3D Printing and Robotic Assembly
Funds: $1,530,219

6. **NSF EPSCoR#1849213:** https://www.nsf.gov/awardsearch/showAward?AWD_ID=1849213

Project: Kentucky Advanced Manufacturing Partnership for Enhanced Robotics and Structures
Funds: $12,133,649

7. **NSF Award ECCS#2025075:** https://www.nsf.gov/awardsearch/showAward?AWD_ID=2025075

Project: KY Multiscale
Funds: $1,400,000